

**CZECH TECHNICAL
UNIVERSITY
IN PRAGUE**

**FACULTY
OF CIVIL
ENGINEERING**



**DOCTORAL
THESIS**

2018

**JAN
STRÁNSKÝ**



CZECH TECHNICAL UNIVERSITY IN PRAGUE

**Faculty of Civil Engineering
Department of Mechanics**

**Mesoscale Discrete Element Model for Concrete
and Its Combination with FEM**

DOCTORAL THESIS

Ing. Jan Stránský

Doctoral study programme: Civil Engineering

Branch of study: Physical and Material Engineering

Doctoral thesis supervisor: prof. Ing. Milan Jirásek, DrSc.

Prague, 2018

I would like to dedicate this thesis to my grandmother, who wished to have a copy, but passed away just a few days before it became completed. She always appreciated my academic achievements, taught me how to be patient and strong-willed and inspired me enormously to study and work hard.



CZECH TECHNICAL UNIVERSITY IN PRAGUE

Faculty of Civil Engineering
Thákurova 7, 166 29 Praha 6

DECLARATION

Ph.D. student's name: Jan Stránský

Title of doctoral thesis: Mesoscale Discrete Element Model for Concrete
and Its Combination with FEM

I hereby declare that this doctoral thesis is my own work and effort written under the guidance of my supervisor, prof. Ing. Milan Jirásek, DrSc.

All sources and other materials used have been quoted in the list of references.

The doctoral thesis was written in connection with research projects:

GAČR 106/08/1508,
SGS11/021/OHK1/1T/11,
SGS12/027/OHK1/1T/11,
SGS13/034/OHK1/1T/11,
SGS14/029/OHK1/1T/11,
SGS15/030/OHK1/1T/11.

In Prague, 31st January 2018

.....
signature

Abstrakt

Dizertační práce se zabývá různými aspekty metody diskretních prvků (DEM) a její aplikací pro modelování porušování betonu a také kombinací DEM s metodou konečných prvků (FEM).

Základní vlastnosti náhodných hustých částicových shluků (jelikož tyto jsou obvyklé počáteční nastavení DEM simulací) jsou analyzovány pro různý počet částic. Pružné vlastnosti takovýchto shluků jsou zkoumány analyticky i numericky. Numerické výrazy jsou odvozeny na základě mikroploškové teorie. Numerické výsledky jsou získány pomocí DEM a FEM simulací. Velmi dobré shody mezi analytickými a numerickými výsledky je dosaženo pro interakční poměr větší než 1.25. Analyticky odvozený plný tenzor pružné tuhosti se velmi dobře shoduje s numerickými výsledky i pro nižší hodnoty interakčního poměru, avšak hodnoty Youngova modulu pružnosti a Poissonova součinitele odvozené za předpokladu rovnoměrného rozdělení směrů vazeb vykazují jistou odchylku od numerických výsledků.

Nespojitost je základní vlastností DEM. V některých situacích je však žádoucí převést nespojitě veličiny (např. síly) na odpovídající spojitou veličinu (např. tenzor napětí). Je představeno vyhodnocení tenzoru napětí a couple stress tenzoru z nespojitých sil. Metoda je založena na principu virtuálních prací. Jsou představeny nové výrazy pro couple stress tenzor, jejichž výsledek je jedinečný a nezávislý na volbě počátku souřadnicového systému.

DEM i FEM mají své oblasti použití, někdy ale spolu mohou být vhodně zkombinovány. V souběžných kombinačních přístupech běží DEM i FEM simulace současně. Je představena kombinace FEM programu OOFEM a DEM programu YADE. Je popsáno několik různých přístupů (jmenovitě povrchové, objemové, víceúrovňové a kontaktní), každý z nich ilustrovaný na jednoduchém případě.

Sériová DEM–FEM kombinace (kdy DEM simulace probíhá první a její výsledek je převeden jako počáteční stav FEM simulace) poškozujícího se betonového materiálu je představena na příkladu jednoosého tlaku. Metoda prokázala schopnost poměrně dobře vystihnout přechod z DEM do FEM pro různé módy zatížení – mapování v různých stádiích (pružná oblast, vrchol pevnosti, změkčení atd.). Výsledky se nejvíce liší v těch oblastech zatížení, kde se samotné DEM a FEM materiálové modely liší nejvíce.

Ve stavební praxi je beton obvykle idealizován jako homogenní izotropní materiál. Některé aplikace však vyžadují popis betonu na nižší úrovni a musí se uvažovat nestejnorodosti. Je představen vývoj a výsledky nového mezoúrovňového modelu pro beton. Model uvažuje nestejnorodou mezoúroveň betonu (t.j. zrna kameniva a zónu rozhraní mezi kamenivem a matricí). Validace vzhledem k experimentálním výsledkům přebraným z literatury prokázala schopnost modelu realisticky vystihnout trendy různých materiálových vlastností (modulu pružnosti, tahové a tlakové pevnosti, lomové energie) vzhledem k mezoúrovňové struktuře materiálu.

Klíčová slova: Metoda diskretních prvků, metoda konečných prvků, kombinování metod, Python, beton, mezoúroveň

Abstract

The presented thesis deals with various aspects of the discrete element method (DEM) with application to modeling of concrete failure and combination of DEM with the finite element method (FEM).

Basic properties (e.g., isotropy) of random densely packed particle assemblies (as a usual initial DEM packing configuration) are analyzed for various numbers of particles. Elastic properties of such packings are investigated both analytically and numerically. The analytical formulas are derived based on the microplane theory. The numerical results are obtained by DEM and FEM simulations. A very good agreement between analytical and numerical results is found for interaction ratios greater than 1.25. For lower values of the interaction ratio, the analytically derived full stiffness tensor corresponds to the numerical results very well, however, the values of Young's modulus and Poisson's ratio estimated based on the assumption of uniform distribution of link directions exhibit a certain discrepancy from the numerical results.

The discrete nature is an essential feature of DEM. However, in some cases it is desirable to transform such discrete information (contact forces for instance) into its continuum counterpart (e.g., stress tensor). The evaluation of the stress tensor and couple stress tensor from discrete forces based on the principle of virtual work is reviewed. New formulas for the couple stress tensor, yielding a unique value of the couple stress tensor independent on the choice of the coordinate reference point, are presented and discussed.

Both DEM and FEM have their fields of application, however, in certain cases they can be combined and used together. In the concurrent coupling approach, both DEM and FEM simulations are run at the same time. Coupling of FEM code OOFEM and DEM code YADE is described. Several classes of coupling approaches (namely surface, direct volume, multiscale and contact) are addressed and illustrated on simple examples.

A DEM to FEM sequential coupling (in which case the DEM simulation is run first and the resulting state is converted into an initial state of the FEM simulation) of damaged concrete material is presented for the case of uniaxial compression. The method is proven to be able to capture the transition from DEM to FEM relatively well for several different loading scenarios – mapping at different stages (elastic range, peak load, softening regime, with or without unloading etc.). The most divergent results are obtained for the stages of loading where the DEM and FEM material models themselves differ the most.

In practical civil engineering, concrete is usually idealized as a homogeneous isotropic material. However, certain applications require description of concrete on a lower scale and heterogeneity has to be taken into account. The development and results of a new mesoscale discrete element model for concrete is described. The model takes into account the heterogeneous mesoscale structure of concrete (i.e., aggregates and interfacial transition zone between aggregates and matrix). The validation against experimental data from literature shows the ability of the model to realistically capture trends of various material properties (elastic modulus, tensile and compressive strength, fracture energy) with respect to the actual mesoscale structure of the material.

Keywords: Discrete Element Method, Finite Element Method, multimethod coupling, Python, concrete, mesoscale

Acknowledgements

I would like to express my sincere thanks and warmest gratitude to all those who encouraged and supported me throughout my Ph.D. study (accidental omissions in the following list do not mean disacknowledgements).

- First of all, I would like to express my sincere gratitude and thanks to my supervisor Milan Jirásek for his support, encouragement and patience during the whole study, for his personal and collegial attitude, the freedom that I have obtained in research directions and for being greatly inspiring both professionally and personally. It was a pleasure to cooperate with him. I would also like to thank him for his course Modeling of Localized Inelastic Deformation that I attended at the beginning of my Ph.D. studies and for organising annual bowling MK events.
- Grateful thanks go to other department members Bořek Patzák and Vít Šmilauer for valuable discussions and for the help with OOFEM. I am especially grateful to Jan Zeman, who determined the direction of my next study, for inspiration and for the honor to cooperate with him from my second university year until the Bachelor's thesis.
- I would also like to thank my department friends (listed in alphabetical order) Martin Doškář, Edita Dvořáková, Karolina Hájková, Jan Havelka, Petr Havlásek, Petr Hlaváček, Adéla Hlobilová, Martin Horák, Filip Kolařík, David Krybus, Karel Mikeš, Eva Myšáková, Michal Přinosil, Vladimír Šána, Václav Šmilauer, Karel Šobra, Jaroslav Vondřejc and others for valuable discussions, inspiration and for friendly atmosphere and fun at the department.
- The financial support by the industrial partner, by the Czech Science Foundation under project GAČR 106/08/1508 and by SGS projects of the Czech Technical University in Prague is also gratefully acknowledged.
- My respect and thanks go to the authors of great open-source codes Python, T_EX and L^AT_EX, Gnuplot, Linux and Ubuntu, Vim, YADE, OOFEM, etc., etc.
- Last but definitely not least, I am deeply indebted to all my family. I am grateful to my parents for their huge support and encouragement during (not only) the years of my study and for all of the sacrifices that they have made for me. I would like to thank my brother for countless discussions on various topics and his support during the thesis finalization.

The very last but the warmest and most sincere thank belongs to my wife Katka and sons Pěťa and Adámek. Words cannot express how grateful I am for their continuous huge love, support, encouragement, inspiration, for what they all taught me and for the final motivation to complete the thesis. Their patience with me during the finalization period, when my presence at home was rather occasional, is truly admirable.

Contents

Abstract	iii
Acknowledgements	v
List of Figures	xi
List of Tables	xiii
1 Introduction	1
1.1 Research objectives	2
1.2 Thesis outline	3
I Discrete Element Method	7
2 Discrete element method	9
2.1 Brief classification	9
2.2 YADE	11
2.3 DEM extensions	11
2.4 Initial packing	12
2.5 Cohesive particle model for concrete	13
2.5.1 Contact kinematics	13
2.5.2 Constitutive law	15
2.5.3 Structural behavior	18
3 Macroscopic elastic properties of DEM models	21
3.1 Theoretical analytical values	22
3.2 Static FEM solution	25
3.2.1 Periodic boundary conditions	27
3.2.2 OOFEM implementation	29
3.2.3 Evaluation	29
3.3 Dynamic DEM solution	29
3.4 Results	30
3.4.1 Isotropy of elastic constants	30
3.4.2 Comparison of analytical and numerical results	34
4 Discrete stress tensor	37
4.1 Derivation based on virtual work	37
4.1.1 Virtual work of discrete external forces	38
4.1.2 Virtual work of discrete internal forces	40
4.1.3 Summary	43
4.2 Derivation based on equilibrium conditions	43
4.2.1 External forces	43
4.2.2 Internal forces	44
4.3 Examples	44

II	DEM – FEM coupling	49
5	Concurrent DEM – FEM coupling	53
5.1	Surface coupling	53
5.1.1	Example	54
5.2	Volume coupling	54
5.2.1	Example	55
5.3	Multiscale coupling	56
5.3.1	Example	56
5.4	Contact coupling	57
5.4.1	Example	57
6	Sequential DEM – FEM coupling	61
6.1	Background	61
6.1.1	Damage–plastic model for concrete	62
6.1.2	Cohesive particle model for concrete	63
6.2	Theory	63
6.2.1	Stress tensor	63
6.2.2	Concrete damage	63
6.2.3	Mapping	66
6.3	Example - uniaxial compression	68
III	Mesoscale Discrete Element Model for Concrete	75
7	State of the art	79
7.1	Mesoscale geometry	79
7.2	Material models for mortar and aggregates	80
7.3	Interface transition zone	80
8	New mesoscale discrete element model for concrete	83
8.1	New model definition	83
8.2	Model validation	84
8.2.1	Experiment [12, 13, 69]	86
IV	Conclusions	91
9	Conclusions	93
	References	95
V	Appendices	105
A	Mathematical and physical concepts and notations	107
A.1	Tensors	107
A.1.1	Algebraic operations and properties	107
A.1.2	Special tensor instances and identities	109
A.2	Differential calculus	111

A.3	Cosserat micropolar continuum mechanics	113
A.3.1	Kinematic equations	113
A.3.2	Equilibrium equations	116
A.3.3	Principle of virtual work	117
A.3.4	Classical Boltzmann continuum	118
A.4	Surface integrals over unit sphere	119
A.4.1	Spherical coordinate system	120
A.4.2	A more general derivation	121
A.5	Miscellaneous	123
B	Publications of the author	125

List of Figures

2.1	2D illustration of a periodic packing	12
2.2	Packing fraction of dynamic periodic compaction	13
2.3	Isotropy of links for $N = 4000$ and $\iota_r = 1.5$	13
2.4	2D illustration of the normal displacement of the link	14
2.5	2D illustration of the shear displacement of the link	15
2.6	Physical meaning of CPM material parameters in normal direction	16
2.7	CPM in normal direction	16
2.8	Plasticity surface in shear direction	17
2.9	Stress strain diagram in shear direction	17
2.10	Uniaxial tension and compression results of CPM model	19
3.1	Illustration of the global and local coordinate system of the link	27
3.2	2D example of periodic cell and “periodic” links	27
3.3	Stability of mean values of E and ν	31
3.4	Relative anisotropy of Young’s modulus $\Delta E/E$ for various N	32
3.5	Relative anisotropy of Poisson’s ratio $\Delta \nu/\nu$ for various N	32
3.6	Relative deviation from mean shear modulus $\Delta G/G$ for various N	33
3.7	Relative deviation of “zero” elements of stiffness matrix Δ/E for various N	33
3.8	Relation between macro- and microscopic parameters for $\iota_r = 1.05$	34
3.9	Relation between macro- and microscopic parameters for $\iota_r = 1.25$	35
3.10	Relation between macro- and microscopic parameters for $\iota_r = 1.50$	35
3.11	Relation between macro- and microscopic parameters for $\iota_r = 2.00$	36
4.1	Illustration of virtual work of internal forces acting on rigid particles	41
5.1	Surface coupling illustration	54
5.2	Volume coupling illustration	55
5.3	Multiscale coupling illustration	56
5.4	Contact coupling illustration	57
5.5	Impact on a simply supported beam at different stages	59
5.6	Collision of three elastic particles at different stages	59
5.7	Impact on a cantilever at different stages	60
5.8	Uniaxial strain test at different stages	60
6.1	Stress-strain diagram of DPM model in uniaxial tension.	62
6.2	Uniaxial stress-strain diagram of one link of CPM model.	63
6.3	Contact points, normals and damage.	64
6.4	Stress-strain diagrams for individual models	69
6.5	Chosen damage transformation law reflecting residual strength of CPM model	69
6.6	Results of mapping at monotonic loading	70
6.7	Results of mapping at unloaded state	71
7.1	Examples of geometrical representation of aggregates	80
7.2	Examples of artificial geometry	81
7.3	Illustration of aggregate representation as a cluster of DEM particles	81

7.4	Interface model	82
7.5	Illustration of material models	82
7.6	Illustration of constitutive law	82
7.7	ITZ modeled by the same material model	82
8.1	Illustration of MCPM geometry definition	83
8.2	Illustration of clustered aggregate	84
8.3	ITZ models in literature	85
8.4	Influence of maximum aggregate size on fracture energy	86
8.5	Influence of maximum aggregate size on mechanical properties	87
8.6	Comparison of simulations and experiment	88
A.1	2D representation of stresses and couple stresses on elementary cube	116
A.2	Spherical coordinate system	120

List of Tables

2.1	CPM material parameters and history variables	15
2.2	Material parameters used for illustrative stress-strain curves in figure 2.10	19
4.1	2D illustrations of stress and couple stress tensors	45
6.1	Principal values of damage tensor for various damages	67
8.1	Concrete compositions	86
A.1	2D representation of Cosserat strain	115

1 Introduction

Concrete is a composite material composed of inclusions (gravel and sand aggregates) embedded in a cement (or similar binder) matrix and is the most widely used building material. Therefore it has been in various contexts subjected to extensive research. From material modeling point of view, the objective is to describe the behavior of concrete under different circumstances and help to predict its behavior in specific situations, e.g., predict deflections of a concrete bridge during its lifetime. The range of methods and approaches to describe concrete behavior is wide – models on different scales (from atomistic to structural level), applicability to specific load cases (from statics to explosive impact dynamics, uniaxial vs. multiaxial loadings . . .), application in the context of different numerical methods, etc. The right approach depends on purpose, resources (on computational simulation time for instance), available input data and so on.

In practical civil engineering, concrete is usually idealized as a homogeneous isotropic material. Indeed, considering heterogeneities (aggregates) in analyses of building-sized structures would be very impractical or even impossible. However, certain applications require description of concrete on lower than structural scales and heterogeneity (e.g., presence of aggregates) has to be taken into account.

The basic behavior and structural response of concrete structures may be described analytically (for example a beam structure in the elastic range). Introducing more and more enhancements and features of the models leads to analytical unsolvability and numerical methods, usually with the help of computers, have to be introduced.

Numerical simulations are an indispensable part of the current engineering and science development. For different engineering areas there are different numerical methods used. In solid phase mechanics, the leading methods are the finite element method (FEM) and the discrete (distinct) element method (DEM). FEM is rigorously derived from the continuum theory and is being used for the description of deformable continuous bodies, while DEM describes particulate materials, usually modeled by perfectly rigid particles and their interactions determined from fictitious overlaps of these rigid particles.

Often, an engineering problem can be modeled using only one of the aforementioned methods. A steel beam would be simulated by FEM, a small assembly of gravel particles by DEM. But what if we wanted to simulate an impact of the steel bar on the gravel? One possible approach would be to split the problem into two domains (the steel part modeled by FEM and the gravel part modeled by DEM) and appropriately *couple* them.

Usually, the solution is performed by a computer program, which is focused on a narrower or wider class of problems (such as solid mechanics, fluid dynamics, heat analysis, DEM etc.). If a combination of two classes of problems is required (coupling of mechanical and heat analysis for instance), it is often possible to find a code allowing such approach. However, in some cases, there exists no program that can solve the desired combination of problems. For instance, it is possible to couple mechanical and heat analysis within the chosen code, but we would like to use a special material model for mechanical analysis, which is not implemented.

One possible approach to deal with such situation would be to write a new or extend an existing program implementing the requested features. Another possible approach would be to use existing independently developed codes, each one focused on a specific class of problems, and “glue” them together.

There are countless software programs for both FEM and DEM. Some of them are commercial (usually) without possibility to change the code and adjust the behavior to our requirements (combination with another software for instance). However, there exist programs with open source code, which the user can modify, possibly for coupling with other programs. In this thesis, coupling of FEM code OOFEM and DEM code YADE is described and illustrated.

The presented research was partially supported by an industrial partner. Some results are not presented due to confidentiality reasons.

The \LaTeX source code of the thesis and errata together with the source code of all presented simulations and results will be available on the author's GitHub sites.

1.1 Research objectives

The principal research objectives of this thesis are:

1. To investigate basic properties of particle models, namely the relation between micro- and macroscopic elastic properties of random dense packings in terms of analytical formulas and results of numerical simulations. Preparation and properties of random dense packings should be investigated beforehand.
2. To develop open source tools for combination of the discrete element method and the finite element method. Several classes of combination approaches together with simple examples should be addressed.
3. To develop a mesoscale discrete element model for concrete. The model should take into account the effect of aggregates and the interfacial transition zone (ITZ) between aggregates and the matrix. The model should be validated against experimental data from available literature.

1.2 Thesis outline

The thesis is organized into several main parts.

- The first part deals with the discrete element method in general. A general introduction to DEM is the topic of chapter 2. It also contains a brief description of the cohesive particle model for concrete (CPM) which is used at several places in the thesis. Chapter 3 investigates the relation of micro- and macroscopic properties of particle models. Analytical formulas are described in detail and are compared to the results of DEM and FEM numerical simulations. The last chapter of the first part gives an review of the evaluation of the stress tensor and couple stress tensor from discrete forces. New formulas for the couple stress tensor are presented and discussed.
- The topic of the second part is the combination of the finite element method and the discrete element method. Concurrent coupling methods (in which case both FEM and DEM simulations are run at the same time) are described in chapter 5. Sequential DEM–FEM coupling (in which case the DEM simulation is run first and the resulting state is converted into an initial state of the FEM simulation) with the application to uniaxial compression of concrete is described in chapter 6.
- The third part describes the development and results of the new mesoscale discrete element model for concrete. The literature overview is given in chapter 7. The new model itself is presented in chapter 8.
- Appendix A summarizes mathematical and physical notation, terminology, conventions and “generally known” theory used throughout the thesis.
- Publications of the author are listed in appendix B.

Part I.

Discrete Element Method

2 Discrete element method

The discrete (or distinct) element method (DEM) is a widely used numerical tool of solid mechanics, mostly for dynamic problems, yet most widely for short-time events. DEM represents the material as a set of perfectly rigid units (referred to as discrete elements, particles, bodies etc.). The name *particle(s)* will be used in this thesis for individual discrete element(s). Particles interact with each other according to defined constitutive law(s).

DEM solves numerically equations of motion of individual particles P .

$$\mathbf{f} = m\ddot{\mathbf{u}} \qquad \mathbf{c} = \mathbf{I} \cdot \ddot{\boldsymbol{\phi}} \qquad (2.1)$$

\mathbf{f} , m , $\ddot{\mathbf{u}}$, \mathbf{c} , \mathbf{I} and $\ddot{\boldsymbol{\phi}}$ denotes force vector, mass, acceleration vector, force moment (also referred as couple) vector, inertia tensor and angular acceleration vector, respectively. Forces and moments occurring in the equations of motion can be of prescribed nature (e.g., gravity, drag force or imposed boundary conditions) or are the result of inter-particle interactions. According to the specific use, these interactions are also denoted as links, bonds etc. The name *link(s)* will be used in this thesis for individual inter-particle interactions.

In its basic version, DEM is naturally applicable for modeling of granular materials (as in its very first application [21]). Using different particle shapes and different contact laws, DEM can take various forms. See, e.g., [91] or the next classification section for more information.

From computational point of view, detection of new contacts is an important part of the numerical solution. A naive approach (testing each particle with all particles) has $O(n^2)$ complexity and therefore more sophisticated approaches must be applied for larger scale problems. Nowadays standard collision detection algorithms work with $O(n \log n)$ complexity [91]. For special cases, contact detection algorithms even with linear complexity $O(n)$ were invented. The topic of contact detection is not addressed in this thesis in detail, interested readers are referred to [91, 65].

The equations of motion can be solved numerically using an implicit or explicit scheme. The collisions (and therefore the stiffness matrix of the system) are not known in advance. A “small” change of positions of particles can cause a sudden (“big”) change of the stiffness of the system. For this reason, implicit integration schemes are in general not suitable for numerical solution and an explicit time integration scheme is usually applied to solve equations of motion (considering only the current configuration of the system to evaluate the configuration in the next time step). Using an explicit integration scheme implies using a sufficiently short time step to keep the simulation stable.

2.1 Brief classification

In general, DEM can be classified and its variants differ by many aspects. Some of them are listed in this section.

Spatial dimensions

The solution can be formulated in 2D or 3D. In all cases below, the 3D case is considered, although the corresponding 2D alternative is possible. For instance, 2 translations

and 1 rotation in 2D instead of 3 translations and 3 rotations in 3D or ellipse 2D analogy to 3D ellipsoid.

Shapes

Particles can be of various shapes. The simplest case is spherical shape. Other shapes may be ellipsoids, polyhedrons, Minkowski sums (“rounded polyhedrons”), surfaces defined by harmonic functions etc.

Discretization

DEM particles can either represent real particles (e.g., sand or gravel grains, masonry stones or bricks etc.) or may be just artificial discretization units (as shown, e.g., in part III).

Degrees of freedom

Particles can possess 3 degrees of freedom (translation) or 6 degrees of freedom (translation and rotation).

Constitutive laws and contact kinematics

Interaction constitutive laws define the interaction force (force to be applied on both interacting particles with opposite direction) based on mutual configuration of interacting particles. Simple models (including those described in this thesis) evaluate force based on the mutual displacement and/or rotation of interacting particles. Other options (not considered further in the thesis, see [91] for more details) may be force dependent on the overlapping volume (used in YADE for polyhedral particles) or potential particles approach.

The basic mutual displacement-rotation-based modes are normal displacement, shear displacement, bending mode and twisting mode. The considered mutual displacement-rotation modes are strongly related to the considered constitutive law. For instance, if the constitutive law is defined only in terms of the normal and shear force, evaluation of the bending and twisting modes is omitted to save computational time. In the case of normal and shear displacement and normal and shear forces, the basic constitutive quantities are normal and shear stiffness \bar{k}_N and \bar{k}_T . The physical dimension of such stiffness is [N/m] as it relates force [N] and displacement [m].

DEM works with discrete forces and displacements. However, it is usual that constitutive models are formulated in terms of stresses and strains. The link is then considered as a fictitious bar with fictitious length L , cross section area A and material stiffness \bar{E} and \bar{G} . Strain can be defined as displacement divided by the fictitious length, stress as force divided by the fictitious cross section area. The basic constitutive quantities are then normal modulus \bar{E} and shear modulus \bar{G} of the fictitious material. The physical dimension of such stiffness is [N/m²] as it relates stress [N/m²] and strain [-]. The relation of the stiffnesses is given as

$$\bar{k}_N = \bar{E} \frac{A}{L}. \quad (2.2)$$

For instance, the length may be considered as the sum of radii of interacting particles and cross section proportional to the average radius of interacting particles (e.g., $A = r^2$ or $A = \pi r^2$).

Cohesive links

Links between particles may be non-cohesive – they are deleted if there is no overlap of the interacting particles – or cohesive – force is transmitted even if the interacting particles are “farther away” from each other. Usually the cohesive approach models an initially continuous material with the possible generation of discontinuities. If a DEM model contains cohesive links (bonds), it is sometimes referred to as Bonded Particle Model (BPM).

2.2 YADE

YADE (Yet Another Dynamic Engine) [91] is an open source software for DEM analysis. Its core is written in C++ (providing efficient execution of time consuming routines), user interface is written in Python (modern dynamic object oriented scripting language, providing easy to use scripting while preserving the C++ efficiency). Extensible object oriented architecture allows independent implementation of new features - new material model or new particle shapes for instance.

All DEM results presented in this thesis were computed using YADE software.

2.3 DEM extensions

Clumps - rigid compounds

Several particles can be clumped together to form a multi-particle rigid body. This approach can be applied to increase the mass of “macro-particles” and thus increase the critical time step or to approximate a complex shape with a set of simple shapes (to approximate a polyhedron with spheres for instance). In the latter case, the mass and inertia of the resulting compound are defined independently of its constituents.

Clumps are one option how to model stiffer and stronger grains, e.g., concrete aggregates within mortar matrix.

Periodic boundary conditions

Periodic boundary conditions (or more precisely periodic contact detection and interaction evaluation) is a technique to avoid boundary effects or to decrease the domain size of problems with uniform strain or a theoretically infinite domain.

Periodic contact detection takes into account also interaction of particles with periodic images of other particles. See figure 2.1 for illustration. The periodic interaction evaluation (between particles JK for instance) is then performed as if particle K was placed at position K' instead of its real position.

The periodicity is defined by the size of the periodic cell and its transformation (the deformation gradient \mathbf{F}). Change of the transformation \mathbf{F} influences the position of periodic images of real particles and therefore inter-particle forces (see figure 2.1). The change of \mathbf{F} can thus be used to impose macroscopic deformation.

See [91, 92] for more technical details (description of periodic contact detection algorithms for instance). As discussed in [88], this kind of periodic boundary conditions is not suitable for modeling problems that involve strain localization.

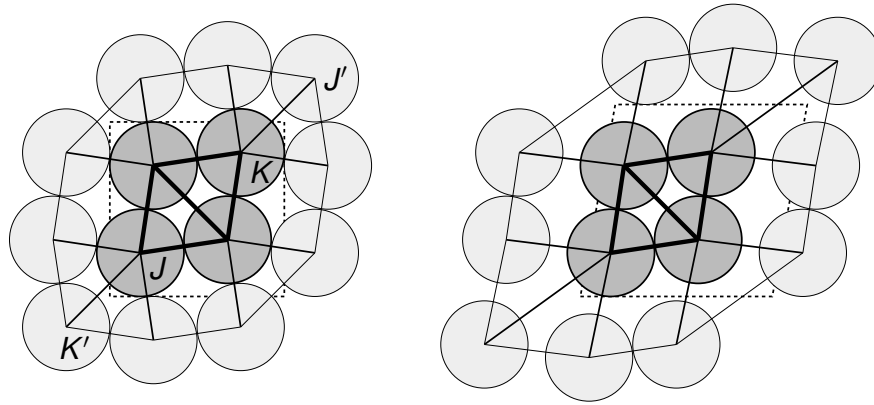


Figure 2.1: 2D illustration of a periodic packing with initial (left) and deformed (right) periodic cell

2.4 Initial packing

The initial particle packing is an important part of DEM simulations (similarly to FEM mesh generation). Regular packings are easy and quick to generate, but are often not suitable for realistic simulations (exhibiting predefined directions of defects, having given anisotropy etc.). Therefore the initial sample is usually a random packing of particles. Although being random, it must at the same time satisfy certain criteria and properties (porosity, particle size distribution, coordination number, packing fraction etc.).

Two main classes of approaches exist for the initial packing preparation: geometric (see, e.g., [48]) and dynamic (see, e.g., [91]). The geometric approaches generate positions and sizes of particles purely based on geometry (once again similarly to mesh generation), while dynamic approaches run actually an auxiliary DEM simulation (to prepare initial data for the desired DEM simulation).

Dynamic approaches usually start with random loose packing (which is easy to generate) and continue with compaction. The compaction stage may be, e.g., gravity deposition or triaxial compression. In the case of the triaxial compression, the sample is first compressed up to a certain level of hydrostatic stress and then unloaded to a defined residual stress level.

A problem of dynamic packing generation is that the required time increases significantly for the increasing number of particles. For the case of triaxial compression as the compaction phase, one possible solution to save time is to compress only a limited amount of particles *periodically*, resulting in a periodic unit cell. The periodic cell is then copied wherever needed for the desired initial sample and cropped to meet geometric requirements. With this approach, a sample of any size is generated at (almost) constant time.

Figure 2.2 shows packing fractions of the periodic compaction for various numbers of particles with a convergence to the value ≈ 0.61 . Figure 2.3 shows spatial isotropy of inter-particle links. For the evaluation, only link directions with absolute value of z coordinate less than 0.7 were extracted. Then they were projected into xy plane, converted to angle in the range $[0, \pi)$ and put into 32 bins. Amounts of directions in corresponding bins are plotted. The grey circle means average value.

As a consequence of this geometric isotropy, the resulting elastic material parameters are (almost) isotropic, too. See chapter 3 for more information.

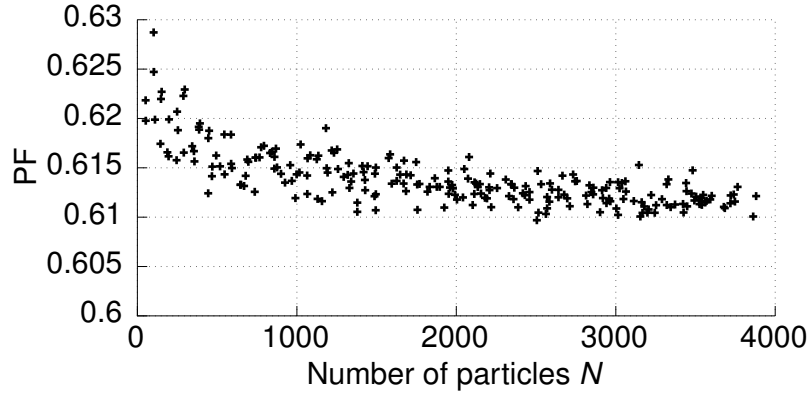


Figure 2.2: Packing fraction of dynamic periodic compaction for various numbers of particles

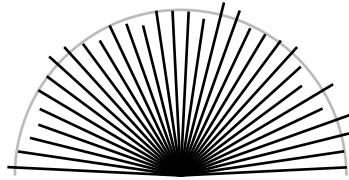


Figure 2.3: Isotropy of links for $N = 4000$ and $l_r = 1.5$

2.5 Cohesive particle model for concrete

The cohesive particle model for concrete (CPM) is a material model for the discrete element method with the aim to model concrete failure. The model is described in detail in [92] together with its extensions for confined loadings and loading at high strain rates. Only its basic version needed for the purposes of the thesis is reviewed in this section. Furthermore, only the version for spherical packings with uniform radius is considered.

The model is formulated in terms of stress and strain. It evaluates normal and shear stress based on normal and shear strain, material parameters and history variables. Material parameters and history variables are listed in table 2.1. Strain and stress evaluation is described in the following subsections.

2.5.1 Contact kinematics

Consider two spherical particles J and K with centers \mathbf{p}_J and \mathbf{p}_K , respectively.

When a link (cohesive or not) between the two particles is created, the original length of the link

$$L = \|\mathbf{p}_K^0 - \mathbf{p}_J^0\|. \quad (2.3)$$

is computed and stored. The superscript 0 denotes the value at the time of the link creation.

2.5.1.1 Normal strain

Normal contact displacement of the link is defined as the difference between the current and original link length

$$u_N = \|\mathbf{p}_K - \mathbf{p}_J\| - L. \quad (2.4)$$

See figure 2.4.

The normal strain is simply the normal displacement divided by the original length of the link:

$$\varepsilon_N = \frac{u_N}{L} \quad \varepsilon_N = \varepsilon_N \mathbf{n}. \quad (2.5)$$

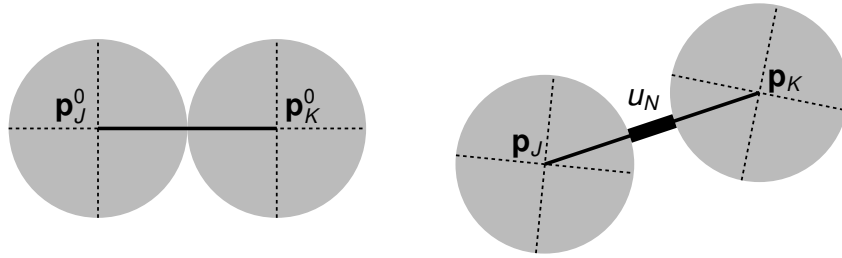


Figure 2.4: 2D illustration of the normal displacement of the link

2.5.1.2 Shear strain

While the normal displacement and strain are computed directly, the situation with shear displacement and strain is somewhat more complicated. The link geometry is defined by the two centers, uniquely defining the contact point

$$\mathbf{c} = \frac{1}{2}(\mathbf{p}_J + \mathbf{p}_K), \quad (2.6)$$

the link direction expressed by a unit vector

$$\mathbf{n} = \frac{\mathbf{p}_K - \mathbf{p}_J}{\|\mathbf{p}_K - \mathbf{p}_J\|} \quad (2.7)$$

and a plane perpendicular to this direction. The local coordinate system is therefore not uniquely defined. For this reason, the shear components are evaluated in the global coordinate system. In YADE implementation, the shear displacement is updated incrementally in each integration step. The increment consists in projecting the previous shear displacement such that it remains perpendicular to the current direction vector. Then the actual shear displacement increment is computed with respect to current \mathbf{n} and linear and angular velocities of interacting spheres

$$\mathbf{v}_{JK} = (\mathbf{v}_K + d_K \mathbf{n} \times \boldsymbol{\omega}_K) - (\mathbf{v}_J + d_J \mathbf{n} \times \boldsymbol{\omega}_J) \quad (2.8)$$

projected to the direction vector

$$\mathbf{v}_{JK}^\perp = \mathbf{v}_{JK} - \mathbf{n}(\mathbf{n} \cdot \mathbf{v}_{JK}) \quad (2.9)$$

The values d_P are distance from the contact point to the center of corresponding particle P

$$d_P = \|\mathbf{c} - \mathbf{p}_P\|, \quad (2.10)$$

which reduces to

$$d_J = d_K = \frac{1}{2} \|\mathbf{p}_K - \mathbf{p}_J\| \quad (2.11)$$

for the case of equally sized spheres.

Shear displacement increment is computed as the shear velocity multiplied by time increment

$$\Delta \mathbf{u}_T = \mathbf{v}_{JK}^\perp \Delta t. \quad (2.12)$$

See [91, 92] or figure 2.5 for more details.

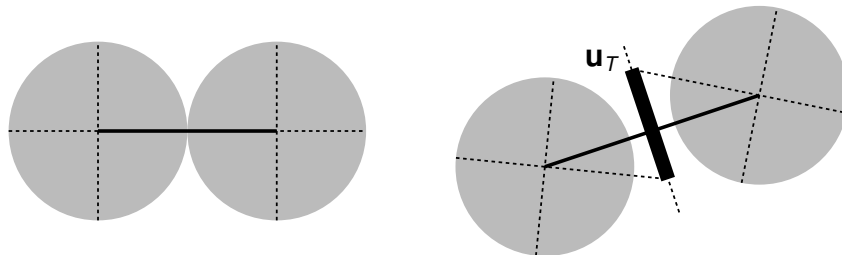


Figure 2.5: 2D illustration of the shear displacement of the link

2.5.2 Constitutive law

Table 2.1: CPM material parameters and history variables

Material parameter	symbol	units
normal modulus	\bar{E}	Pa
limit elastic strain	ε_0	-
strain defining softening	ε_f	-
shear modulus	\bar{G}	Pa
initial cohesion	c_0	Pa
friction angle	φ	-

History variable	symbol	units
damage variable	ω	-
historically maximum strain	κ	-
shear plastic strain	ε_T^p	-

Forces needed by the DEM program for equations of motion are simply the stress values multiplied by the cross section area:

$$f_N = A\sigma_N \quad \mathbf{f}_N = f_N \mathbf{n} \quad \mathbf{f}_T = A\boldsymbol{\sigma}_T. \quad (2.13)$$

The cross section area is considered as

$$A = \pi r^2, \quad (2.14)$$

where r is the radius of the spheres.

2.5.2.1 Normal stress

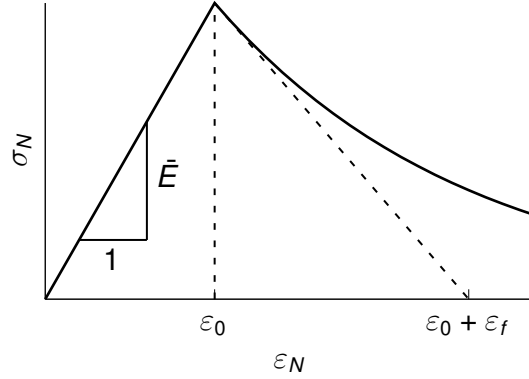


Figure 2.6: Physical meaning of CPM material parameters in normal direction

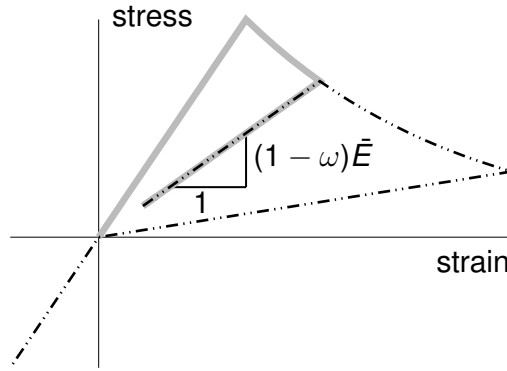


Figure 2.7: CPM in normal direction - illustration of unloading and reloading and stiffness reduction due to damage

Constitutive law in the normal direction is inspired by (1D) damage mechanics and defines normal stress σ_N in terms of normal strain ε_N

$$\sigma_N = [1 - \omega H(\varepsilon_N)] \bar{E} \varepsilon_N. \quad (2.15)$$

\bar{E} is the normal modulus and defines the elastic slope in the normal direction. $\omega \in [0, 1]$ is the damage variable which influences stiffness for unloading and reloading in the tensile regime. The Heaviside function $H(\varepsilon_N)$ deactivates damage influence in compression, which physically corresponds to crack closure. ω is computed based on the damage evolution function g defined in terms of historically maximum normal strain κ and material parameters ε_0 and ε_f :

$$\kappa = \max_t(\varepsilon_N) \quad (2.16)$$

$$\omega = g(\kappa) = 1 - \frac{\varepsilon_0}{\kappa} \exp\left(-\frac{\kappa - \varepsilon_0}{\varepsilon_f}\right) \quad (2.17)$$

ε_0 defines the elastic limit strain (the product $\bar{E}\varepsilon_0$ equals the link tensile strength). ε_f defines the initial softening slope and therefore controls the softening branch. See figures 2.6 and 2.7 for illustration.

2.5.2.2 Shear stresses

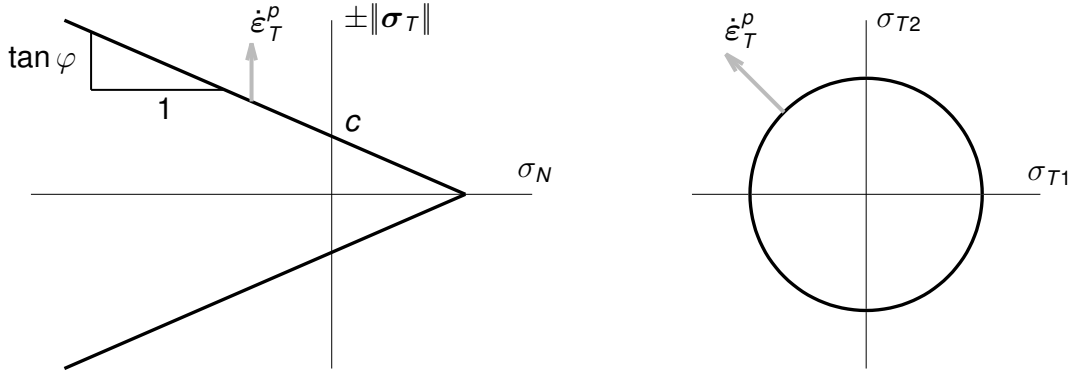


Figure 2.8: Plasticity surface in shear direction

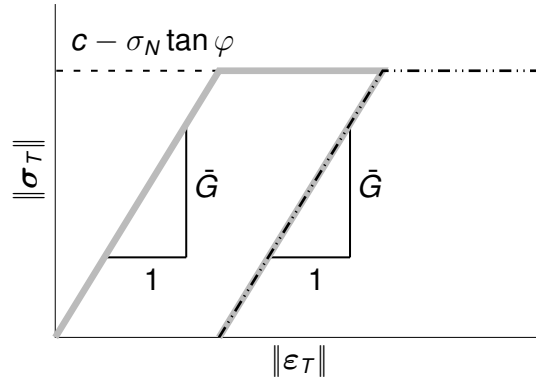


Figure 2.9: Stress strain diagram in shear direction

Constitutive law in the shear direction is inspired by plasticity and defines shear stress σ_T in terms of shear strain ε_T

$$\sigma_T = \bar{G}(\varepsilon_T - \varepsilon_T^p). \quad (2.18)$$

\bar{G} is the shear modulus and defines the elastic slope in the shear direction. ε_T^p is the shear plastic strain.

The shear stress is limited by the Mohr-Coulomb-like plasticity condition

$$f(\sigma_N, \sigma_T) = \|\sigma_T\| - (c - \sigma_N \tan \varphi) \leq 0 \quad c = (1 - \omega)c_0. \quad (2.19)$$

Cohesion c is computed from material parameter initial cohesion c_0 and the damage variable ω and defines the limit shear stress in pure shear loading. Internal angle φ determines the influence of normal stress on the plasticity condition. See figures 2.8 and 2.9 for illustration.

The non-associated plastic flow rule

$$\dot{\varepsilon}_T^p = \dot{\lambda} \frac{\sigma_T}{\|\sigma_T\|} \quad (2.20)$$

is chosen for computational reasons. The stress return is then simply the radial return, which can be evaluated directly (does not involve any iterative method). Furthermore, the

plasticity in shear does not influence the normal direction. As a result, the normal stress can be directly evaluated first (independently on the shear direction) and the shear stress is directly evaluated afterwards (with already known damage variable ω).

2.5.3 Structural behavior

Figure 2.10 shows results of uniaxial tension and uniaxial compression tests for several sets of material parameters. The tests were performed on a $50 \times 50 \times 50$ mm cubic sample containing $\approx 50,000$ particles, each of size (diameter) 2 mm. The boundary conditions are imposed by prescribing the velocity of top and bottom boundary layers of particles. The boundary particles are free to move in the lateral direction. The initial cohesive links were created considering interaction ratio $\iota_r = 1.5$.

In this illustrative example, the results are structural (macroscopic) Young's modulus E , tensile strength f_t and compressive strength f_c . The material parameters are \bar{E} , \bar{G} , ε_0 , ε_f , c and φ , see table 2.1. In general, the macroscopic quantities could be considered to depend on all material parameters:

$$E = f(\bar{E}, \bar{G}, \varepsilon_0, \varepsilon_f, c, \varphi) \quad (2.21)$$

$$f_t = f(\bar{E}, \bar{G}, \varepsilon_0, \varepsilon_f, c, \varphi) \quad (2.22)$$

$$f_c = f(\bar{E}, \bar{G}, \varepsilon_0, \varepsilon_f, c, \varphi). \quad (2.23)$$

Using the dimensional analysis, both micro- and macroscopic parameters can be transformed into a set of dimensionally independent or dimensionless parameters. The initial functions $f(\bullet)$ are transformed into new functions $\pi(\bullet)$. Firstly, macroscopic elastic parameters depend only on microscopic elastic parameters (as discussed in chapter 3):

$$E = \bar{E} \pi_E \left(\frac{\bar{G}}{\bar{E}} \right). \quad (2.24)$$

The inelastic parameters are transformed in a similar way:

$$f_t = \bar{E} \varepsilon_0 \pi_{f_t} \left(\frac{\varepsilon_f}{\varepsilon_0}, \frac{c}{\bar{E} \varepsilon_0}, \varphi \right) \quad (2.25)$$

$$f_r = \frac{f_c}{f_t} = \pi_{f_r} \left(\frac{\varepsilon_f}{\varepsilon_0}, \frac{c}{\bar{E} \varepsilon_0}, \varphi \right). \quad (2.26)$$

$\bar{E} \varepsilon_0$ represents the link tensile strength, $\varepsilon_f/\varepsilon_0$ relative ductility and $c/(\bar{E} \varepsilon_0)$ relative cohesion.

Figure 2.10 shows results for varying link stiffness, link strength and both link stiffness and link strength. The other quantities (ε_0 , φ , $\varepsilon_f/\varepsilon_0$ and $c/(\bar{E} \varepsilon_0)$) are the same for all four simulations. The macroscopic response is close to the theoretical expectations and therefore the macroscopic stiffness and strength can be easily estimated based on the link stiffness and link tensile strength. This approach is applied in chapter 8.

Table 2.2: Material parameters used for illustrative stress-strain curves in figure 2.10

simulation	\bar{E}/\bar{E}_1	$(\bar{E}\varepsilon_0)/(\bar{E}/\varepsilon_0)_1$
1	1	1
2	1	2
3	2	1
4	2	2

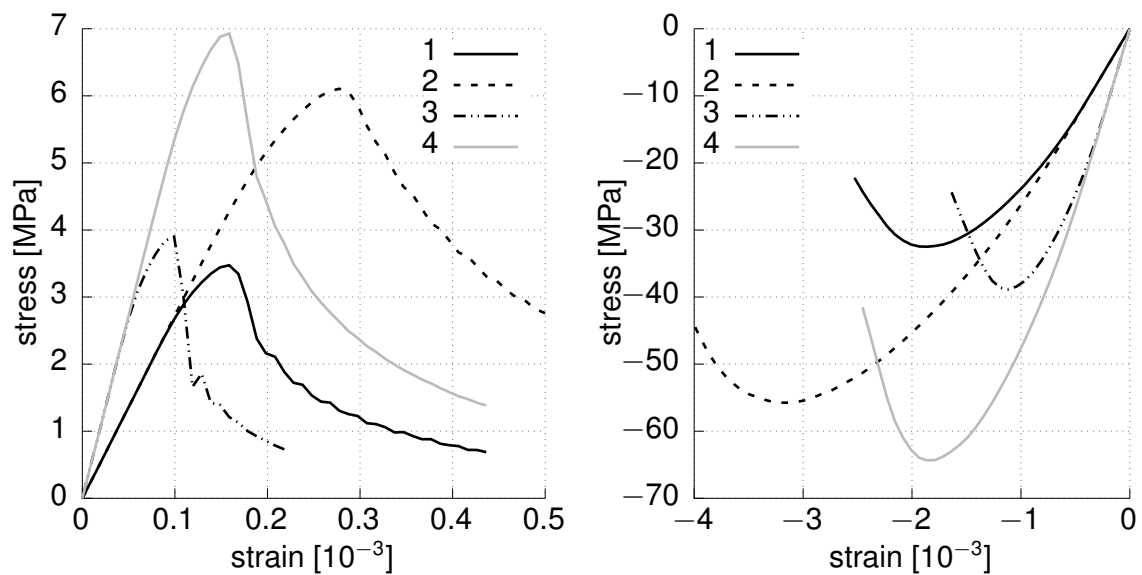


Figure 2.10: Uniaxial tension and compression results of CPM model with material parameters according to table 2.2

3 Macroscopic elastic properties of DEM models

The particle model investigated in this chapter consists of rigid spheres with uniform radius r connected by links that can transmit normal stress and shear stress. Each particle possesses six degrees of freedom, three translations and three rotations.

Initially, particles whose center distance L is less than $2r\iota_r$ (where ι_r is called interaction ratio) are connected by cohesive links. Each link is characterized by its length L (distance between centers of connected particles), unit normal vector \mathbf{n} and fictitious cross section area

$$A = \alpha r^2. \quad (3.1)$$

α may differ for specific constitutive law formulations, usual values are $\alpha = 1$ or $\alpha = \pi$.

Links in our model have normal and shear (or transversal) elastic fictitious material stiffness \bar{E} and \bar{G} [Pa] and normal and shear link stiffness $\bar{k}_N = \frac{\bar{E}A}{L}$ and $\bar{k}_T = \frac{\bar{G}A}{L}$ [N/m] (see section 2.5).

In a cube of dimension C and volume $V = C^3$ consider a random, densely packed assembly of spherical particles with radius r (see section 2.4). If the number of particles N is high enough, the assembly behaves macroscopically as an isotropic material. The elastic properties of that macroscopic material are determined by two material constants, for example Young's modulus E and Poisson ratio ν . In a very general case, we can express the macroscopic material properties as functions of all relevant variables:

$$E = f_E(\bar{E}, \bar{G}, r, \iota_r, C, N, A) \quad (3.2)$$

$$\nu = f_\nu(\bar{E}, \bar{G}, r, \iota_r, C, N, A) \quad (3.3)$$

Using dimensional analysis we can identify two dimensionally independent variables (e.g., \bar{E} and r) and two dimensionless variables ι_r and N . Applying Buckingham π theorem, we can rewrite equations (3.2) and (3.3) in terms of new dimensionless variables as

$$\frac{E}{\bar{E}} = \pi_E \left(\frac{\bar{G}}{\bar{E}}, \frac{r^2}{A}, \frac{r}{C}, \iota_r, N \right) \quad (3.4)$$

$$\nu = \pi_\nu \left(\frac{\bar{G}}{\bar{E}}, \frac{r^2}{A}, \frac{r}{C}, \iota_r, N \right) \quad (3.5)$$

Based on physical considerations, most of the dimensionless variables on the right side of (3.4) and (3.5) can be eliminated:

In principle, the number of particles N could be considered as independent of the relative particle size r/C . However, we are interested in the behavior of densely packed assemblies of particles, which are prepared by a simulated compaction process. It turns out that, for large values of N , the packing fraction

$$PF = \frac{V_{particles}}{V_{total}} = \frac{4\pi Nr^3}{3C^3} \quad (3.6)$$

tends to a constant, approximately equal to 0.612, which is close to the value 0.64 (theoretical maximum packing fraction for random close packing [96]), see section 2.4. Therefore,

the ratio r/C for such dense assemblies can be determined from N and does not need to be considered as an independent variable.

Furthermore, as N tends to infinity, the macroscopic properties approach a certain limit, which represents the effective properties of an equivalent elastic continuum. If it is chosen sufficiently high, the corresponding periodic cell is a representative volume element and its properties are close to the theoretical limit. Therefore, N does not need to be considered as a variable influencing the results, it just has to be chosen sufficiently high.

The ratio r^2/A is taken as constant, according to equation (3.1). Even if it was not, the dependence of the macroscopic properties on this ratio would be very simple. Young's modulus (or any other elastic stiffness) would be inversely proportional to r^2/A and the Poisson's ratio would not depend on it at all.

After all these considerations, we can rewrite the relationship between macro- and microscopic material parameters as

$$\frac{E}{\bar{E}} = \pi_E \left(\frac{\bar{G}}{\bar{E}}, l_r \right) \quad (3.7)$$

$$\nu = \pi_\nu \left(\frac{\bar{G}}{\bar{E}}, l_r \right) \quad (3.8)$$

The specific forms of equations (3.7) and (3.8) are addressed in following sections.

3.1 Theoretical analytical values

The presented derivation of analytical evaluation of elastic constants is a generalized version of [51].

Given a vector \mathbf{v} and a unit vector \mathbf{n} , \mathbf{v} can be split into the part parallel to \mathbf{n} and the part perpendicular to \mathbf{n} denoted by subscript N and T , respectively:

$$\begin{aligned} \mathbf{v} &= \mathbf{v}_N + \mathbf{v}_T \\ \mathbf{v}_N &= (\mathbf{v} \cdot \mathbf{n})\mathbf{n} = v_N \mathbf{n} \\ v_N &= \mathbf{v} \cdot \mathbf{n} \\ \mathbf{v}_T &= \mathbf{v} - \mathbf{v}_N = \mathbf{v} - (\mathbf{v} \cdot \mathbf{n})\mathbf{n} = \mathbf{v} - v_N \mathbf{n}. \end{aligned} \quad (3.9)$$

The stiffness tensor \mathbf{D}_e is derived bases on the stress tensor $\boldsymbol{\sigma}$ induced by the prescribed strain tensor $\boldsymbol{\varepsilon}$. Displacement of particles is assumed to be linear governed by strain tensor

$$\mathbf{u}_P = \mathbf{x}_P \cdot \boldsymbol{\varepsilon}. \quad (3.10)$$

Each link c is considered as a fictitious bar connecting particles J and K with branch vector \mathbf{l}^c , length L^c and unit direction (normal) vector \mathbf{n}^c related as

$$\mathbf{l}^c = \mathbf{x}_K - \mathbf{x}_J \quad L^c = \|\mathbf{l}^c\| = \sqrt{\mathbf{l}^c \cdot \mathbf{l}^c} \quad \mathbf{n}^c = \frac{\mathbf{l}^c}{\|\mathbf{l}^c\|} = \frac{\mathbf{l}^c}{L^c} \quad \mathbf{l}^c = L^c \mathbf{n}^c. \quad (3.11)$$

The change of the branch vector (relative displacement) is given by the displacement of particles as

$$\Delta \mathbf{l}^c = \mathbf{u}_K - \mathbf{u}_J = \mathbf{x}_K \cdot \boldsymbol{\varepsilon} - \mathbf{x}_J \cdot \boldsymbol{\varepsilon} = (\mathbf{x}_K - \mathbf{x}_J) \cdot \boldsymbol{\varepsilon} = \mathbf{l}^c \cdot \boldsymbol{\varepsilon}. \quad (3.12)$$

According to (3.9), the relative displacement can be split into normal and shear component:

$$\Delta \mathbf{l}^c = \Delta L_N^c \mathbf{n}^c + \Delta \mathbf{l}_T^c. \quad (3.13)$$

Applying relations (3.9) and (3.11) and kinematic constraints (3.12):

$$\Delta L_N^c = \Delta \mathbf{I}^c \cdot \mathbf{n}^c = \mathbf{I}^c \cdot \boldsymbol{\varepsilon} \cdot \mathbf{n}^c = L^c \mathbf{n}^c \cdot \boldsymbol{\varepsilon} \cdot \mathbf{n}^c = L^c (\mathbf{n}^c \otimes \mathbf{n}^c) : \boldsymbol{\varepsilon} = L^c \mathbf{N}^c : \boldsymbol{\varepsilon} \quad (3.14)$$

$$\begin{aligned} \Delta \mathbf{I}_T^c &= \Delta \mathbf{I}^c - \mathbf{n}^c \Delta L_N^c = \mathbf{I}^c \cdot \boldsymbol{\varepsilon} - \mathbf{n}^c (L^c \mathbf{n}^c \otimes \mathbf{n}^c : \boldsymbol{\varepsilon}) = L^c \mathbf{n}^c \cdot \boldsymbol{\varepsilon} - L^c (\mathbf{n}^c \otimes \mathbf{n}^c \otimes \mathbf{n}^c) : \boldsymbol{\varepsilon} = \\ &= L^c \mathbf{n}^c \cdot \mathbf{I}^S : \boldsymbol{\varepsilon} - L^c \mathcal{N}^c : \boldsymbol{\varepsilon} = L^c \mathcal{T} : \boldsymbol{\varepsilon} \end{aligned} \quad (3.15)$$

where

$$\mathbf{N} = \mathbf{n} \otimes \mathbf{n} \quad (3.16)$$

$$\mathcal{N} = \mathbf{n} \otimes \mathbf{n} \otimes \mathbf{n} = \mathbf{N} \otimes \mathbf{n} = \mathbf{n} \otimes \mathbf{N} \quad (3.17)$$

$$\mathbf{N} = \mathbf{n} \otimes \mathbf{n} \otimes \mathbf{n} \otimes \mathbf{n} = \mathbf{N} \otimes \mathbf{N} \quad (3.18)$$

$$\mathcal{T} = \mathbf{n} \cdot \mathbf{I}^S - \mathbf{n} \otimes \mathbf{n} \otimes \mathbf{n} = \mathbf{n} \cdot \mathbf{I}^S - \mathcal{N} \quad (3.19)$$

$$\mathcal{T}^T = \mathbf{I}^S \cdot \mathbf{n} - \mathcal{N} \quad (3.20)$$

$$\begin{aligned} \mathbf{T} &= \mathcal{T}^T \cdot \mathcal{T} = (\mathbf{I}^S \cdot \mathbf{n} - \mathcal{N}) \cdot (\mathbf{n} \cdot \mathbf{I}^S - \mathcal{N}) = \\ &= (\mathbf{I}^S \cdot \mathbf{n}) \cdot (\mathbf{n} \cdot \mathbf{I}^S) - (\mathbf{I}^S \cdot \mathbf{n}) \cdot \mathcal{N} - \mathcal{N} \cdot (\mathbf{n} \cdot \mathbf{I}^S) + \mathcal{N} \cdot \mathcal{N} = \\ &= (\mathbf{I}^S \cdot \mathbf{n}) \cdot (\mathbf{n} \cdot \mathbf{I}^S) - \mathbf{N} - \mathbf{N} + \mathbf{N} = (\mathbf{I}^S \cdot \mathbf{n}) \cdot (\mathbf{n} \cdot \mathbf{I}^S) - \mathbf{N} \end{aligned} \quad (3.21)$$

are projection and auxiliary tensors.

Constitutive law assumes independent normal and shear direction and thus resulting normal and shear forces are parallel to normal and shear relative displacements:

$$\mathbf{f}^c = \mathbf{n}^c f_N^c + \mathbf{f}_T^c \quad (3.22)$$

$$f_N^c = \bar{k}_N^c \Delta L_N^c = \frac{\bar{E}A^c}{L^c} \Delta L_N^c \quad (3.23)$$

$$\mathbf{f}_T^c = \bar{k}_T^c \Delta \mathbf{I}_T^c = \frac{\bar{G}A^c}{L^c} \Delta \mathbf{I}_T^c. \quad (3.24)$$

Substituting kinematic assumptions (3.14) and (3.15) yields

$$f_N^c = \frac{\bar{E}A^c}{L^c} \Delta L_N^c = \bar{E}A^c \mathbf{N}^c : \boldsymbol{\varepsilon} \quad (3.25)$$

$$\mathbf{f}_T^c = \frac{\bar{G}A^c}{L^c} \Delta \mathbf{I}_T^c = \bar{G}A^c \mathcal{T}^c : \boldsymbol{\varepsilon}. \quad (3.26)$$

Stress tensor is defined according to equation (4.56). Because both the strain tensor $\boldsymbol{\varepsilon}$ and the desired elastic stiffness tensor \mathbf{D}_e is symmetric, we consider only the symmetric part of the stress tensor in the derivation.

$$\begin{aligned} \boldsymbol{\sigma} &= \frac{1}{V} \sum_c (\mathbf{I}^c \otimes \mathbf{f}^c)^S = \frac{1}{V} \sum_c (L^c \mathbf{n}^c \otimes (\mathbf{n}^c f_N^c + \mathbf{f}_T^c))^S = \frac{1}{V} \sum_c L^c (\mathbf{n}^c \otimes \mathbf{n}^c f_N^c + \mathbf{n}^c \otimes \mathbf{f}_T^c)^S = \\ &= \frac{1}{V} \sum_c L^c (\mathbf{N}^c f_N^c + (\mathbf{n}^c \otimes \mathbf{f}_T^c)^S) \end{aligned} \quad (3.27)$$

The last term can be rewritten as

$$\begin{aligned} (\mathbf{n} \otimes \mathbf{f}_T)^S &= (\mathbf{f}_T \otimes \mathbf{n})^S = \mathbf{I}^S : (\mathbf{f}_T \otimes \mathbf{n}) = (\mathbf{I}^S \cdot \mathbf{n}) \cdot \mathbf{f}_T - \mathcal{N} \cdot \mathbf{f}_T = \\ &= (\mathbf{I}^S \cdot \mathbf{n} - \mathcal{N}) \cdot \mathbf{f}_T = \mathcal{T}^T \cdot \mathbf{f}_T. \end{aligned} \quad (3.28)$$

The term $\mathcal{N} \cdot \mathbf{f}_T$ is zero (normal vector \mathbf{n} is perpendicular to the shear force \mathbf{f}_T) and is added to get consistent formalism.

Substituting constitutive assumptions (3.26) yields

$$\begin{aligned} \boldsymbol{\sigma} &= \frac{1}{V} \sum_c L^c \left(\mathbf{N}^c f_N^c + \mathcal{T}^{cT} \cdot \mathbf{f}_T^c \right) = \\ &= \frac{1}{V} \sum_c L^c \left(\mathbf{N}^c (\bar{E} A^c \mathbf{N}^c : \boldsymbol{\varepsilon}) + \mathcal{T}^{cT} \cdot (\bar{G} A^c \mathcal{T}^c : \boldsymbol{\varepsilon}) \right) = \\ &= \frac{1}{V} \sum_c L^c A^c \left(\bar{E} (\mathbf{N}^c \otimes \mathbf{N}^c) : \boldsymbol{\varepsilon} + \bar{G} (\mathcal{T}^{cT} \cdot \mathcal{T}^c) : \boldsymbol{\varepsilon} \right) = \\ &= \frac{1}{V} \sum_c L^c A^c (\bar{E} \mathbf{N}^c + \bar{G} \mathbf{T}^c) : \boldsymbol{\varepsilon}. \end{aligned} \quad (3.29)$$

Comparison to the elastic stress-strain law (A.119)

$$\boldsymbol{\sigma} = \mathbf{D}_e : \boldsymbol{\varepsilon} \quad (3.30)$$

yields the expression of stiffness tensor

$$\mathbf{D}_e = \frac{1}{V} \sum_c L^c A^c (\bar{E} \mathbf{N}^c + \bar{G} \mathbf{T}^c). \quad (3.31)$$

According to [51], sum of terms dependent on direction \mathbf{n}^c can be approximated with an integral over solid angle

$$\sum_c^{N_c} f(\mathbf{n}^c) = \frac{N_c}{4\pi} \int_{\Omega} f(\mathbf{n}) d\Omega. \quad (3.32)$$

The integration domain here is the surface of the unit sphere and N_c is number of contacts.

Using identities (A.127) and (A.128)

$$\int_{\Omega} \mathbf{N} d\Omega = \int_{\Omega} \mathbf{n} \otimes \mathbf{n} \otimes \mathbf{n} \otimes \mathbf{n} d\Omega = \frac{4\pi}{15} (3\mathbf{I}^V + 2\mathbf{I}^S) \quad (3.33)$$

$$\begin{aligned} \int_{\Omega} \mathbf{T} d\Omega &= \int_{\Omega} (\mathbf{I}^S \cdot \mathbf{n}) \cdot (\mathbf{n} \cdot \mathbf{I}^S) - \mathbf{N} d\Omega = \int_{\Omega} (\mathbf{I}^S \cdot \mathbf{n}) \cdot (\mathbf{n} \cdot \mathbf{I}^S) d\Omega - \int_{\Omega} \mathbf{N} d\Omega = \\ &= \frac{4\pi}{3} \mathbf{I}^S - \frac{4\pi}{15} (3\mathbf{I}^V + 2\mathbf{I}^S) = \frac{4\pi}{5} (\mathbf{I}^S - \mathbf{I}^V), \end{aligned} \quad (3.34)$$

applying approximation (3.32) and assuming the uniform distribution of branch lengths and cross section areas gives

$$\begin{aligned} \sum_c L^c A^c f(\mathbf{n}^c) &\approx \sum_c \frac{\sum_c L^c A^c}{N_c} f(\mathbf{n}^c) = \frac{\sum_c L^c A^c}{N_c} \sum_c f(\mathbf{n}^c) \approx \\ &\approx \frac{\sum_c L^c A^c}{N_c} \cdot \frac{N_c}{4\pi} \int_{\Omega} f(\mathbf{n}) = \frac{\sum_c L^c A^c}{4\pi} \int_{\Omega} f(\mathbf{n}) \end{aligned} \quad (3.35)$$

yields

$$\begin{aligned} \mathbf{D}_e &= \frac{1}{V} \sum_c L^c A^c (\bar{\mathbf{E}}\mathbf{N}^c + \bar{\mathbf{G}}\mathbf{T}^c) \approx \frac{N_c}{4\pi V} \int_{\Omega} L^c A^c (\bar{\mathbf{E}}\mathbf{N} + \bar{\mathbf{G}}\mathbf{T}) d\Omega \approx \\ &\approx \frac{\sum L^c A^c}{4\pi V} \int_{\Omega} \bar{\mathbf{E}}\mathbf{N} + \bar{\mathbf{G}}\mathbf{T} d\Omega = \frac{\sum LA}{4\pi V} \left(\bar{\mathbf{E}} \frac{4\pi}{15} (3\mathbf{I}^V + 2\mathbf{I}^S) \bar{\mathbf{G}} \frac{4\pi}{5} (\mathbf{I}^S - \mathbf{I}^V) \right) = \\ &= \frac{\sum L^c A^c}{5V} (\bar{\mathbf{E}} - \bar{\mathbf{G}}) \mathbf{I}^V + \frac{\sum L^c A^c}{15V} (2\bar{\mathbf{E}} + 3\bar{\mathbf{G}}) \mathbf{I}^S. \end{aligned} \quad (3.36)$$

Comparing with the Hooke's law (A.123)

$$\mathbf{D}_e = \frac{3E\nu}{(1+\nu)(1-2\nu)} \mathbf{I}^V + \frac{E}{1+\nu} \mathbf{I}^S \quad (3.37)$$

yields the approximation of macroscopic elastic constants

$$E = \frac{\sum L^c A^c}{3V} \cdot \frac{\bar{\mathbf{E}} (2\bar{\mathbf{E}} + 3\bar{\mathbf{G}})}{4\bar{\mathbf{E}} + \bar{\mathbf{G}}} \quad \nu = \frac{\bar{\mathbf{E}} - \bar{\mathbf{G}}}{4\bar{\mathbf{E}} + \bar{\mathbf{G}}}. \quad (3.38)$$

See also codes/scripts/tests/macroelastic.py.

3.2 Static FEM solution

The links fictitiously connect centers of particles and can be represented by bars with length L and cross section area A . In the FEM solution described below, particles are modeled as nodes with six degrees of freedom, three displacements and three rotations

$$\mathbf{u} = \{u_1, u_2, u_3\}^T \quad \boldsymbol{\phi} = \{\phi_1, \phi_2, \phi_3\}^T \quad (3.39)$$

respectively. Links are modeled as beam-like finite elements.

Each particle (node) P has center \mathbf{p}_P and a nodal displacement vector

$$\mathbf{d}_P = \begin{Bmatrix} \mathbf{u} \\ \boldsymbol{\phi} \end{Bmatrix} = \{u_1, u_2, u_3, \phi_1, \phi_2, \phi_3\}^T. \quad (3.40)$$

A nodal displacement vector of a link (finite element) is constructed by merging the displacement vectors of connected particles J and K

$$\mathbf{d} = \begin{Bmatrix} \mathbf{d}_J \\ \mathbf{d}_K \end{Bmatrix} = \{u_{J1}, u_{J2}, u_{J3}, \phi_{J1}, \phi_{J2}, \phi_{J3}, u_{K1}, u_{K2}, u_{K3}, \phi_{K1}, \phi_{K2}, \phi_{K3}\}^T. \quad (3.41)$$

The values of \mathbf{d} uniquely defines the contact displacement, i.e, the fictitious mutual displacement at the center of the link, expressed in the local coordinate system of the link

$$\mathbf{u}_c = \begin{Bmatrix} u_N \\ \mathbf{u}_T \end{Bmatrix} = \begin{Bmatrix} u_N \\ u_{T1} \\ u_{T2} \end{Bmatrix} \quad (3.42)$$

and the equivalent strain of the link

$$\boldsymbol{\varepsilon} = \frac{1}{L} \mathbf{u}_c. \quad (3.43)$$

The local coordinate system $\mathbf{e}_N, \mathbf{e}_{T1}, \mathbf{e}_{T2}$ is defined such that the first base vector

$$\mathbf{e}_N = \frac{\mathbf{p}_K - \mathbf{p}_J}{\|\mathbf{p}_K - \mathbf{p}_J\|}, \quad (3.44)$$

is a normalized vector given by the centers of connected particles, \mathbf{e}_{T1} is chosen arbitrarily but must be perpendicular to \mathbf{e}_N and finally the last base vector is defined by the cross product

$$\mathbf{e}_{T2} = \mathbf{e}_N \times \mathbf{e}_{T1}. \quad (3.45)$$

Its matrix representation is an orthogonal matrix with rows equal to local base vectors

$$\mathbf{R} = \begin{bmatrix} \mathbf{e}_N^T \\ \mathbf{e}_{T1}^T \\ \mathbf{e}_{T2}^T \end{bmatrix}, \quad \mathbf{R}^T = \mathbf{R}^{-1} \quad (3.46)$$

and can be used to transform a vector from the global to the local coordinate system and vice versa:

$$\mathbf{R}\mathbf{u} = \mathbf{u}_l, \quad \mathbf{R}\boldsymbol{\phi} = \boldsymbol{\phi}_l, \quad \mathbf{R}^T\mathbf{u}_l = \mathbf{u}, \quad \mathbf{R}^T\boldsymbol{\phi}_l = \boldsymbol{\phi} \quad (3.47)$$

The transformation matrix \mathbf{T} transforms nodal displacement vector \mathbf{d} from the global coordinate system:

$$\mathbf{T}\mathbf{d} = \mathbf{d}_l, \quad \mathbf{T}^T\mathbf{d}_l = \mathbf{d} \quad (3.48)$$

Because of the structure of \mathbf{d} (3.41) and using (3.47) it has the form

$$\mathbf{T} = \begin{bmatrix} \mathbf{R} & \cdot & \cdot & \cdot \\ \cdot & \mathbf{R} & \cdot & \cdot \\ \cdot & \cdot & \mathbf{R} & \cdot \\ \cdot & \cdot & \cdot & \mathbf{R} \end{bmatrix}. \quad (3.49)$$

The relation between nodal displacements and equivalent strains can be rewritten in the matrix form as

$$\boldsymbol{\varepsilon} = \mathbf{B}\mathbf{d} = \mathbf{B}_l\mathbf{d}_l, \quad (3.50)$$

where

$$\mathbf{B}_l = \frac{1}{L} \begin{bmatrix} -1 & \cdot & \cdot & \cdot & \cdot & \cdot & 1 & \cdot & \cdot & \cdot & \cdot \\ \cdot & -1 & \cdot & \cdot & \cdot & -\frac{L}{2} & \cdot & 1 & \cdot & \cdot & -\frac{L}{2} \\ \cdot & \cdot & -1 & \cdot & \frac{L}{2} & \cdot & \cdot & \cdot & 1 & \cdot & \frac{L}{2} \\ \cdot & \cdot \end{bmatrix} \quad (3.51)$$

is a strain-displacement (or geometric) matrix of the element with respect to the local coordinate system. Using (3.50) and (3.48), the global geometric matrix \mathbf{B} is defined as

$$\boldsymbol{\varepsilon} = \mathbf{B}\mathbf{d} = \mathbf{B}_l\mathbf{d}_l = \mathbf{B}_l\mathbf{T}\mathbf{T}^T\mathbf{d}_l = \mathbf{B}_l\mathbf{T}\mathbf{d} \quad \rightarrow \quad \mathbf{B} = \mathbf{B}_l\mathbf{T}. \quad (3.52)$$

Link stress vector

$$\boldsymbol{\sigma} = \begin{Bmatrix} \sigma_N \\ \boldsymbol{\sigma}_T \end{Bmatrix} = \begin{Bmatrix} \sigma_N \\ \sigma_{T1} \\ \sigma_{T2} \end{Bmatrix} = \begin{Bmatrix} \bar{E}\varepsilon_N \\ \bar{G}\varepsilon_{T1} \\ \bar{G}\varepsilon_{T2} \end{Bmatrix} \quad (3.53)$$

can be expressed in the matrix form

$$\boldsymbol{\sigma} = \mathbf{D}\boldsymbol{\varepsilon} \quad (3.54)$$

with

$$\mathbf{D} = \begin{bmatrix} \bar{E} & 0 & 0 \\ 0 & \bar{G} & 0 \\ 0 & 0 & \bar{G} \end{bmatrix} \quad (3.55)$$

being material stiffness matrix.

The link stiffness matrix is computed using the standard formula

$$\mathbf{K} = \int_V \mathbf{B}^T \mathbf{D} \mathbf{B} dV = \mathbf{A} \mathbf{L} \mathbf{B}^T \mathbf{D} \mathbf{B}. \quad (3.56)$$

Nodal forces can then be expressed as

$$\mathbf{f} = \mathbf{K} \mathbf{d} = \mathbf{A} \mathbf{L} \mathbf{B}^T \mathbf{D} \mathbf{B} \mathbf{d} = \mathbf{A} \mathbf{L} \mathbf{B}^T \boldsymbol{\sigma}. \quad (3.57)$$

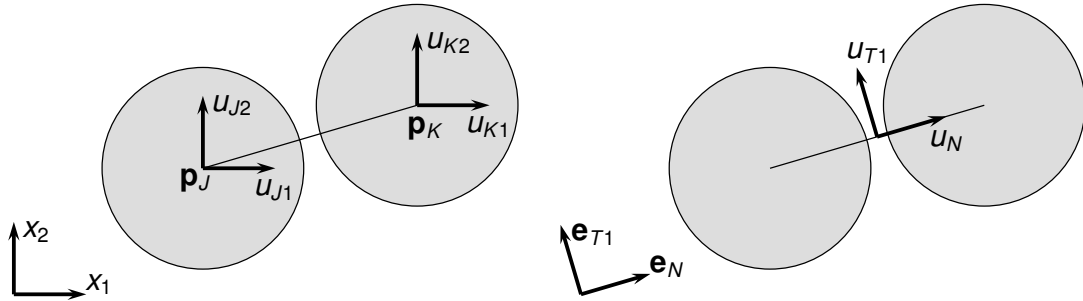


Figure 3.1: Illustration of the global (left) and local (right) coordinate system of the link

3.2.1 Periodic boundary conditions

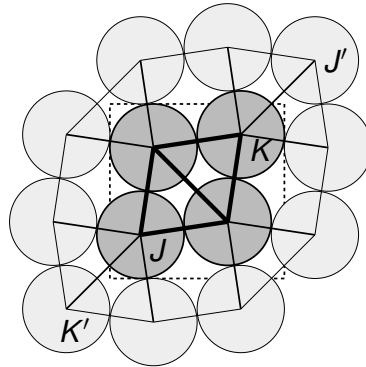


Figure 3.2: 2D example of periodic cell and "periodic" links

Numerical simulations have been done on a representative cell with periodic boundary conditions. The implementation of the periodic boundary conditions is analogous to the implementation described by [40]. Elements crossing the boundary of the bounding cube

(connecting one particle inside the cell with another particle physically located in one of the neighboring cells) is modified in a special way. Consider such an element connecting particles J and K and a corresponding element connecting periodic images of these particles, denoted as J and K' (see Figure 3.2). Both elements are real links of the structure, but for the analysis purposes only one of them is taken into account when setting up the equilibrium equations (in our example we chose link JK').

Consider a macroscopic deformation

$$\mathbf{E} = \{E_{11}, E_{22}, E_{33}, E_{23}, E_{31}, E_{12}\}^T. \quad (3.58)$$

Periodic boundary conditions are imposed by the set of constraint equations that contain the components of \mathbf{E} :

$$\begin{aligned} u_{K'1} &= u_{K1} + E_{11}k_1C + \frac{1}{2}E_{12}k_2C + \frac{1}{2}E_{31}k_3C \\ u_{K'2} &= u_{K2} + E_{22}k_2C + \frac{1}{2}E_{12}k_1C + \frac{1}{2}E_{23}k_3C \\ u_{K'3} &= u_{K3} + E_{33}k_3C + \frac{1}{2}E_{31}k_1C + \frac{1}{2}E_{23}k_2C \\ \phi_{K'1} &= \phi_{K1} \\ \phi_{K'2} &= \phi_{K2} \\ \phi_{K'3} &= \phi_{K3} \end{aligned} \quad (3.59)$$

C is the dimension of the cubic periodic cell, constants k have integer values (usually -1 , 0 or 1) and specify the position of the particle outside the cell according to the relations

$$\begin{aligned} x_{K'1} &= x_{K1} + k_1C \\ x_{K'2} &= x_{K2} + k_2C \\ x_{K'3} &= x_{K3} + k_3C. \end{aligned} \quad (3.60)$$

Using equations (3.59), the displacement of connected particles J and K' (periodic image of particle K) can be written in terms of the displacements of particles J and K and the macroscopic deformation as

$$\begin{Bmatrix} \mathbf{u}_J \\ \mathbf{u}_{K'} \end{Bmatrix} = \mathbf{P} \begin{Bmatrix} \mathbf{u}_J \\ \mathbf{u}_K \\ \mathbf{E} \end{Bmatrix} \quad (3.61)$$

The upper block (first 12×12 components out of 12×18) of the transformation matrix \mathbf{P} corresponds to the identity matrix, and the only non-zero components of the lower block are in rows 7-9 and in columns 13-18:

$$\mathbf{P}_{(7-9,13-18)} = C \begin{matrix} & \begin{matrix} 13 & 14 & 15 & 16 & 17 & 18 \end{matrix} \\ \begin{bmatrix} k_1 & 0 & 0 & 0 & \frac{1}{2}k_3 & \frac{1}{2}k_2 \\ 0 & k_2 & 0 & \frac{1}{2}k_3 & 0 & \frac{1}{2}k_1 \\ 0 & 0 & k_3 & \frac{1}{2}k_2 & \frac{1}{2}k_1 & 0 \end{bmatrix} & \begin{matrix} 7 \\ 8 \\ 9 \end{matrix} \end{matrix} \quad (3.62)$$

Using the transformation matrix \mathbf{P} , the modified stiffness matrix of the “periodic” elements (with 18 rows and 18 columns) can be expressed in the form

$$\mathbf{K} = \mathbf{A}\mathbf{L}\mathbf{P}^T\mathbf{B}^T\mathbf{D}\mathbf{B}\mathbf{P}. \quad (3.63)$$

The components of macroscopic deformation \mathbf{E} are therefore considered as global degrees of freedom. The corresponding “load” components are directly related to the macroscopic stress (they are equal to the stress components multiplied by the volume of the cell). To prevent displacement of the assembly as a rigid body, one particle needs to be “supported” by setting its three displacements to zero.

3.2.2 OOFEM implementation

The results presented in this thesis are computed with OOFEM, version 2.0.

Particles are implemented in `Particle` class, which is derived from `Node` class. Interactions are implemented in `CohesiveSurface3d` class, derived from `StructuralElement` class.

For the periodic solution, a link finite element has three nodes – two physical nodes and one node representing macroscopic deformation. The particle representing macroscopic deformation has (by convention) coordinates equal to dimensions of the periodic cell and has to be the third particle of the element. See the source codes for more information.

The implementation files of `CohesiveSurface3d` class were slightly refactored to correspond with the description in the section (especially the computation of strain-displacement matrix \mathbf{B}) and can be found in the file `codes/oofemyade/oofem-2.0/src/sm`.

3.2.3 Evaluation

To obtain the macroscopic elastic stiffness matrix of a particle assembly, the assembly is subjected to six simulations. In each simulation, one component of the macroscopic deformation \mathbf{E} is set to one while all the others are prescribed as zeros. The individual components of the macroscopic stress then represent the coefficients in the corresponding column of the macroscopic stiffness matrix \mathbf{D}_e .

3.3 Dynamic DEM solution

For the sake of completeness, the results obtained by DEM are also presented. Periodic boundary conditions according to section 2.3 are used. The macroscopic deformation is controlled by the deformation of the periodic cell. Numerical damping helps to remove kinetic energy from the system.

The evaluation is similar to the FEM case. The assembly is subjected to six simulations. In each simulation, one component of the macroscopic deformation is set to a “small” value ε while all the others are prescribed as zeros. The transformation matrix of the periodic cell is adjusted according to the desired macroscopic deformation and the model is relaxed to (almost) static equilibrium. The individual components of the macroscopic stress divided by the value of ε then represent the coefficients in the corresponding column of the macroscopic stiffness matrix \mathbf{D}_e .

3.4 Results

3.4.1 Isotropy of elastic constants

Firstly, macroscopic isotropy and stability of results for a variable number of particles N has been studied.

$$\mathbf{C}_e = \mathbf{D}_e^{-1} = \begin{bmatrix} \frac{1}{E_1} & -\frac{\nu_{21}}{E_2} & -\frac{\nu_{31}}{E_3} & \cdot & \cdot & \cdot \\ -\frac{\nu_{12}}{E_1} & \frac{1}{E_2} & -\frac{\nu_{32}}{E_3} & \cdot & \cdot & \cdot \\ -\frac{\nu_{13}}{E_1} & -\frac{\nu_{23}}{E_2} & \frac{1}{E_3} & \cdot & \cdot & \cdot \\ \cdot & \cdot & \cdot & \frac{1}{G_{23}} & \cdot & \cdot \\ \cdot & \cdot & \cdot & \cdot & \frac{1}{G_{31}} & \cdot \\ \cdot & \cdot & \cdot & \cdot & \cdot & \frac{1}{G_{12}} \end{bmatrix} \quad (3.64)$$

Several particle assemblies have been analyzed and the macroscopic constants E and ν have been evaluated for a number of values of the dimensionless quantities ν_r and \bar{k}_T/\bar{k}_N .

The resulting material is first considered as orthotropic, with compliance matrix \mathbf{C}_e (3.64), from which E_1 , E_2 , E_3 , ν_{12} , ν_{21} , ν_{13} , ν_{31} , ν_{23} , and ν_{32} are easily extracted. In the ideal case of an isotropic material, all Young's moduli and Poisson's ratios would be identical. To verify that the results indeed closely correspond to an isotropic behavior is one of the goals of this study.

The isotropy has been evaluated based on the following quantities:

- Relative anisotropy of Young's modulus E

$$\frac{\Delta E}{E} = \frac{\max_i |E_i - E_{\text{avg}}|}{E_{\text{avg}}} \quad (3.65)$$

E_i denotes i th computed modulus and E_{avg} their average value.

- Relative anisotropy of Poisson's ratio

$$\frac{\Delta \nu}{\nu} = \frac{\max_{ij} |\nu_{ij} - \nu_{\text{avg}}|}{\nu_{\text{avg}}} \quad (3.66)$$

- Relative anisotropy of shear modulus

$$\frac{\Delta G}{G} = \frac{\max_i \left| G_i - \frac{E_{\text{avg}}}{2(1+\nu_{\text{avg}})} \right|}{\frac{E_{\text{avg}}}{2(1+\nu_{\text{avg}})}} \quad (3.67)$$

- In the stiffness or compliance matrix of the isotropic material, there are a few zero elements. However, these elements are nonzero in the result of numerical simulations. The last studied quantity is therefore the relative deviation from zero of these elements

$$\frac{\Delta}{E} = \frac{\max_{ij} (|D_{ij}|)}{E_{\text{avg}}} \quad (3.68)$$

D_{ij} denotes elements, which are zero for isotropic material.

The findings can be summarized as:

- The mean material parameters E and ν are almost independent of the number of particles, even for N less than 100. For more than 200 particles per periodic cell, the values of mean material parameters do not change for any type of simulation (i.e., for any ratio \bar{k}_T/\bar{k}_N and any interaction ratio ι_r). See figure 3.3.
- The relative anisotropy of Young's modulus decreases with increasing number of particles. The convergence is faster for higher ι_r and for higher \bar{k}_T/\bar{k}_N . See figure 3.4.
- The relative anisotropy of Poisson's ratio ν has a similar trend: for an increasing number of particles, its relative anisotropy decreases. In contrast to the case of Young's modulus, the slowest convergence (or even no convergence at all) has been observed for ratio \bar{k}_T/\bar{k}_N close to 1. This is caused by the fact that for $\bar{k}_T/\bar{k}_N = 1$, the Poisson's ratio ν has a theoretical value 0 and the relative error is therefore higher. See figure 3.5.
- The theoretically vanishing components of the stiffness matrix of the macroscopic material are indeed almost zero, again for increasing N the error is smaller. Faster convergence has been observed on samples with higher ι_r and for \bar{k}_T/\bar{k}_N closer to 1. See figure 3.6.
- The relative error of the formula $G = \frac{E}{2(1+\nu)}$ gets smaller for increasing N . The convergence is faster for \bar{k}_T/\bar{k}_N closer to 1. See figure 3.7.
- All of the general trends described above are consistent with our expectations.

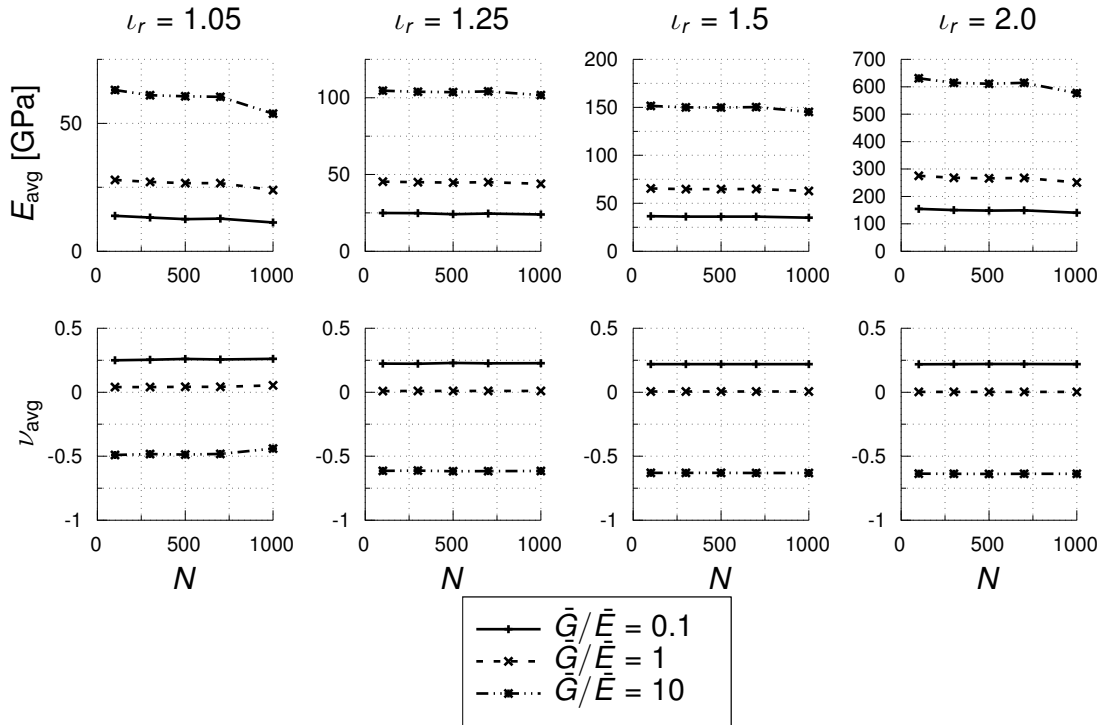


Figure 3.3: Stability of mean values of Young's modulus E and Poisson's ratio ν for various numbers of particles N

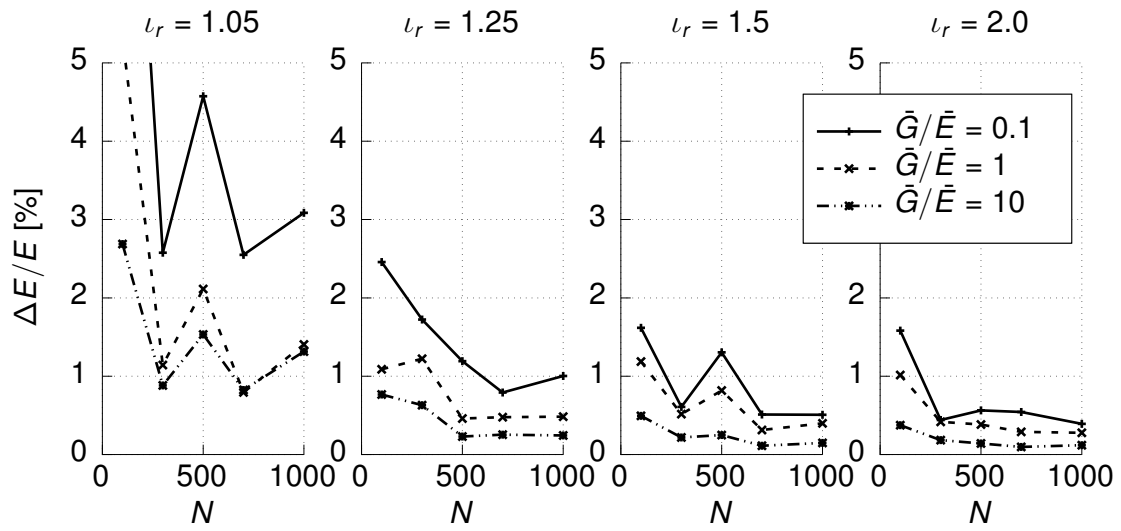


Figure 3.4: Relative anisotropy of Young's modulus $\Delta E/E$ for various N

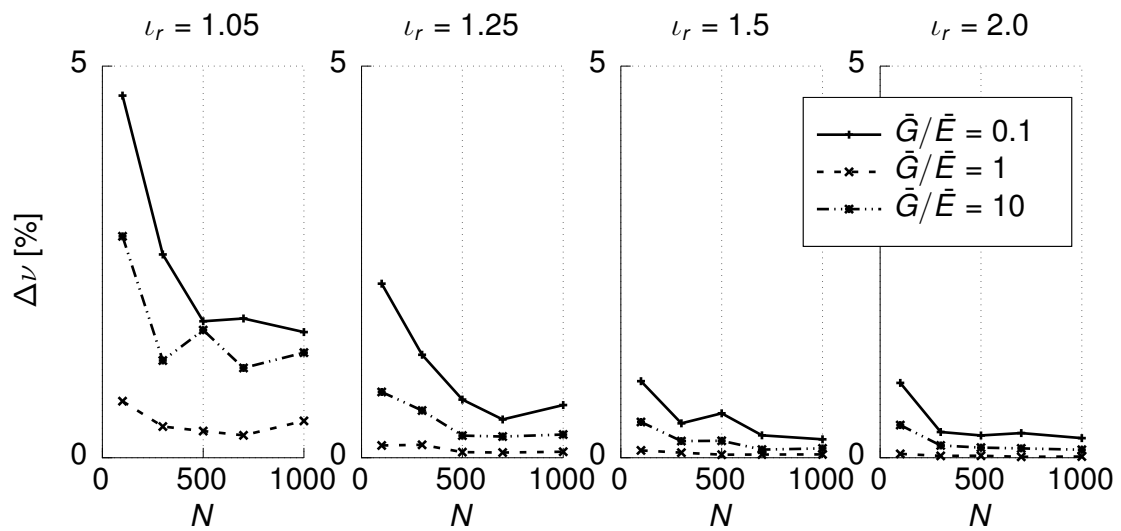
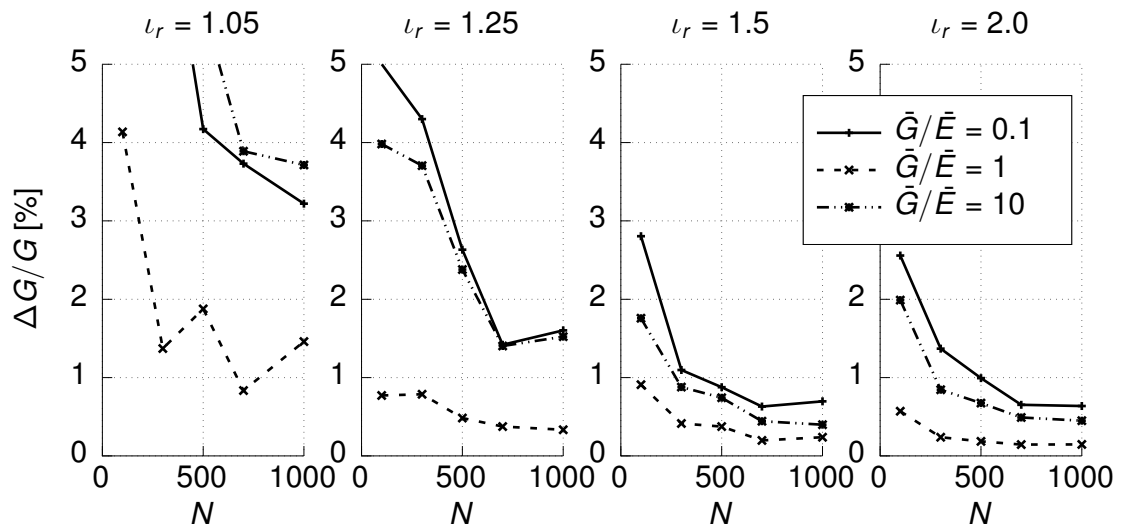
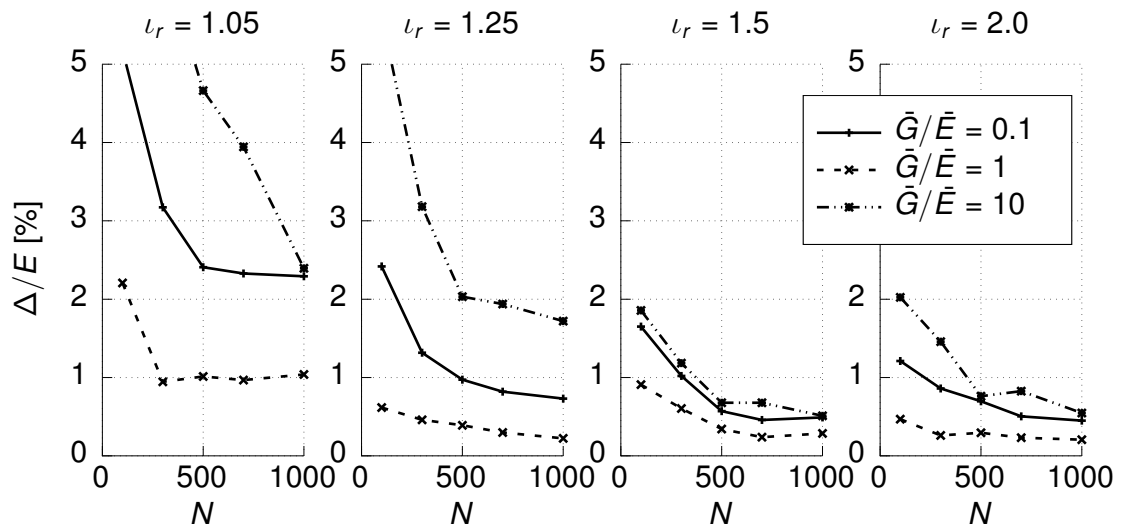


Figure 3.5: Relative anisotropy of Poisson's ratio $\Delta \nu/\nu$ for various N

Figure 3.6: Relative deviation from mean shear modulus $\Delta G/G$ for various N Figure 3.7: Relative deviation of "zero" elements of stiffness matrix Δ/E for various N

3.4.2 Comparison of analytical and numerical results

The mean values of Young's modulus and Poisson's ratio according to section 3.4.1 have been considered as the results of numerical tests to compare analytical and numerical results. The numerical relation between macro- and microscopic parameters has been computed for several values of ν_r and compared to the analytical values.

In graphs, points represent numerically obtained data and data according to equation (3.31). The line represents the analytical dependence according to equation (3.38).

The numerical results of static FEM, quasi-static DEM simulations and equation (3.31) are practically indistinguishable from each other. Certain discrepancy can be found for larger values of $\bar{G}/\bar{E} \rightarrow \infty$ because then Young's modulus tends to zero relatively to the shear modulus.

As seen from the graphs, the agreement between analytically and numerically obtained data is very good for higher values of ν_r . On the other hand, the analytical formula underestimates the actual (numerically determined) values of Poisson's ratio and overestimates the actual values of Young's modulus for $\nu_r < 1.3$. For all values of ν_r , the value of Poisson's ratio in the limit case for $\bar{G}/\bar{E} \rightarrow \infty$ ($\bar{E} = 0$) is -1 (the extreme theoretical value for Poisson's ratio), while the maximum attainable value is $\frac{1}{4}$ for higher values of ν_r , which corresponds to equation (3.38). A higher value of Poisson's ratio, up to 0.335, is obtained for $\nu_r = 1.05$.

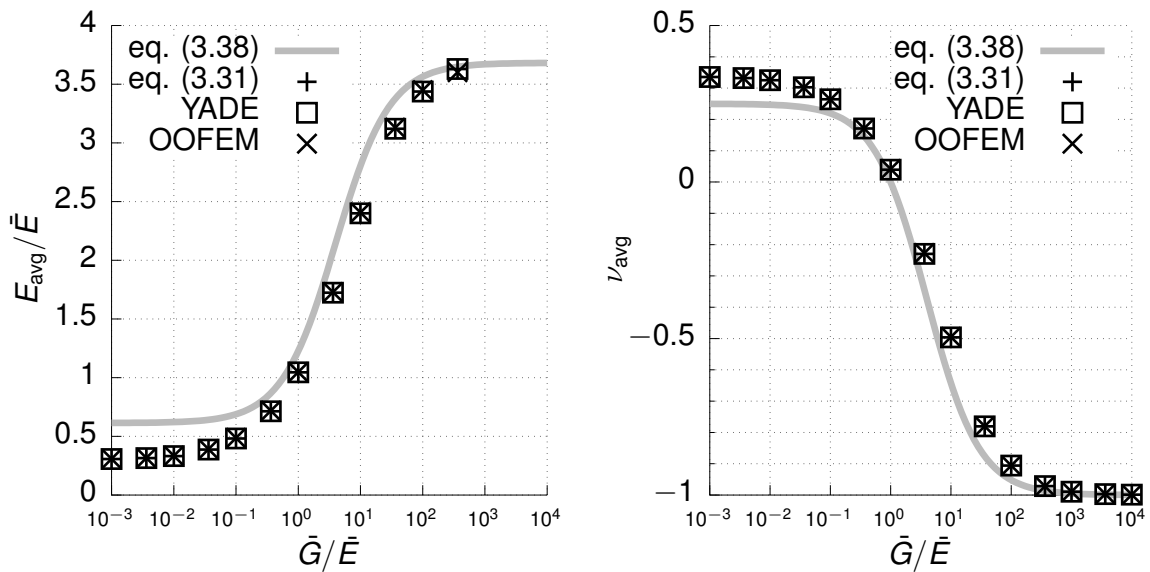


Figure 3.8: Relation between macro- and microscopic parameters for $\nu_r = 1.05$ (semilogarithmic plot)

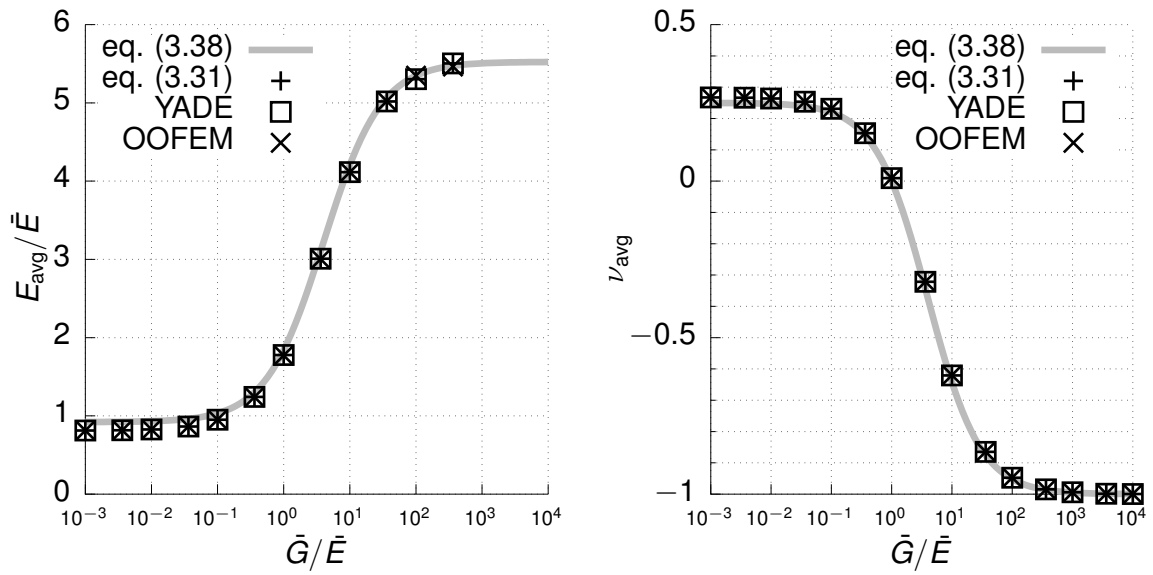


Figure 3.9: Relation between macro- and microscopic parameters for $\nu_r = 1.25$ (semilogarithmic plot)

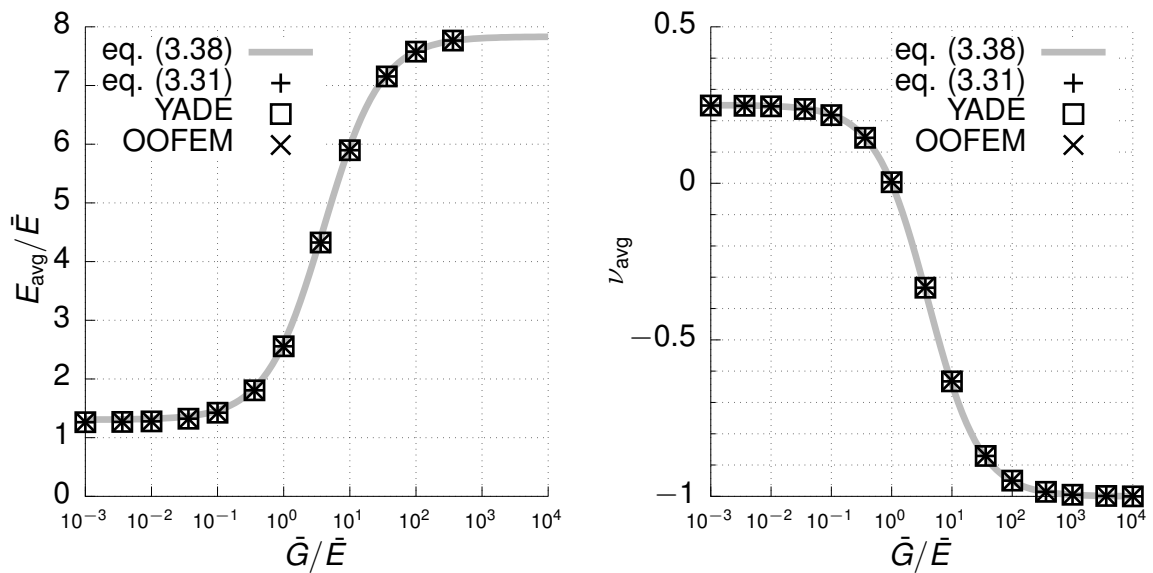


Figure 3.10: Relation between macro- and microscopic parameters for $\nu_r = 1.50$ (semilogarithmic plot)

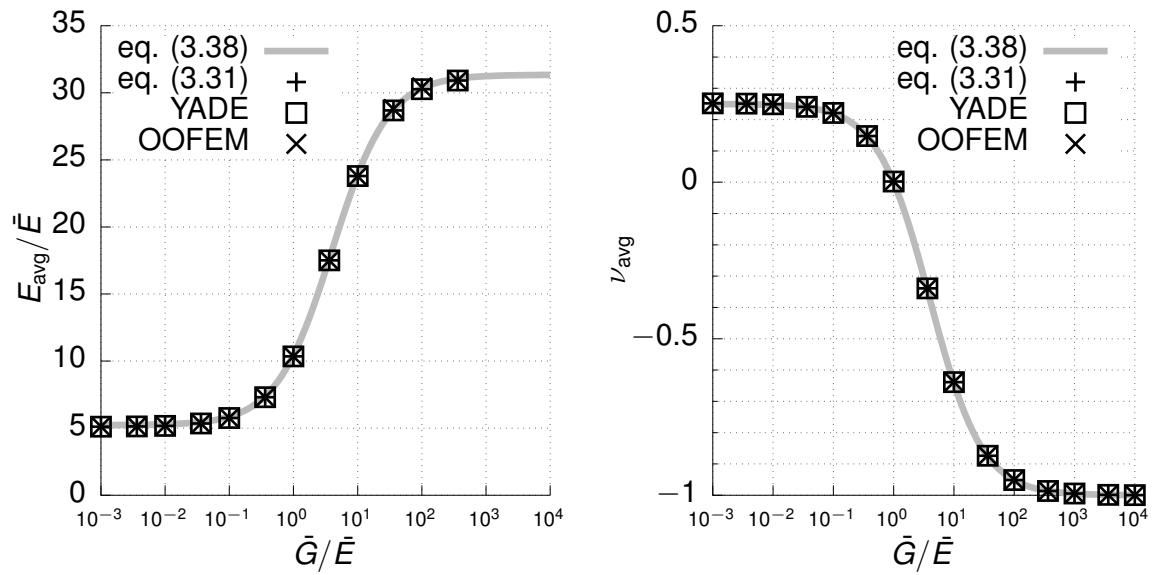


Figure 3.11: Relation between macro- and microscopic parameters for $\nu_r = 2.00$ (semilogarithmic plot)

4 Discrete stress tensor

Discrete nature is an essential feature of DEM. However, in some cases one would like to transform such discrete information (contact forces for instance) into its continuum counterpart (e.g., stress tensor). To give an example, assume a sample of sand, which is on lower level definitely discrete domain, thus discrete forces may be used as a model for description of mutual interaction between individual grains. On the other hand, on a higher scale (e.g., building construction), investigation of each individual sand grain would not be meaningful (or even possible) and the same material is considered as a continuum.

The evaluation of equivalent stress from discrete forces is a topic much older than DEM itself [58] described in many papers [4, 17, 8], but until these days it is a subject of debates in specialized literature [11, 7, 52, 9, 10]. A brief summary of current knowledge and author's new ideas are presented in this chapter.

The discrete elements in DEM possess 6 degrees of freedom, namely 3 displacements and 3 rotations. Classical Boltzmann continuum assumes 3 degrees of freedom (3 displacements) in each material point. Therefore a higher order (Cosserat for instance) model should be used for continuum approximation of DEM in its general form [4]. Readers not familiar with Cosserat continuum are referred to section A.3.

Consider a system of rigid particles P represented as mass points \mathbf{x}_P . The particles mutually interact with each other by fictitious links c with resulting contact (internal) forces and couples acting at contact points \mathbf{c} . We consider external body forces \mathbf{f} , body couples \mathbf{c} , surface forces \mathbf{t} and surface couples \mathbf{m} as Dirac delta distributions transforming boundary and volume integrals into discrete sums over points of application e in terms of external forces \mathbf{f}^e and external couples \mathbf{c}^e :

$$\int_V \mathbf{f} \cdot \delta \mathbf{u} dV + \int_S \mathbf{t} \cdot \delta \mathbf{u} dS = \sum_e \mathbf{f}^e \cdot \delta \mathbf{u} \quad (4.1)$$

$$\int_V \mathbf{x} \otimes \mathbf{f} dV + \int_S \mathbf{x} \otimes \mathbf{t} dS = \sum_e \mathbf{x} \otimes \mathbf{f}^e \quad (4.2)$$

$$\int_V \mathbf{c} \cdot \delta \mathbf{u} dV + \int_S \mathbf{m} \cdot \delta \mathbf{u} dS = \sum_e \mathbf{c}^e \cdot \delta \mathbf{u} \quad (4.3)$$

$$\int_V \mathbf{x} \otimes \mathbf{c} dV + \int_S \mathbf{x} \otimes \mathbf{m} dS = \sum_e \mathbf{x} \otimes \mathbf{c}^e. \quad (4.4)$$

4.1 Derivation based on virtual work

The principle of virtual displacements in Cosserat continuum (see section A.3.3)

$$\int_V \boldsymbol{\sigma} : (\nabla \otimes \delta \mathbf{u}) dV = \int_V \mathbf{f} \cdot \delta \mathbf{u} dV + \int_S \mathbf{t} \cdot \delta \mathbf{u} dS \quad (4.5)$$

$$\int_V \boldsymbol{\mu} : (\nabla \otimes \delta \boldsymbol{\phi}) dV - \int_V \boldsymbol{\sigma} : (\mathbf{1} \times \delta \boldsymbol{\phi}) dV = \int_V \mathbf{c} \cdot \delta \boldsymbol{\phi} dV + \int_S \mathbf{m} \cdot \delta \boldsymbol{\phi} dS. \quad (4.6)$$

is expressed in terms of the stress tensor $\boldsymbol{\sigma}$, couple stress tensor $\boldsymbol{\mu}$, and external load fields. The virtual fields are displacement $\delta \mathbf{u}$ and its gradient $\delta \mathbf{U} = \nabla \otimes \delta \mathbf{u}$ and rotation $\delta \boldsymbol{\phi}$ and its gradient (curvature tensor) $\delta \boldsymbol{\kappa} = \nabla \otimes \delta \boldsymbol{\phi}$.

The equivalent (couple) stress tensor is derived under the assumption that virtual work of discrete forces is equal to the virtual work of an equivalent continuum. We assume the *macro* (couple) stress to be *one constant value*, which is expressed by overlined symbols, e.g., $\bar{\sigma}$. The virtual fields are considered to be (at most) linear functions and therefore their gradients are constant (or zero).

The derivation is presented for both external and internal discrete forces. For example, in the case of one rigid particle, no internal forces are present and only the derivation based on virtual work of discrete *external* forces is meaningful. On the other hand, no external forces are present in the equilibrium case of a periodic cell and only the derivation based on virtual work of discrete *internal* forces is meaningful.

The internal forces of one particle may not be in equilibrium, but are required to be in equilibrium with (possibly zero) external load acting at the particle's reference point. This corresponds to static nonequilibrium case and the balancing load corresponds to inertial forces. The external loads are required to satisfy force and moment equilibrium conditions

$$\sum \mathbf{f} = \mathbf{0} \qquad \sum \mathbf{c} + \sum \mathbf{x} \times \mathbf{f} = \mathbf{0}. \quad (4.7)$$

4.1.1 Virtual work of discrete external forces

Consider an external force \mathbf{f}^e and couple \mathbf{c}^e acting at point \mathbf{x}^e . Together with virtual displacement $\delta \mathbf{u}^e$ and rotation $\delta \phi^e$, the virtual work of these quantities is simply

$$\delta W^e = \mathbf{f}^e \cdot \delta \mathbf{u}^e + \mathbf{c}^e \cdot \delta \phi^e. \quad (4.8)$$

The total virtual work of external forces is the sum of contributions of individual discrete points e :

$$\delta W = \sum_e \delta W^e = \sum_e \mathbf{f}^e \cdot \delta \mathbf{u}^e + \sum_e \mathbf{c}^e \cdot \delta \phi^e. \quad (4.9)$$

4.1.1.1 Virtual displacement

We start from the part of continuum virtual work principle which depends on virtual displacement (A.104)

$$\int_V \boldsymbol{\sigma} : \delta \mathbf{U} dV = \int_V \mathbf{f} \cdot \delta \mathbf{u} dV + \int_S \mathbf{t} \cdot \delta \mathbf{u} dS. \quad (4.10)$$

The right hand side is the virtual work of external forces. The external forces are considered as Dirac delta distributions (4.4), which coincide with the virtual work of discrete external forces (4.9):

$$\int_V \mathbf{f} \cdot \delta \mathbf{u} dV + \int_S \mathbf{t} \cdot \delta \mathbf{u} dS = \sum_e \mathbf{f}^e \cdot \delta \mathbf{u}^e. \quad (4.11)$$

According to the assumption of *constant* macro quantities, the left hand side can be rewritten to the form

$$\int_V \boldsymbol{\sigma} : \delta \mathbf{U} dV = \delta \mathbf{U} : V \bar{\boldsymbol{\sigma}}. \quad (4.12)$$

Virtual work equation (4.10) can then be rewritten as

$$\delta \mathbf{U} : V \bar{\boldsymbol{\sigma}} = \sum_e \mathbf{f}^e \cdot \delta \mathbf{u}^e. \quad (4.13)$$

Assuming constant $\delta \mathbf{u}$ ($\delta \mathbf{U} = \mathbf{0}$) yields

$$\mathbf{0} = \sum_e \mathbf{f}^e \cdot \delta \mathbf{u}^e \quad (4.14)$$

$$\xrightarrow{\forall \delta \mathbf{u} = \text{const}}$$

$$\sum_e \mathbf{f}^e = \mathbf{0} \quad (4.15)$$

the external force equilibrium condition.

Assuming homogeneous $\delta \mathbf{U}$

$$\delta \mathbf{u} = \mathbf{x} \cdot \delta \mathbf{U} \quad (4.16)$$

yields the expression for discrete stress tensor

$$\delta \mathbf{U} : V \bar{\boldsymbol{\sigma}} = \sum_e \mathbf{x}^e \cdot \delta \mathbf{U} \cdot \mathbf{f}^e = \sum_e \delta \mathbf{U} : (\mathbf{x}^e \otimes \mathbf{f}^e) \quad (4.17)$$

$$\xrightarrow{\forall \delta \mathbf{U}}$$

$$V \bar{\boldsymbol{\sigma}} = \sum_e \mathbf{x}^e \otimes \mathbf{f}^e. \quad (4.18)$$

In general, the stress tensor may be non-symmetric, as illustrated in section 4.3.

4.1.1.2 Virtual rotation

We start from the part of continuum virtual work principle which depends on virtual rotation (A.105)

$$\int_V \boldsymbol{\mu} : \delta \boldsymbol{\kappa} dV = \int_V \boldsymbol{\sigma} : (\mathbf{1} \times \delta \boldsymbol{\phi}) dV + \int_V \mathbf{c} \cdot \delta \boldsymbol{\phi} dV + \int_S \mathbf{m} \cdot \delta \boldsymbol{\phi} dS. \quad (4.19)$$

One part of the right hand side is the virtual work of external couples. The external couples are considered as Dirac delta distributions (4.4), which coincide with the virtual work of discrete couples (4.9)

$$\int_V \mathbf{c} \cdot \delta \boldsymbol{\phi} dV + \int_S \mathbf{m} \cdot \delta \boldsymbol{\phi} dS = \sum_e \mathbf{c}^e \cdot \delta \boldsymbol{\phi}^e. \quad (4.20)$$

According to the assumption of *constant* macro quantities, the left hand side of (4.19) can be rewritten to the form

$$\int_V \boldsymbol{\mu} : \delta \boldsymbol{\kappa} dV = \delta \boldsymbol{\kappa} : V \bar{\boldsymbol{\mu}}. \quad (4.21)$$

Using equation (A.55) and again assuming *constant* macro quantities yields

$$\int_V \boldsymbol{\sigma} : (\mathbf{1} \times \delta \boldsymbol{\phi}) dV = \int_V (\mathbf{1} \times \boldsymbol{\sigma}) \cdot \delta \boldsymbol{\phi} dV = (\mathbf{1} \times \bar{\boldsymbol{\sigma}}) \cdot \int_V \delta \boldsymbol{\phi} dV. \quad (4.22)$$

Virtual work equation (4.19) can then be rewritten to the form

$$\delta \boldsymbol{\kappa} : V \bar{\boldsymbol{\mu}} - (\mathbf{1} \times \bar{\boldsymbol{\sigma}}) \cdot \int_V \delta \boldsymbol{\phi} dV = \sum_e \mathbf{c}^e \cdot \delta \boldsymbol{\phi}^e. \quad (4.23)$$

Assuming constant $\delta\phi$ ($\delta\kappa = \mathbf{0}$) yields

$$-(\mathbf{1} \times \bar{\sigma}) \cdot \int_V \delta\phi \, dV = \sum_e \mathbf{c}^e \cdot \delta\phi^e \quad (4.24)$$

$$\xrightarrow{\forall \delta\phi = \text{const}} \\ -\mathbf{1} \times V\bar{\sigma} = \sum_e \mathbf{c}^e \quad (4.25)$$

antisymmetric part of stress tensor. Equation (4.25) can also be derived from (4.18) using identity (A.56)

$$\sum_e \mathbf{c}^e = -\mathbf{1} \times V\bar{\sigma} = \mathbf{1} \times \sum_e \mathbf{x}^e \otimes \mathbf{f}^e = \sum_e \mathbf{x}^e \times \mathbf{f}^e \quad (4.26)$$

because we assume the forces and couples to be equilibrated according to equation (4.7).

Assuming homogeneous $\delta\kappa$

$$\delta\phi = \mathbf{x} \cdot \delta\kappa \quad (4.27)$$

yields

$$\begin{aligned} (\mathbf{1} \times \bar{\sigma}) \cdot \int_V \delta\phi \, dV &= \int_V \mathbf{x} \cdot \delta\kappa \, dV \cdot (\mathbf{1} \times \bar{\sigma}) = \delta\kappa : \int_V \mathbf{x} \, dV \otimes (\mathbf{1} \times \bar{\sigma}) = \\ &= \delta\kappa : V\mathbf{x}^0 \otimes (\mathbf{1} \times \bar{\sigma}) \end{aligned} \quad (4.28)$$

and

$$\sum_e \mathbf{c}^e \cdot \delta\phi^e = \sum_e \mathbf{x}^e \cdot \delta\kappa \cdot \mathbf{c}^e = \sum_e \delta\kappa : (\mathbf{x}^e \otimes \mathbf{c}^e) \quad (4.29)$$

and then the expression for discrete couple stress tensor

$$\delta\kappa : V\bar{\mu} = \delta\kappa : V\mathbf{x}^0 \otimes (\mathbf{1} \times \bar{\sigma}) + \sum_e \delta\kappa : (\mathbf{x}^e \otimes \mathbf{c}^e) \quad (4.30)$$

$$\xrightarrow{\forall \delta\kappa} \\ V\bar{\mu} = V\mathbf{x}^0 \otimes (\mathbf{1} \times \bar{\sigma}) + \sum_e \mathbf{x}^e \otimes \mathbf{c}^e. \quad (4.31)$$

$\int_V \mathbf{x} \, dV = V\mathbf{x}^0$ is the first moment of volume according to equation (A.149).

4.1.2 Virtual work of discrete internal forces

Internal forces (couples) act at contact points c . The forces (couples) act with opposite orientation on two rigid particles J and K with reference points \mathbf{x}_J and \mathbf{x}_K . The internal forces are considered attached to the particles, i.e., the virtual displacement (rotation) is determined from the relative virtual displacement and rotation of particles J and K , see figure 4.1.

We will only consider constant virtual fields

$$\delta\mathbf{u} = \text{const} \quad \delta\mathbf{U} = \mathbf{0} \quad (4.32)$$

$$\delta\phi = \text{const} \quad \delta\kappa = \mathbf{0} \quad (4.33)$$

or linear virtual fields such that

$$\delta\mathbf{u} = \mathbf{x} \cdot \delta\mathbf{U} \quad \delta\phi = \mathbf{x} \cdot \delta\kappa. \quad (4.34)$$

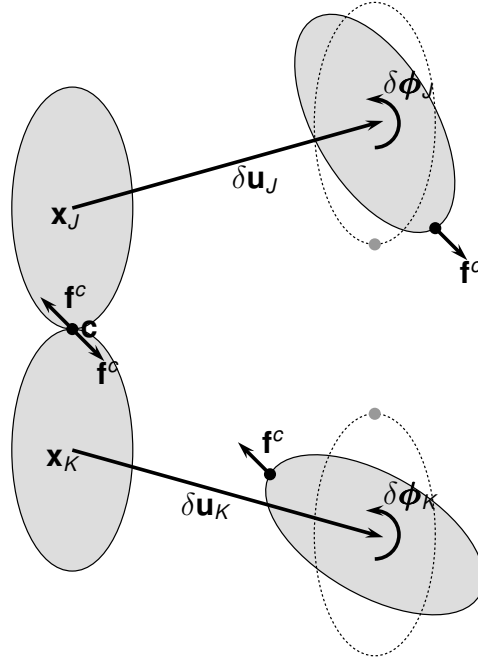


Figure 4.1: Illustration of virtual work of internal forces acting on rigid particles

4.1.2.1 Virtual displacement

Assuming linear virtual displacement (4.34), the virtual work dependent on virtual displacement of one contact reads

$$\begin{aligned} \delta W_u^c &= \mathbf{f}^c \cdot \delta \mathbf{u}_K - \mathbf{f}^c \cdot \delta \mathbf{u}_J = (\delta \mathbf{u}_K - \delta \mathbf{u}_J) \cdot \mathbf{f}^c = (\mathbf{x}_K \cdot \delta \mathbf{U} - \mathbf{x}_J \cdot \delta \mathbf{U}) \cdot \mathbf{f}^c = \\ &= (\mathbf{x}_K - \mathbf{x}_J) \cdot \delta \mathbf{U} \cdot \mathbf{f}^c = \mathbf{I}^c \cdot \delta \mathbf{U} \cdot \mathbf{f}^c = \delta \mathbf{U} : (\mathbf{I}^c \otimes \mathbf{f}^c) \end{aligned} \quad (4.35)$$

with $\mathbf{I}^c = \mathbf{x}_K - \mathbf{x}_J$ being the branch vector of contact c .

The total virtual work of internal forces dependent on virtual displacement is the sum of contributions of individual discrete points c :

$$\delta W_u = \sum_{\text{contact}} \delta W_u^c = \sum_c \delta \mathbf{U} : (\mathbf{I}^c \otimes \mathbf{f}^c) = \delta \mathbf{U} : \sum_c \mathbf{I}^c \otimes \mathbf{f}^c. \quad (4.36)$$

Comparing to the virtual work of the equivalent continuum yields the expression for discrete stress tensor

$$\int_V \boldsymbol{\sigma} : \delta \mathbf{U} dV = \delta \mathbf{U} : V \bar{\boldsymbol{\sigma}} = \delta \mathbf{U} : \sum_c \mathbf{I}^c \otimes \mathbf{f}^c \quad (4.37)$$

$$\begin{aligned} &\xrightarrow{\forall \delta \mathbf{U}} \\ V \bar{\boldsymbol{\sigma}} &= \sum_c \mathbf{I}^c \otimes \mathbf{f}^c. \end{aligned} \quad (4.38)$$

4.1.2.2 Virtual rotation

We assume equivalence of virtual work of internal forces and virtual work of equivalent continuum:

$$\delta \boldsymbol{\kappa} : V \bar{\boldsymbol{\mu}} - (\mathbf{1} \times \bar{\boldsymbol{\sigma}}) \cdot \int_V \delta \boldsymbol{\phi} dV = \delta W_\phi. \quad (4.39)$$

The virtual work dependent on virtual rotation of one contact reads

$$\begin{aligned} \delta W_\phi^c &= \mathbf{c}^c \cdot \delta \boldsymbol{\phi}_K - \mathbf{c}^c \cdot \delta \boldsymbol{\phi}_J + \mathbf{f}^c \cdot (\delta \boldsymbol{\phi}_K \times (\mathbf{c} - \mathbf{x}_K)) - \mathbf{f}^c \cdot (\delta \boldsymbol{\phi}_J \times (\mathbf{c} - \mathbf{x}_J)) = \\ &= (\delta \boldsymbol{\phi}_K - \delta \boldsymbol{\phi}_J) \cdot \mathbf{c}^c + (\delta \boldsymbol{\phi}_K \times (\mathbf{c} - \mathbf{x}_K) - \delta \boldsymbol{\phi}_J \times (\mathbf{c} - \mathbf{x}_J)) \cdot \mathbf{f}^c. \end{aligned} \quad (4.40)$$

The total virtual work of internal forces is the sum of contributions of individual discrete points c :

$$\delta W_\phi = \sum_c \delta W_\phi^c. \quad (4.41)$$

Assuming constant virtual rotation ($\delta \boldsymbol{\phi}_J = \delta \boldsymbol{\phi}_K$) in (4.40) yields

$$\begin{aligned} \delta W_{\phi=const}^c &= \delta \boldsymbol{\phi} \times (\mathbf{c} - \mathbf{x}_K - \mathbf{c} + \mathbf{x}_J) \cdot \mathbf{f}^c = \delta \boldsymbol{\phi} \times (-\mathbf{x}_K + \mathbf{x}_J) \cdot \mathbf{f}^c = \\ &= \delta \boldsymbol{\phi} \times (-\mathbf{I}^c) \cdot \mathbf{f}^c = \delta \boldsymbol{\phi} \cdot (-\mathbf{I}^c) \times \mathbf{f}^c. \end{aligned} \quad (4.42)$$

and substituting into (4.39) yields the expression for the antisymmetric part of stress tensor

$$\delta \boldsymbol{\kappa} : V\bar{\boldsymbol{\mu}} - (\mathbf{1} \times \bar{\boldsymbol{\sigma}}) \cdot \int_V \delta \boldsymbol{\phi} dV = \delta \boldsymbol{\phi} \cdot (-\mathbf{I}^c) \times \mathbf{f}^c \quad (4.43)$$

$$\mathbf{1} \times V\bar{\boldsymbol{\sigma}} = \sum_c \mathbf{I}^c \times \mathbf{f}^c \quad (4.44)$$

Assuming linear virtual rotation (4.34) yields

$$(\mathbf{x}_K \cdot \delta \boldsymbol{\kappa} - \mathbf{x}_J \cdot \delta \boldsymbol{\kappa}) \cdot \mathbf{c}^c = \delta \boldsymbol{\kappa} : (\mathbf{x}_K - \mathbf{x}_J) \otimes \mathbf{c}^c = \delta \boldsymbol{\kappa} : \mathbf{I}^c \otimes \mathbf{c}^c \quad (4.45)$$

$$\delta \boldsymbol{\phi} \times \mathbf{x} \cdot \mathbf{f} = \mathbf{x} \cdot \delta \boldsymbol{\kappa} \times \mathbf{x} \cdot \mathbf{f} = \delta \boldsymbol{\kappa} : (\mathbf{x} \otimes \mathbf{x} \times \mathbf{f}) \quad (4.46)$$

$$\begin{aligned} (\delta \boldsymbol{\phi}_K \times (\mathbf{c} - \mathbf{x}_K) - \delta \boldsymbol{\phi}_J \times (\mathbf{c} - \mathbf{x}_J)) \cdot \mathbf{f}^c &= \delta \boldsymbol{\kappa} : (\mathbf{x}_K \otimes (\mathbf{c} - \mathbf{x}_K) - \mathbf{x}_J \otimes (\mathbf{c} - \mathbf{x}_J)) \times \mathbf{f}^c = \\ &= \delta \boldsymbol{\kappa} : (\mathbf{x}_K \otimes \mathbf{c} - \mathbf{x}_K \otimes \mathbf{x}_K - \mathbf{x}_J \otimes \mathbf{c} + \mathbf{x}_J \otimes \mathbf{x}_J) \times \mathbf{f}^c = \delta \boldsymbol{\kappa} : \mathbf{X}^c \times \mathbf{f}^c \end{aligned} \quad (4.47)$$

$$\delta W_{\phi=homo}^c = \delta \boldsymbol{\kappa} : \mathbf{I}^c \otimes \mathbf{c}^c + \delta \boldsymbol{\kappa} : \mathbf{X}^c \times \mathbf{f}^c. \quad (4.48)$$

and substituting into (4.39) and using (4.28) yields the expression for the discrete couple stress tensor

$$\delta \boldsymbol{\kappa} : V\bar{\boldsymbol{\mu}} - (\mathbf{1} \times \bar{\boldsymbol{\sigma}}) \cdot \int_V \delta \boldsymbol{\phi} dV = \delta W_\phi \quad (4.49)$$

$$\delta \boldsymbol{\kappa} : V\bar{\boldsymbol{\mu}} = \delta \boldsymbol{\kappa} : V\mathbf{x}^0 \otimes (\mathbf{1} \times \bar{\boldsymbol{\sigma}}) + \delta \boldsymbol{\kappa} : \sum_c \mathbf{I}^c \otimes \mathbf{c}^c + \delta \boldsymbol{\kappa} : \sum_c \mathbf{X}^c \times \mathbf{f}^c \quad (4.50)$$

$$V\bar{\boldsymbol{\mu}} = V\mathbf{x}^0 \otimes (\mathbf{1} \times \bar{\boldsymbol{\sigma}}) + \sum_c \mathbf{I}^c \otimes \mathbf{c}^c + \sum_c \mathbf{X}^c \times \mathbf{f}^c, \quad (4.51)$$

where

$$V\mathbf{x}^0 = \int_V \mathbf{x} dV \quad (4.52)$$

is the first moment of volume according to (A.149) and \mathbf{X}^c is

$$\mathbf{X}^c = \mathbf{x}_K \otimes \mathbf{c} - \mathbf{x}_K \otimes \mathbf{x}_K - \mathbf{x}_J \otimes \mathbf{c} + \mathbf{x}_J \otimes \mathbf{x}_J. \quad (4.53)$$

4.1.3 Summary

Based on the equivalence of macro virtual work and virtual work of discrete external forces, the stress and couple stress are defined as

$$V\bar{\sigma} = \sum_e \mathbf{x} \otimes \mathbf{f}^e \quad (4.54)$$

$$V\bar{\mu} = V\mathbf{x}^0 \otimes (\mathbf{1} \times V\bar{\sigma}) + \sum_e \mathbf{x} \otimes \mathbf{c}^e \quad (4.55)$$

The resulting (couple) stress tensor does not depend on the choice of the point of moment equilibrium. The resulting (couple) stress tensor does not depend on the choice of particles' reference points.

Based on the equivalence of macro virtual work and virtual work of discrete internal forces, the stress and couple stress are defined as

$$V\bar{\sigma} = \sum_c \mathbf{l} \otimes \mathbf{f}^c \quad (4.56)$$

$$V\bar{\mu} = V\mathbf{x}^0 \otimes (\mathbf{1} \times \bar{\sigma}) + \sum_c \mathbf{l}^c \otimes \mathbf{c}^c + \sum_c \mathbf{X}^c \times \mathbf{f}^c \quad (4.57)$$

The resulting (couple) stress tensor does not depend on the choice of the point of moment equilibrium. The resulting (couple) stress tensor does not depend on the choice of particles' reference points. The independence of the choice of reference points is required by [17], who also proposed a derivation independent on the choice of particle's reference points. However, the independence is only valid in the absence of body forces and couples (i.e., self-equilibrated internal forces of each particle), which is a rare case in real DEM simulations.

The resulting stress tensor may be asymmetric only in the presence of external couples (either directly applied or as the result of unbalanced internal forces).

[11] and [17] agreed that based on the virtual work principle, only equivalent values of the sum of couple stress and moment of stress (not couple stress itself) can be derived. According to the author's knowledge, the expressions for couple stress tensor $\bar{\mu}$ using pre-computed macro stress tensor $\bar{\sigma}$ and first moment of volume $V\mathbf{x}^0$ have not been published before. A more detailed analysis and literature research (if the result is really a new one) could/should be realized in the future.

4.2 Derivation based on equilibrium conditions

4.2.1 External forces

Equilibrium conditions are the consequence of the virtual work principle, therefore the derivation based on equilibrium conditions results in the same formulas as the derivation based on the virtual work principle.

Consider a region (e.g., one DEM particle) with volume V , centroid \mathbf{x}^0 and applied external discrete forces \mathbf{f}^e and couples \mathbf{c}^e .

Expressing the (couple) stress tensor using its derivatives and position vector (A.82), using divergence theorem (A.76), Cauchy's stress theorem (A.95) and (A.96), local equilibrium conditions (A.99) and (A.100) and considering surface and body loads as Dirac delta

distributions (4.4), we can write discrete stress as a volume average of stress tensor

$$\begin{aligned}
 V\bar{\sigma} &= \int_V \sigma \, dV = \int_V \nabla^m (\mathbf{x} \otimes \sigma) - \mathbf{x} \otimes (\nabla \cdot \sigma) \, dV = \\
 &= \int_S \mathbf{x} \otimes \mathbf{n} \cdot \sigma \, dS - \int_V \mathbf{x} \otimes (\nabla \cdot \sigma) \, dV = \int_S \mathbf{x} \otimes \mathbf{t} \, dS + \int_V \mathbf{x} \otimes \mathbf{f} \, dV = \\
 &= \sum_e \mathbf{x} \otimes \mathbf{f}^e
 \end{aligned} \tag{4.58}$$

and discrete couple stress as a volume average of couple stress tensor

$$\begin{aligned}
 V\bar{\mu} &= \int_V \mu \, dV = \int_V \nabla^m (\mathbf{x} \otimes \mu) - \mathbf{x} \otimes (\nabla \cdot \mu) \, dV = \\
 &= \int_S \mathbf{x} \otimes \mathbf{n} \cdot \mu \, dS - \int_V \mathbf{x} \otimes (\nabla \cdot \mu) \, dV = \int_S \mathbf{x} \otimes \mathbf{m} \, dS + \int_V \mathbf{x} \otimes (\mathbf{c} + \mathbf{1} \times \sigma) \, dV = \\
 &= \int_S \mathbf{x} \otimes \mathbf{m} \, dS + \int_V \mathbf{x} \otimes \mathbf{c} \, dV + \int_V \mathbf{x} \, dV \otimes (\mathbf{1} \times \bar{\sigma}) = \\
 &= V\mathbf{x}^0 \otimes (\mathbf{1} \times \bar{\sigma}) + \sum_e \mathbf{x} \otimes \mathbf{c}^e.
 \end{aligned} \tag{4.59}$$

$\int_V \mathbf{x} \, dV = V\mathbf{x}^0$ is the first moment of volume according to equation (A.149).

4.2.2 Internal forces

This approach is also applicable for internal forces [11, 21]. Each particle is treated separately considering internal forces (couples) with surrounding particles as external forces (couples) with respect to the particle. The overall (couple) stress tensor is evaluated as a volume average of the (couple) stress tensor of each particle.

However, the result depends on the volume assigned to the particles. If the particles represent physical grains, the assigned volume is defined uniquely. If the particles are an artificial discretization, the assigned volume is not defined uniquely.

4.3 Examples

Table 4.1 shows evaluated stress tensor, and couple stress tensor for simple 2D situations.

Table 4.1: 2D illustrations of stress and couple stress tensors

	σ	μ		σ	μ
	$\begin{bmatrix} \cdot & \cdot & \cdot \\ \cdot & \cdot & \cdot \\ \cdot & \cdot & \cdot \end{bmatrix}$	$\begin{bmatrix} \cdot & \cdot & \cdot \\ \cdot & \cdot & \cdot \\ \cdot & \cdot & \cdot \end{bmatrix}$		$\begin{bmatrix} \cdot & \cdot & \cdot \\ \cdot & \cdot & \cdot \\ \cdot & \cdot & \cdot \end{bmatrix}$	$\begin{bmatrix} \cdot & \cdot & 2 \\ \cdot & \cdot & \cdot \\ \cdot & \cdot & \cdot \end{bmatrix}$
	$\begin{bmatrix} 2 & \cdot & \cdot \\ \cdot & \cdot & \cdot \\ \cdot & \cdot & \cdot \end{bmatrix}$	$\begin{bmatrix} \cdot & \cdot & \cdot \\ \cdot & \cdot & \cdot \\ \cdot & \cdot & \cdot \end{bmatrix}$		$\begin{bmatrix} \cdot & \cdot & \cdot \\ \cdot & \cdot & \cdot \\ \cdot & \cdot & \cdot \end{bmatrix}$	$\begin{bmatrix} \cdot & \cdot & 1 \\ \cdot & \cdot & \cdot \\ \cdot & \cdot & \cdot \end{bmatrix}$
	$\begin{bmatrix} 1 & \cdot & \cdot \\ \cdot & \cdot & \cdot \\ \cdot & \cdot & \cdot \end{bmatrix}$	$\begin{bmatrix} \cdot & \cdot & \cdot \\ \cdot & \cdot & \cdot \\ \cdot & \cdot & \cdot \end{bmatrix}$		$\begin{bmatrix} \cdot & 2 & \cdot \\ \cdot & \cdot & \cdot \\ \cdot & \cdot & \cdot \end{bmatrix}$	$\begin{bmatrix} \cdot & \cdot & \cdot \\ \cdot & \cdot & \cdot \\ \cdot & \cdot & \cdot \end{bmatrix}$
	$\begin{bmatrix} \cdot & 2 & \cdot \\ 2 & \cdot & \cdot \\ \cdot & \cdot & \cdot \end{bmatrix}$	$\begin{bmatrix} \cdot & \cdot & \cdot \\ \cdot & \cdot & \cdot \\ \cdot & \cdot & \cdot \end{bmatrix}$		$\begin{bmatrix} \cdot & \cdot & \cdot \\ 1 & \cdot & \cdot \\ \cdot & \cdot & \cdot \end{bmatrix}$	$\begin{bmatrix} \cdot & \cdot & \cdot \\ \cdot & \cdot & \cdot \\ \cdot & \cdot & \cdot \end{bmatrix}$

Part II.

DEM – FEM coupling

There exist two main approaches to modeling of the mechanical behavior of solid materials. One approach is based on the continuum theory and the finite element method (FEM) is usually used for numerical solution, while the other approach considers the material as a set of discrete units (particles) and the discrete element method (DEM) is the main numerical solution method. Both approaches have their fields of application, however, in certain cases they can be combined and used together.

The finite element method is a tool for approximate solution of partial differential equations. In the context of solid mechanics, such equations describe the mechanical behavior of a *continuous* material. FEM underwent intensive development from both engineering and mathematical points of view and is being used for solution of various engineering and scientific problems. Different enhancements and features (adaptive meshing, implicit/explicit solution schemes etc.) were investigated to reduce computational costs or improve usability and performance for different model features/purposes. Despite these facts, FEM is considered not to be suitable for modeling of a large number of discontinuities (i.e., massive fragmentation), especially if a significant number of new contacts between individual “particles” is assumed.

The discrete element method (or particle models in other words) was originally developed for modeling of granular materials, i.e., *discontinuous* matter. Later on, the method was extended to bonded (or cohesive) particle models, resulting in a continuum-like behavior of discrete particles in the elastic range. However, due to its discrete nature, beyond the elastic range the creation of discontinuities (like cracks, damage or even massive fragmentation) together with large displacement effects is very naturally included in the DEM formulation. DEM is usually solved in an explicit sense, which allows easy computer implementation and straightforward contact law definitions, but makes the whole simulation computationally expensive at the same time.

The combination of FEM and DEM methods can be performed in several ways, depending on the context. The vast majority of scientific papers dealing with this topic is aimed at concurrent FEM – DEM coupling, i.e., modeling situations in which the process modeled by DEM and the process modeled by FEM take place at the same time and at least one of them influences the other. Several classes of combination approaches have been developed, as will be discussed later.

In the concurrent approach (see chapter 5), both DEM and FEM simulations have to run at the same time, increasing computational time costs. In the case of multiscale coupling, each FEM integration point possesses its own DEM simulation (where the stress–strain law is determined from the actual microstructure evolution) and the computational costs grow even more due to this fact.

The classification complementary to the concurrent combination is the sequential approach. It assumes that the processes are separable in time and therefore only the former process (a bridge column subjected to an impact load, for example) influences the latter process (e.g., further bridge loading), but not vice versa (further bridge loading does not backward influence the impact). In chapter 6, a DEM to FEM sequential mapping of damaged concrete material is presented. Usually some kind of homogenization technique is used to determine FEM model parameters at the beginning of the latter (e.g., further bridge loading) process from the final state of the former (e.g., an impact on the column) process.

Concurrent coupling methods are computationally expensive. On the other hand, the sequential mapping, due to its “one way” nature, allows, e.g., to use different FEM meshes while running the DEM part only once, reducing additional computation time. Which approach is more suitable depends always on specific physical and simulation context.

5 Concurrent DEM – FEM coupling

As an example of the concurrent coupling of the two methods, consider a dynamic soil compaction. The compacted soil could be modeled by DEM, the compactor by FEM (here we have surface coupling) and the rest of the soil domain by FEM (soil is usually considered as continuous material on a larger scale). The soil DEM / soil FEM interface would probably be of a volume coupling kind. Of course, the FEM soil could be modeled using the multiscale approach, where a certain small representative volume around integration points of the FEM mesh is modeled by DEM (reflecting the discrete nature of the material on lower scale). And we could go in coupling further and further. . .

This example was just to show the variety of possible coupling combinations and that there are a variety of real world problems, where such coupled methods could be useful. Together with the simplicity of creating, modifying and running such simulations and extensibility of the used programs (due to the open source character of the code) it makes this approach attractive for a variety of engineering problems.

There are countless software programs for both FEM and DEM. Some of them are commercial (usually) without possibility to change the code and adjust the behavior to our requirements (combination with another software for instance). However, there exist programs with open source code, which the user can modify, possibly for coupling with other programs. In the present work, coupling of FEM code OOFEM [74, 73] and DEM code YADE [92, 90, 91, 93] is presented. Both programs have the core written in C++ (providing efficient execution of time consuming routines), user interface written in Python (modern dynamic object oriented scripting language, providing easy to use scripting while preserving the C++ efficiency) and extensible object oriented architecture allowing independent implementation of new features - new material model or new particle shapes for instance.

Basic principles and examples of different coupling strategies (surface, volume, multi-scale and contact coupling) are explained in the following sections. All the methods and examples are considered as dynamic problems solved by an explicit scheme. An implicit static solution would be possible, but with much more effort (DEM is not suitable for implicit schemes as discussed in the beginning of chapter 2). One example for each method is presented in this thesis. More examples should be available on the GitHub sites of the author. The source code to the examples is available at `codes/external/fem-dem/examples` and on GitHub, too.

5.1 Surface coupling

The so called surface coupling [64, 70, 101, 32, 66] is probably the most straightforward FEM–DEM coupling strategy.

The principle is to split the whole problem into two separated domains, one modeled by FEM and the other by DEM. As an illustrative example, consider a steel beam modeled by FEM falling into an assembly of gravel particles modeled by DEM. Both domains interact with each other, but are physically separated during the entire time of the process.

If there exists a contact between a finite element and a DEM particle, the repulsive interaction force acts (with opposite direction) on both the DEM particle and on the FEM element. The interaction forces are used as an external load for each domain. The dis-

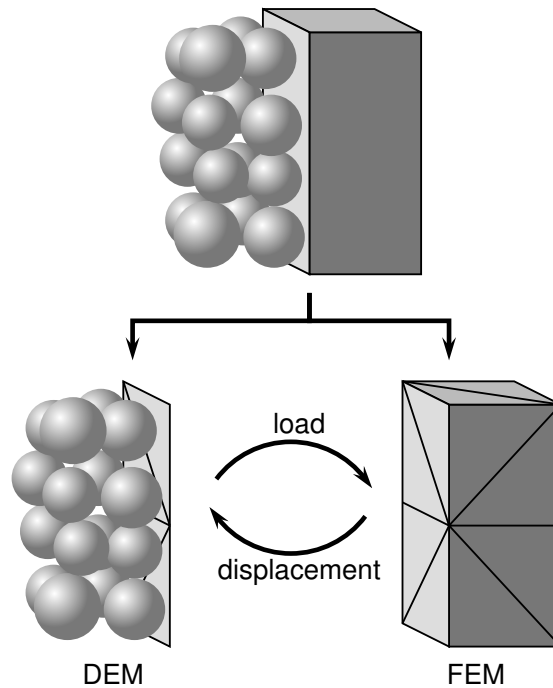


Figure 5.1: Surface coupling illustration

placements of the FEM domain has to be taken into account in the DEM domain.

In the current OOFEM/YADE implementation, the boundary (surface) of the FEM mesh is copied into the DEM part as special triangular particles. Then, in the case of explicit dynamic simulation, in each time step:

- the DEM part is solved;
- the FEM part is solved;
- forces acting on DEM facets are interpolated into vertices and applied on FEM as nodal loads;
- positions of DEM facets are updated according to FEM displacements.

5.1.1 Example

This very simple example is aimed to test the approach, mainly correct contact detection and interaction evaluation. A cantilever is “bombed” by three particles. One particle hits the cantilever “directly”, while two particles hit the cantilever outside its original position (one aspect of the testing). The cantilever is modeled by FEM with linear brick elements. The bottom of the cantilever has fixed displacements. The cantilever surface (set of quadrilateral faces) is triangulated and copied to the DEM part of the simulation. The DEM “impactors” can have different shapes, e.g., spherical or polyhedral. The visual results are shown in figure 5.7, the animation can be found at `text/figs/coupling/surf1`.

5.2 Volume coupling

Volume coupling [82, 107, 5, 105] is similar to the surface coupling. The difference is that the two subdomains overlap each other.

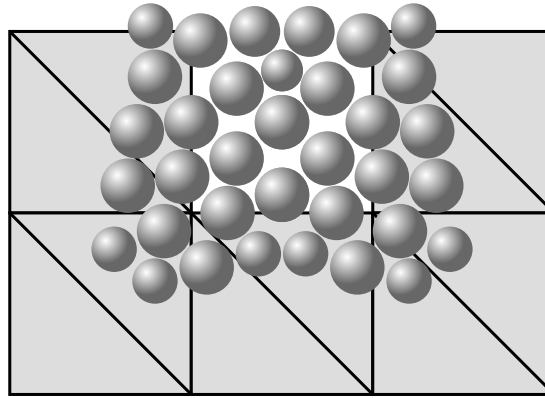


Figure 5.2: Volume coupling illustration

The possible usage of this approach could be a model of concrete beam subjected to an impact load (blast for example). The whole beam would be modeled by FEM and only a small volume of the concrete (the volume to be fragmented and crushed) would be modeled by DEM. To preserve continuous nature of the beam, a transition zone (containing both FEM and DEM) would be included.

There are two basic strategies how to model transition between FEM and DEM domains [107]. The first one, “direct” or “master/slave” method [5], considers DEM particles overlapping with FEM as direct slaves of the FEM mesh (using standard “master/slave” or “hanging nodes” approach). The second one, the “weak” or “Arlequin” method [82, 105], considers a transition bridging zone, where the total response is superposed from contributions of the two models and is interpolated between both domains. In the thesis, only the former (master/slave) approach is described.

In the current OOFEM/YADE implementation, hanging nodes are created at centers of overlapping spheres. Then, in the case of explicit dynamic simulation, in each time step:

- the DEM part is solved;
- the FEM part is solved;
- forces acting on DEM overlapping particles are applied on the corresponding FEM hanging nodes as nodal loads;
- position of overlapping DEM particles are updated according to displacements of the corresponding FEM hanging nodes.

5.2.1 Example

In this example, a simply supported 2D beam subjected to a missile impact was simulated. The sides of the beam body were simulated by FEM as a plane stress problem using quadrilateral elements and linear elastic material law. The central part was modeled by DEM using a regular packing and CPM material model (described in section 2.5). The material parameters and initial conditions are artificially set to get “nice” results. The visual results are shown in figure 5.5, the animation can be found at `text/figs/coupling/vol1`.

5.3 Multiscale coupling

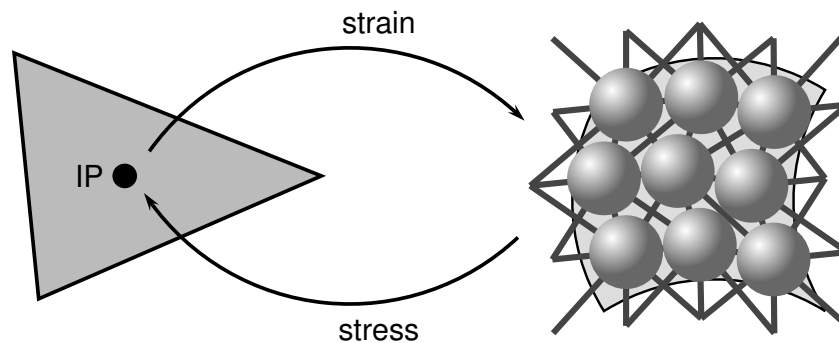


Figure 5.3: Multiscale coupling illustration

The idea of multiscale simulations is to model the problem on the large (macro) scale using information from a lower (micro) scale [80, 105]. In the current context, the (first order) homogenization [35] is presented.

Geometric information (strain) from macro scale – integration points (IPs) of FEM mesh – is transferred to the micro scale (representative volume element - RVE - modeled by DEM). On the micro scale, the boundary value problem (BVP) governed by the transferred prescribed strain is solved using periodic boundary conditions [89]. The output of the micro-scale problem is the stress tensor (sufficient for explicit solution scheme) and possibly also the constitutive characteristics (stiffness tensor, needed by implicit solution schemes), which are transferred back to the macro-scale problem.

As an example of such approach, consider a sample of sand. In reality, it is composed of individual grains, therefore DEM could be the right modeling approach. However, because of very high computational costs of DEM, the sand is considered as a continuum from the macroscopic point of view and FEM is used for macroscopic description. To preserve the particular nature of the sample, the stress–strain law in each integration point is determined not from predefined formulas, but rather from microscale simulations performed on smaller sand samples solved by DEM. Thus we do not need any explicit expression of the material law on the FEM scale (it is determined from the actual micro RVE response).

In the current OOFEM/YADE implementation, separate RVE is generated according to certain criteria for selected integration points. Then, in the case of explicit dynamic simulation, in each time step:

- the FEM part is solved;
- the DEM part is solved;
- strains at IPs are applied to the corresponding RVEs;
- stresses of RVEs are evaluated and adjusted to the corresponding IPs.

5.3.1 Example

Uniaxial strain (oedometric test) of a sample consisting of three different (linear elastic) materials is simulated in this example. The macro-scale problem is modeled by three brick elements. Each FEM element has eight integration points. The upper one is a pure FEM

element. For each integration point of the two bottom elements, different DEM micro-scale RVE simulations are performed.

The visual results are shown in figure 5.8, the animation can be found at `text/figs/coupling/multi1`. In each “DEM” element, one micro RVE result is displayed. The results of linear elastic behavior are not extremely spectacular indeed, but using a nonlinear behavior of RVEs (resulting in a higher stiffness when more inter-particle contacts occur for instance) could be very useful for certain applications.

5.4 Contact coupling

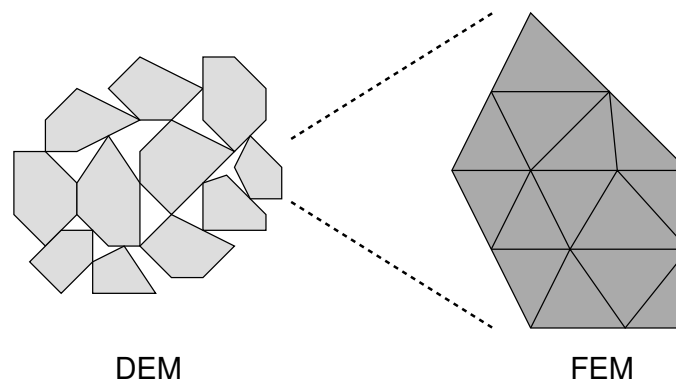


Figure 5.4: Contact coupling illustration

The idea of contact analysis [33] is very simple and opposite to the multiscale approach. The material on the large scale is considered to be of a particulate nature and is modeled by particles using DEM. Each such particle is deformable and further modeled by FEM.

There is no strict border between the cases when the solution can be considered as a contact FEM analysis and when it is already DEM. For only a few particles we would probably use the former one, but when the number of particles increases, the DEM modeling (with its efficient contact detection algorithms) would be more appropriate. This strategy can be actually considered as full FEM, only the contact detection and contact constitutive law is “borrowed” from the DEM program.

In the current OOFEM/YADE implementation, the FEM “particles” are copied into DEM part as polyhedrons. Then, in the case of explicit dynamic simulation, in each time step:

- the DEM part is solved;
- the FEM part is solved;
- forces acting on DEM polyhedrons are interpolated into vertices and applied on FEM as nodal loads;
- position and shape of DEM polyhedrons are updated according to the displacement of the FEM mesh.

5.4.1 Example

In this example, collision of three elastic bodies is presented. All three particles are modeled by FEM, only a detection algorithm is borrowed from DEM. The visual results are shown in figure 5.6, the animation can be found at `text/figs/coupling/contact1`.

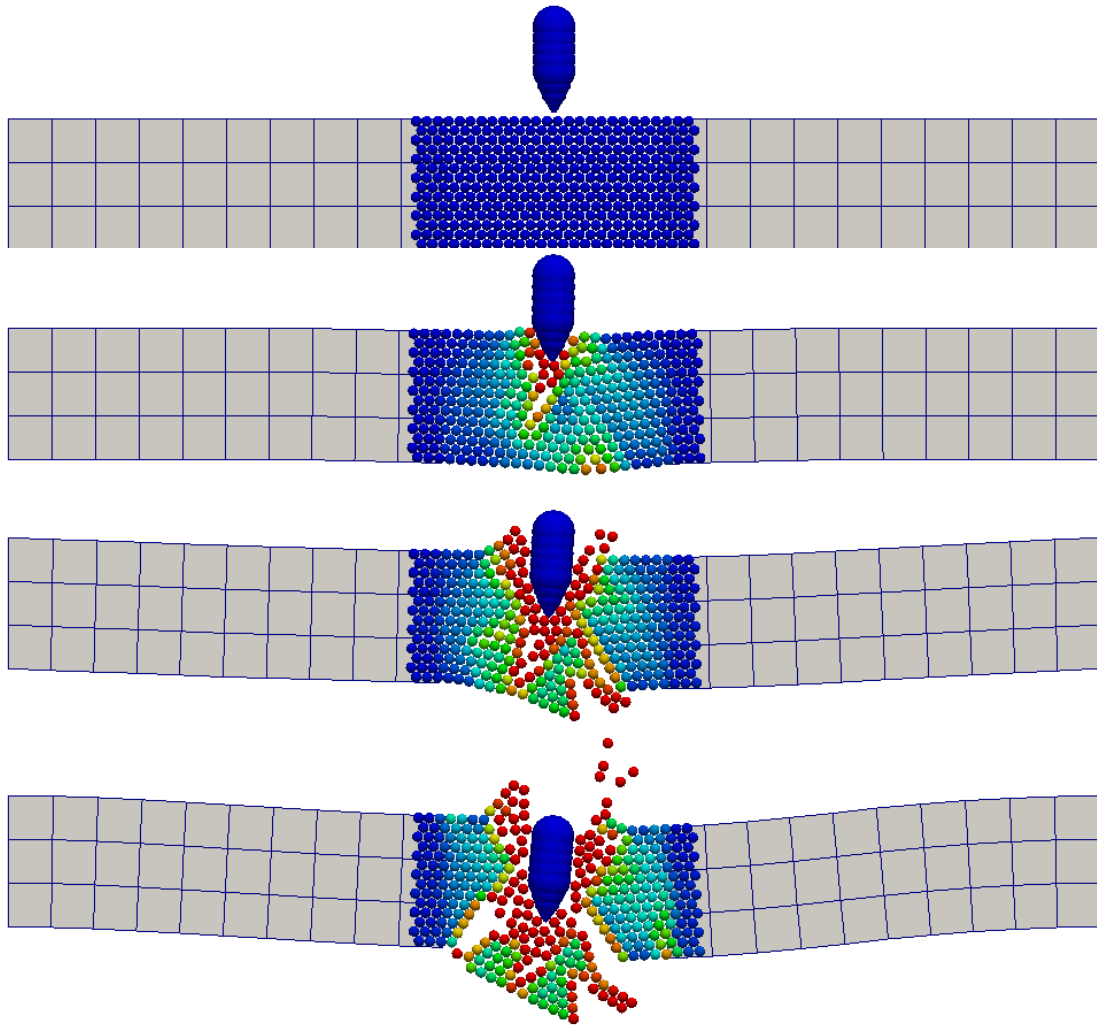


Figure 5.5: Impact on a simply supported beam at different stages

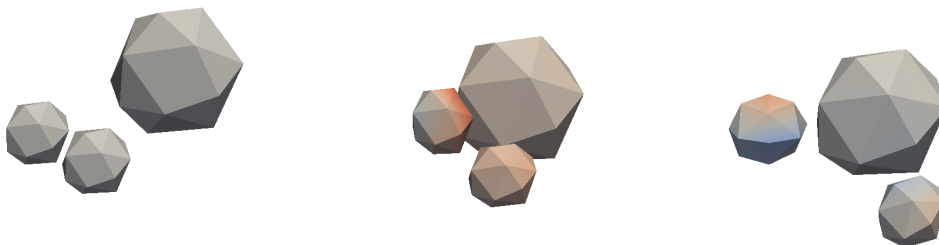


Figure 5.6: Collision of three elastic particles at different stages

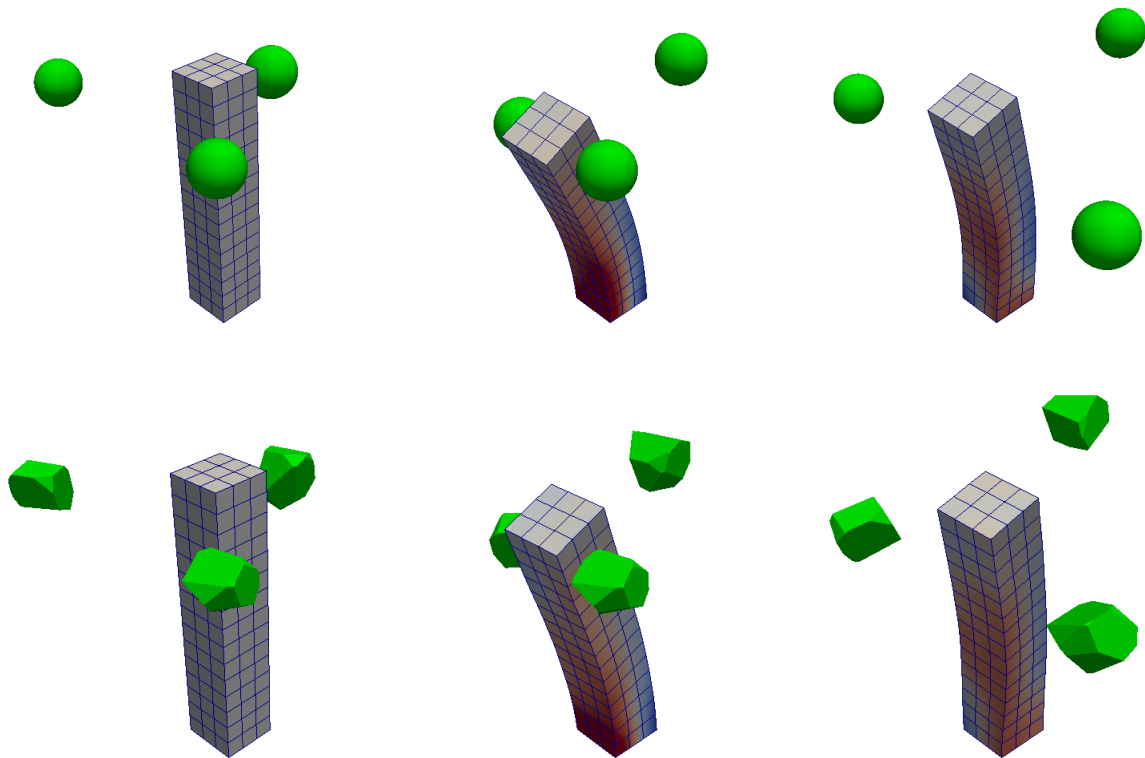


Figure 5.7: Impact on a cantilever at different stages. DEM particles can be spheres (top) or polyhedrons (bottom).

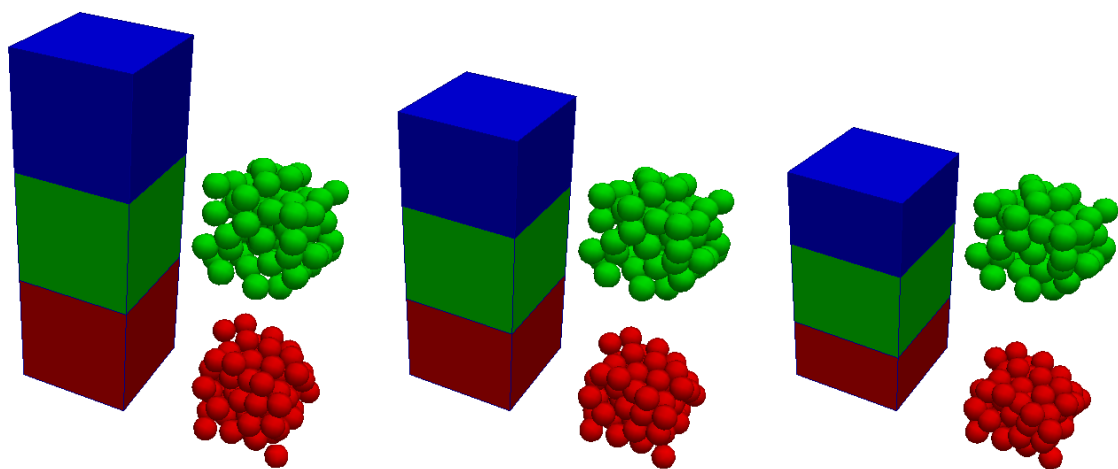


Figure 5.8: Uniaxial strain test at different stages

6 Sequential DEM – FEM coupling

In this chapter, a sequential mapping method from DEM to FEM applied to modeling of fracture of concrete is presented. For example, consider an impact load on a bridge column and then further bridge loading. The two processes are clearly separable in time, where the impact influences the behavior of the bridge under further loading, but not vice versa. From the physical nature, the impact is a dynamic process involving fragmentation and is therefore suitable for DEM. On the other hand, further bridge loading could be a (quasi)static “large-scale” process and is therefore suitable for FEM. The aim of the mapping method is to take the information from a DEM simulation (e.g., damage and stress distribution) and use it within a FEM simulation.

The CPM, cohesive particle model for concrete [92], is chosen for the DEM part. CPM was developed for numerical modeling of concrete under dynamic loading with possibility of massive fragmentation (e.g., crushing) and can be used for simulations of the impact influence.

The DPM, damage-plastic model for concrete failure [39], is chosen for the FEM part. DPM was developed for numerical modeling of concrete under (quasi)static conditions and can be used for further bridge loading simulations.

Theoretically, both impact and further bridge loading processes could be modeled only with CPM model using DEM as a solution tool. However, because of the aforementioned significant computational costs of DEM method, such approach is practically impossible and only a small volume around the impact directly subjected to fragmentation is modeled. Similarly, FEM could be used for both the impact and further bridge loading simulations, but FEM was found, as already mentioned, not to be suitable for modeling of massive fragmentation, which is the case of the impact.

As a conclusion, both methods are used to model different stages of concrete bridge lifetime.

According to the physical background of both CPM and DPM (see section 6.1), the force/stress quantities and damage quantities have to be transferred from CPM to DPM. The proposed method is based on microplane theory and homogenization of discrete forces into the continuous stress tensor and damage in discrete point into the continuous damage. According to the knowledge of the author, no similar work is published in the literature.

The basics and features of both combined models are reviewed in section 6.1. The actual mapping method is described in section 6.2 and illustrated on simple examples in section 6.3.

6.1 Background

In this section, the common features of as well as differences between the DPM and CPM models will be shown. Based on the following equations and relations, the mapping process itself will be derived in section 6.2.

6.1.1 Damage–plastic model for concrete

Some material models (e.g., the DPM model described below) consider the history of loading. Commonly the concept of a model with internal variables is used. Such internal variables (damage for instance) are evaluated and stored only at integration points.

The Damage-Plastic Model (DPM) for concrete [39, 99] is a continuum-based model for concrete failure combining the theories of plasticity and damage. The model is described in detail in the aforementioned papers, thus only the basics of the model are summarized here. This summary is mainly focused on the features used further for combination with the CPM model.

The combination of plasticity and isotropic damage is expressed in the constitutive stress-strain law

$$\boldsymbol{\sigma} = (1 - \omega)\bar{\boldsymbol{\sigma}} = (1 - \omega)\mathbf{D}_e(\boldsymbol{\varepsilon} - \boldsymbol{\varepsilon}_p), \quad (6.1)$$

where $\boldsymbol{\sigma}$ denotes stress, $\bar{\boldsymbol{\sigma}}$ effective stress, ω damage, \mathbf{D}_e elastic stiffness, $\boldsymbol{\varepsilon}$ total strain, $\boldsymbol{\varepsilon}_p$ plastic strain and $\boldsymbol{\varepsilon} - \boldsymbol{\varepsilon}_p = \boldsymbol{\varepsilon}_e$ elastic strain.

The plastic part of the constitutive law is governed by the yield function f_p (which depends on all three invariants of the effective stress tensor $\bar{\boldsymbol{\sigma}}$ and the hardening variable κ_p) and a non-associated flow rule derived from the plastic potential g_p

$$f_p(\bar{\boldsymbol{\sigma}}, \kappa_p) \leq 0, \quad g_p(\bar{\boldsymbol{\sigma}}, \kappa_p) \neq f_p(\bar{\boldsymbol{\sigma}}, \kappa_p), \quad \dot{\kappa}_p = \dot{\kappa}_p(\dot{\boldsymbol{\varepsilon}}_p). \quad (6.2)$$

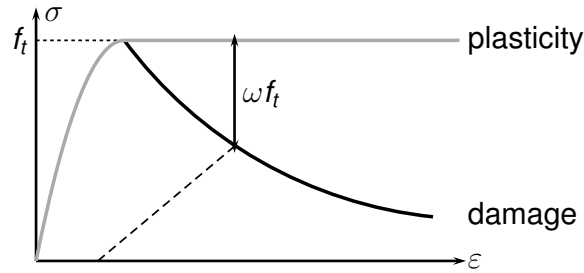


Figure 6.1: Stress-strain diagram of DPM model in uniaxial tension.

The damage part is expressed by the damage evolution function g and the relationships between internal variables κ_D and κ_P

$$\text{damage} \begin{cases} \kappa_p < 1 & \rightarrow & \omega = 0 & (a) \\ \kappa_p = 1 & \rightarrow & \omega = 0 & (b) \\ \kappa_p > 1 & \rightarrow & \omega = g(\kappa_D), \kappa_D = \kappa_p - 1 & (c). \end{cases} \quad (6.3)$$

Damage evolution is driven by the plastic strain $\boldsymbol{\varepsilon}_p$, see (6.2) and (6.3). If $\kappa_p < 1$ (6.3a), no damage occurs. When $\kappa_p = 1$ (6.3b), the plasticity surface takes its final form. After this point, $\kappa_p > 1$ (6.3c) and damage evolution begins.

The law is (due to damage and possible strain localization) dependent on the finite element size.

For the mapping part, the physical meaning of the damage variable ω is important. As is expressed in equation (6.1) and visually in figure 6.1, the physical meaning of DPM damage is the relative reduction of effective stress (or in other words, the relative reduction of strength).

6.1.2 Cohesive particle model for concrete

The Cohesive Particle Model (CPM) for concrete (see [92] and section 2.5) is a discrete model for concrete failure. Figure 6.2 recall the tensile response in normal direction. The physical meaning of damage ω (unlike in the case of DPM model, see figure 6.2) is the stiffness reduction. This difference between DPM and CPM is discussed more in detail in section 6.2.2.1.

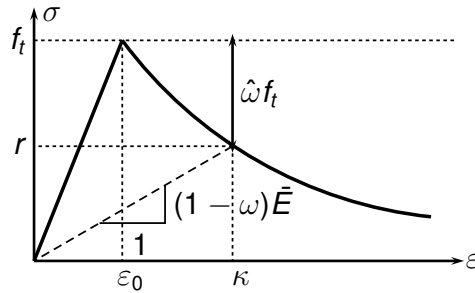


Figure 6.2: Uniaxial stress-strain diagram of one link of CPM model.

6.2 Theory

In this section, the actual mapping method is described. We want to transfer information from the CPM model (used, e.g., for an impact simulation) to the DPM model (used, e.g., for further bridge loading simulations). Because the starting model is discrete and the target model is continuum-based, the required operation is to map discrete quantities into their continuous counterparts.

6.2.1 Stress tensor

The stress tensor is computed according to equation 4.54. Because the considered FEM model is formulated for classical Boltzmann continuum, only the symmetric part is considered.

$$V\sigma = \left(\sum_e \mathbf{x} \otimes \mathbf{f}^e \right)^S \quad (6.4)$$

V , e , \mathbf{x} and \mathbf{f}^e denotes volume assigned to the particle, contact points, position vector of a contact point and force acting on the particle at the contact point, respectively.

6.2.2 Concrete damage

For the purpose of damage mapping, we have to transform damage from both models into a variable with a consistent physical meaning. Because the DPM model is the target of the mapping, the physical meaning of this model (the relative strength reduction) will be chosen. Furthermore, the DPM model uses a scalar damage variable, whereas the CPM model represents damage of individual links containing also directional information. We can therefore define the DEM damage in its tensorial nature.

6.2.2.1 Consistent physical meaning

The following derivation is based on figures 6.1 and 6.2. For each link, the CPM damage ω is converted to the DPM-like damage $\hat{\omega}$. Firstly, the original and current tensile strengths (f_t and r respectively) are evaluated in terms of material properties E and ε_0 and internal variables κ and ω :

$$f_t = E\varepsilon_0, \quad r = (1 - \omega)E\kappa. \quad (6.5)$$

Comparing figures 6.1 and 6.2, we can write

$$\hat{\omega} = 1 - \frac{r}{f_t} = 1 - \frac{(1 - \omega)E\kappa}{E\varepsilon_0} = 1 - \frac{(1 - \omega)\kappa}{\varepsilon_0} \quad (6.6)$$

which is the expression of the CPM damage in the DPM physical meaning.

6.2.2.2 Per-particle overall damage

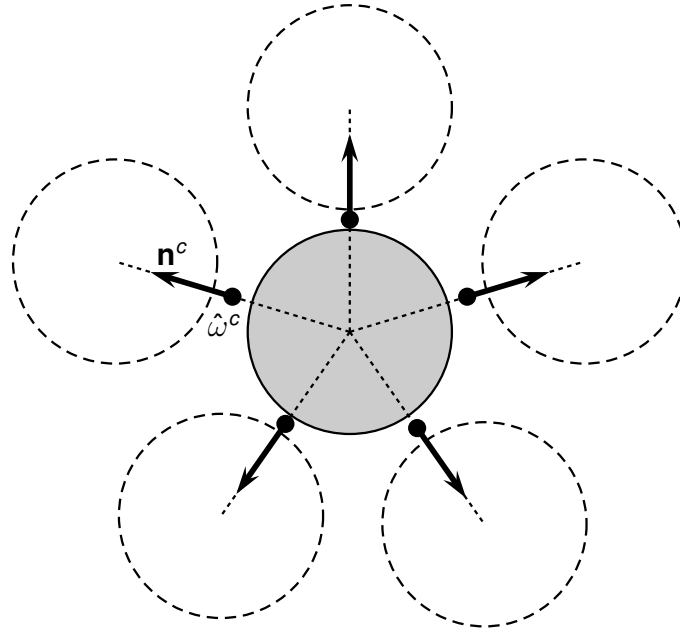


Figure 6.3: Contact points, normals and damage.

The derivation of the damage tensor is inspired by section 3.1. We define the damage tensor Ω as a symmetric second-order tensor such that the difference between link damage $\hat{\omega}^c$ and the projection of the damage tensor Ω to the link direction \mathbf{n}^c is minimal in the least-square sense. Note that the DPM-like damage quantity is used from now on. In mathematical terms, Ω minimizes the following function:

$$\sum_c (\mathbf{n}^c \cdot \Omega \cdot \mathbf{n}^c - \hat{\omega}^c)^2 = \min, \quad (6.7)$$

which means

$$\begin{aligned}
\mathbf{0} &= \frac{\partial}{\partial \Omega} \left[\sum_c (\mathbf{n}^c \cdot \Omega \cdot \mathbf{n}^c - \hat{\omega}^c)^2 \right] = \sum_c 2(\mathbf{n}^c \cdot \Omega \cdot \mathbf{n}^c - \hat{\omega}^c) \mathbf{n}^c \otimes \mathbf{n}^c = \\
&= 2\Omega : \sum_c \mathbf{n}^c \otimes \mathbf{n}^c \otimes \mathbf{n}^c \otimes \mathbf{n}^c - 2 \sum_c \hat{\omega}^c \mathbf{n}^c \otimes \mathbf{n}^c \\
\Omega : \sum_c \mathbf{n}^c \otimes \mathbf{n}^c \otimes \mathbf{n}^c \otimes \mathbf{n}^c &= \sum_c \hat{\omega}^c \mathbf{n}^c \otimes \mathbf{n}^c.
\end{aligned} \tag{6.8}$$

According to [51] and equation (3.32), the approximation of a discrete set of normal vectors by uniformly distributed normals can be written as

$$\frac{1}{N} \sum_c \mathbf{n}^c \otimes \mathbf{n}^c \otimes \mathbf{n}^c \otimes \mathbf{n}^c \approx \frac{1}{4\pi} \int_{\Omega} \mathbf{n}^c \otimes \mathbf{n}^c \otimes \mathbf{n}^c \otimes \mathbf{n}^c d\Omega. \tag{6.9}$$

Substituting equation (6.9) into (6.8) and using (A.127) (A.49) and (A.52) we can write

$$\begin{aligned}
\Omega : (3\mathbb{I}^V + 2\mathbb{I}^S) &= \frac{15}{N} \sum_c \hat{\omega}^c \mathbf{n}^c \otimes \mathbf{n}^c \\
3\Omega^V + 2\Omega &= \frac{15}{N} \sum_c \hat{\omega}^c \mathbf{n}^c \otimes \mathbf{n}^c.
\end{aligned} \tag{6.10}$$

To solve equation (6.10), firstly the trace of the damage tensor $\text{tr}(\Omega)$ is evaluated with the help of identities (A.36) and (A.63):

$$\begin{aligned}
\text{tr}(3\Omega^V + 2\Omega) &= \text{tr} \left(\frac{15}{N} \sum_c \hat{\omega}^c \mathbf{n}^c \otimes \mathbf{n}^c \right) \\
5\text{tr}(\Omega) &= \frac{15}{N} \sum_c \hat{\omega}^c \quad \rightarrow \quad \text{tr}(\Omega) = \frac{3}{N} \sum_c \hat{\omega}^c.
\end{aligned} \tag{6.11}$$

This means that the mean value of the damage tensor

$$\Omega_m = \frac{1}{3} \text{tr}(\Omega) = \frac{1}{N} \sum_c \hat{\omega}^c \tag{6.12}$$

is the average of individual discrete damages, which has a clear physically meaning.

When the trace of the damage tensor $\text{tr}(\Omega)$ is known according to (6.11), the actual damage tensor can be expressed as:

$$\begin{aligned}
3\Omega^V + 2\Omega &= \text{tr}(\Omega) \mathbf{1} + 2\Omega = \frac{15}{N} \sum_c \hat{\omega}^c \mathbf{n}^c \otimes \mathbf{n}^c \\
\Omega &= -\frac{1}{2} \text{tr}(\Omega) \mathbf{1} + \frac{15}{2N} \sum_c \hat{\omega}^c \mathbf{n}^c \otimes \mathbf{n}^c = -\frac{3}{2N} \sum_c \hat{\omega}^c + \frac{15}{2N} \sum_c \hat{\omega}^c \mathbf{n}^c \otimes \mathbf{n}^c.
\end{aligned} \tag{6.13}$$

As shown by equation (6.12), the mean value of the damage tensor always equals the average damage, thus it is always in the range $[0, 1]$. However, its principal values may be negative or greater than 1, as shown in examples below.

Examples

The approach is illustrated on an artificial arrangement of axis aligned directions. Table 6.1 shows computed principal values for different values of damage in different directions. Because the presented damage tensor evaluation assumes uniform distribution of directions (which is not the case for 3 directions), the results sometimes differ from intuitively expected values. On the other hand, the examples naturally illustrates the possibility of negative values or values greater than 1.

Script `codes/scripts/damageTensor/example.py` shows convergence to expected results (the damage is artificially set as $\hat{\omega}^c = \mathbf{n}^c \cdot \mathbf{\Omega} \cdot \mathbf{n}^c$) as the number of direction increases.

6.2.3 Mapping

Auxiliary formulas derived in the previous sections will be used in this section for the actual mapping. The mapping method is sequential, i.e., firstly the DEM simulation is run and the stress tensor and damage tensor are saved for all particles. This information is then included in the FEM simulation. Both simulations can be run independently, e.g., the FEM simulation can be done with different meshes without the need of recomputing the DEM part, or the DEM part can be run independently of the FEM mesh. This approach also allows to use independent averaging methods.

In DEM simulations, the stress tensor σ and damage tensor $\mathbf{\Omega}$ are computed for each particle according to formulas (6.4) and (6.13), respectively. Before the FEM simulation, the mesh to be used must be known (in particular the coordinates of integration points). For each integration point, the stress tensor and damage tensor are averaged and passed to the FEM simulation. The averaging may be of any type.

In the DPM part of the mapping, the following process is performed for each integration point. The damage scalar is evaluated from the averaged damage tensor (in particular from its principal values), generally

$$\omega = \omega(\mathbf{\Omega}) = \omega(\Omega_1, \Omega_2, \Omega_3). \quad (6.14)$$

The specific form of the $\omega(\Omega_1, \Omega_2, \Omega_3)$ function is dependent on material properties and typical loading scenarios for given situation.

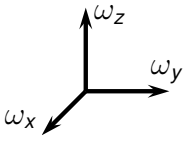
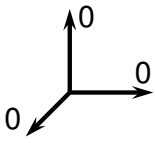
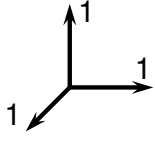
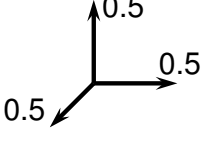
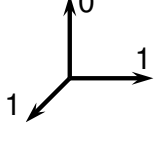
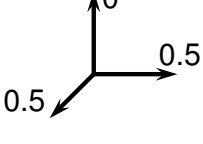
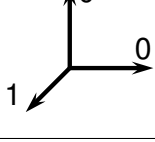
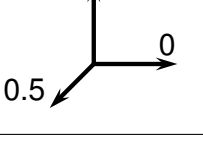
For the known damage scalar ω , the corresponding internal variables κ_D and κ_P have to be evaluated. Because the DPM damage law $\omega = g(\kappa_D)$ (relating κ_D and ω) is element-size dependent, the following operations are done, when the element size is already known:

$$\begin{cases} \omega \leq m & \rightarrow \kappa_D = 0, & \kappa_P = \kappa_P(\omega), & \omega = 0 \\ \omega > m & \rightarrow \kappa_D = g^{-1}(\omega) & \kappa_P = \kappa_D + 1. \end{cases} \quad (6.15)$$

For very low values of resulting damage, less than a certain m , the corresponding DPM material state would be plastic (before the onset of damage). Therefore the first $\kappa_P = \kappa_P(\omega)$ is computed and then $\omega = 0$ is further considered. See the example in the next section for illustration.

At the beginning of the FEM simulation, the actual total strain is not known. Therefore we assume the total strain to be zero. To preserve the elastic strain consistent with the stress tensor, a fictitious value of the plastic strain tensor (i.e., a value which does not necessarily correspond to the real physical plastic strain) is evaluated according to the

Table 6.1: Principal values of damage tensor for various damages

	$(\Omega_x, \Omega_y, \Omega_z)$	$\frac{\text{tr}(\Omega)}{3}$
	$(0, 0, 0)$	0
	$(1, 1, 1)$	1
	$(0.5, 0.5, 0.5)$	0.5
	$(1.5, 1.5, -1)$	$\frac{2}{3}$
	$(0.75, 0.75, -0.5)$	$\frac{1}{3}$
	$(2, -0.5, -0.5)$	$\frac{1}{3}$
	$(1, -0.25, -0.25)$	$\frac{1}{6}$

DPM stress–strain law (6.1):

$$\sigma = (1 - \omega)\mathbf{D}_e : (\boldsymbol{\varepsilon} - \boldsymbol{\varepsilon}_p) \xrightarrow{\boldsymbol{\varepsilon}=0} \boldsymbol{\varepsilon}_p = -\frac{1}{1 - \omega}\mathbf{D}_e^{-1} : \sigma \quad (6.16)$$

The evaluated plastic strain therefore corresponds to the real plastic strain minus the unknown initial total strain.

After this point, the FEM simulation is run in the usual way.

6.3 Example - uniaxial compression

In this section, the results of proposed method are shown on simple “one element” tests. The simulated prismatic specimen is subjected to uniaxial compression. In the case of a one-element FEM simulation, the definition of boundary conditions is straightforward. In the DEM simulation, the axial strain is imposed by prescribed displacements at the top and bottom boundary layers. In the lateral directions, the particles are free to move. For the graphical post-processing, the stress values from DEM simulation are obtained as the normal component in the axial direction of the average stress.

The DEM and FEM material parameters are set such that the resulting stress-strain diagrams are as similar as possible. Figure 6.4 shows a very good agreement of the two models in both pre-peak and post-peak regime. However, the two models differ at the peak load (the CPM softening starts prior to the DPM softening).

The DEM specimen is loaded at a certain level and then possibly unloaded. At the final stage of the DEM simulation, relevant quantities are mapped onto the one-element FEM simulation and the FEM simulation is run. The average stress tensor and average damage tensor are evaluated from all “ordinary” particles (not belonging to the layer imposing boundary conditions).

Based on numerical testing, the damage transformation law

$$\omega = 2.09 (0.85\Omega_1 + 0.15\Omega_3)^{4.7} \quad (6.17)$$

was chosen. Ω_1 denotes the maximum principal value of the damage tensor and Ω_3 the minimum one. See figure 6.5.

For the DPM plastic stage before damage onset (6.15),

$$\text{if } \omega \leq m \text{ then } \kappa_D = 0, \kappa_P = \kappa_P(\omega), \omega = 0, \quad (6.18)$$

the following value and formula

$$m = 5 \cdot 10^{-4} \quad \kappa_P = 0.3 + 900\omega \quad (6.19)$$

were chosen after numerical testing.

Graphs in figures 6.6 and 6.7 show results of the CPM simulation (grey) and continuation with the mapped DPM model (black). The presented results show a reasonable approximation of the FEM behavior after the transformation from DEM. The biggest error is obtained, if the mapping occurs around the peak (or after unloading from around the peak) where the results of two presented models differ the most.

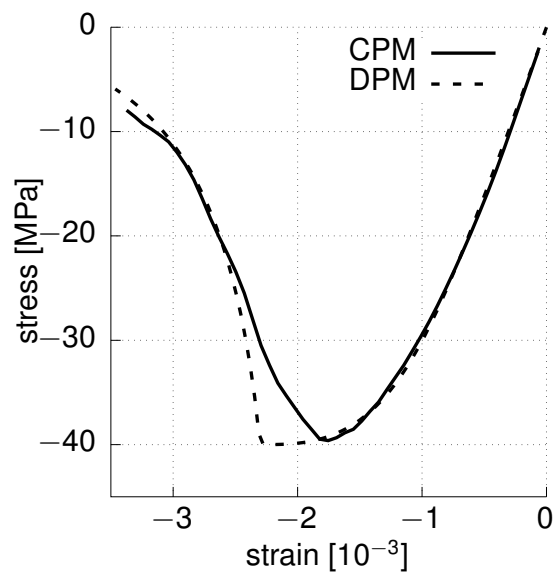


Figure 6.4: Stress-strain diagrams for individual models

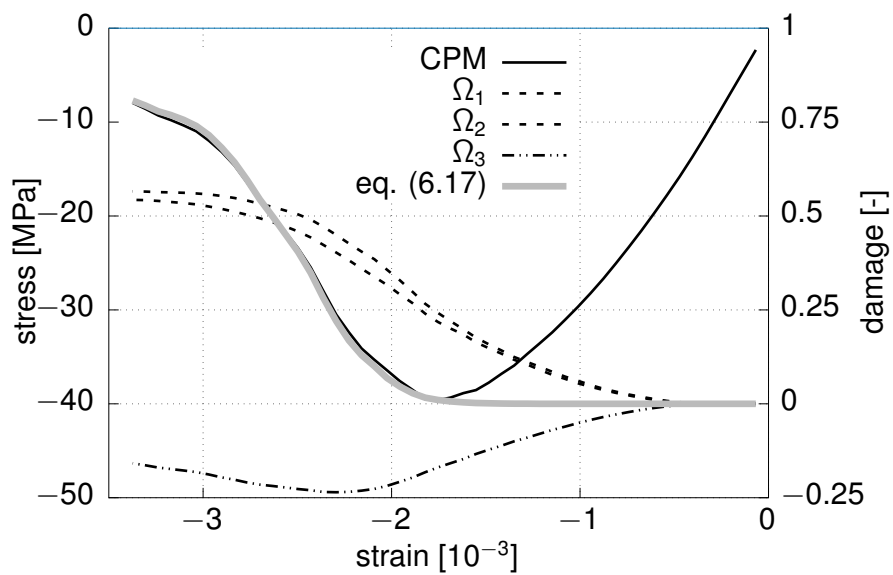


Figure 6.5: Chosen damage transformation law reflecting residual strength of CPM model

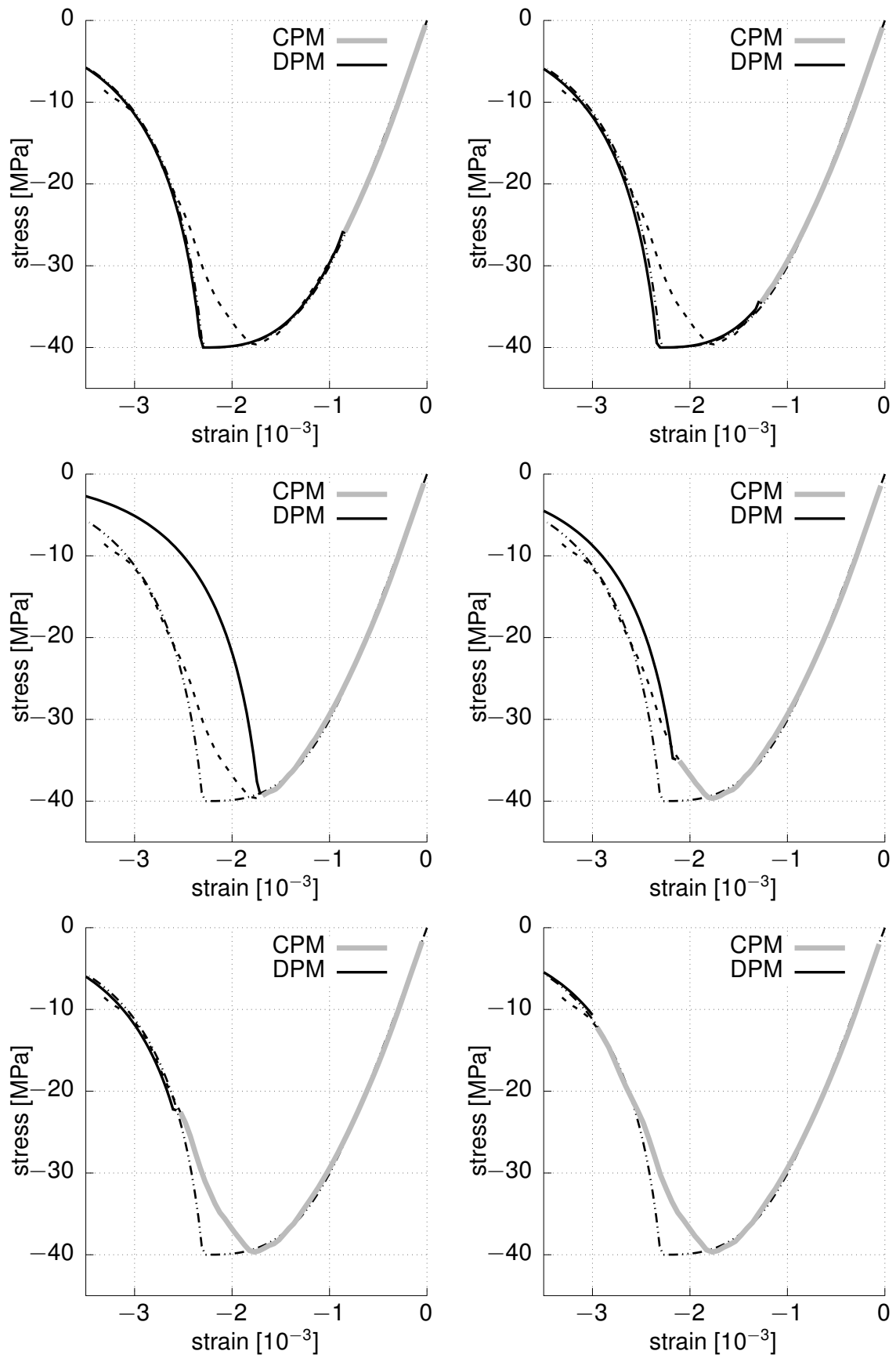


Figure 6.6: Results of mapping at monotonic loading

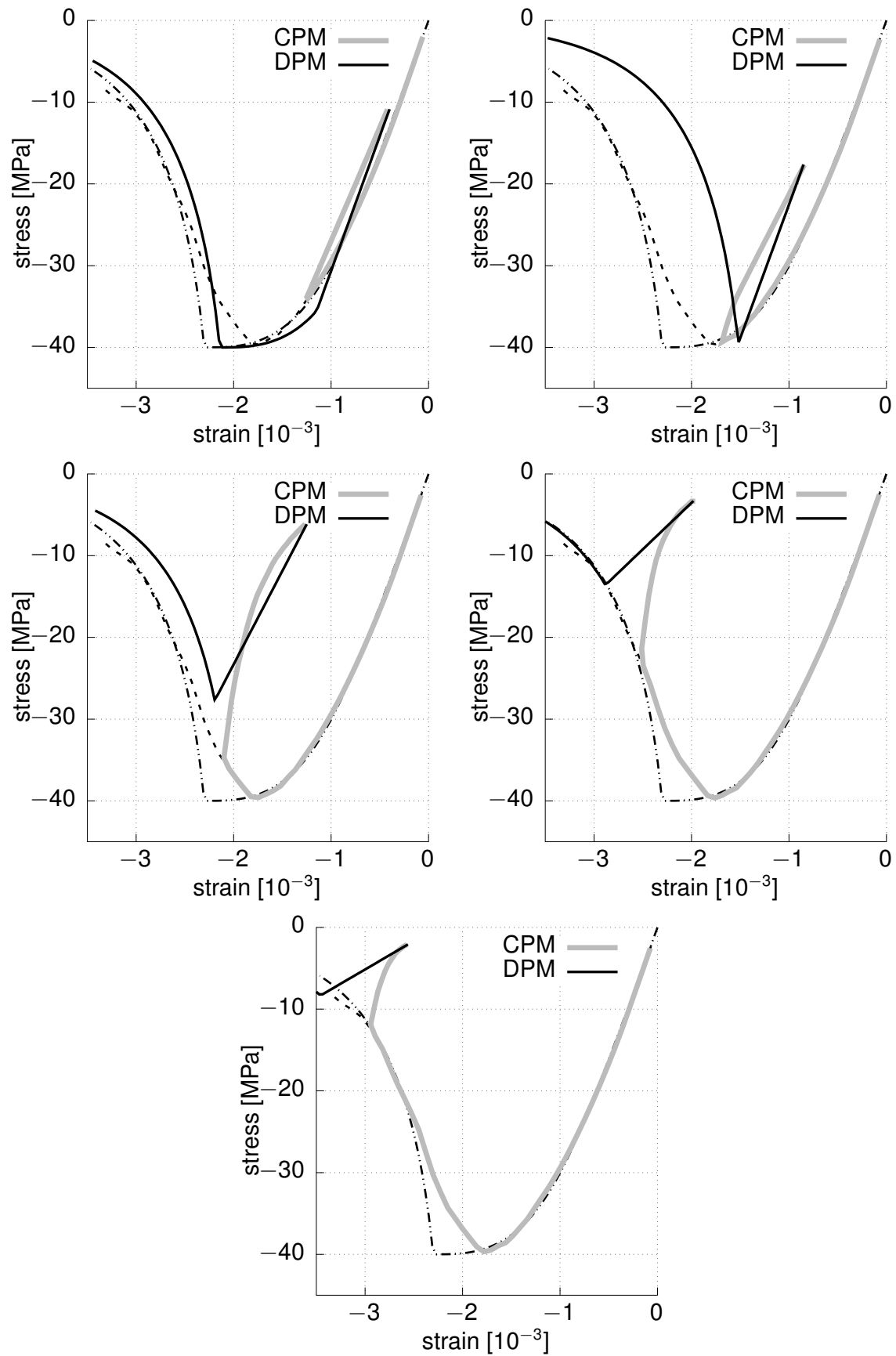


Figure 6.7: Results of mapping at unloaded state

Part III.

Mesoscale Discrete Element Model for Concrete

For description of a homogeneous material, only the overall geometry of investigated region and one set of material properties are needed. If the heterogeneities are considered, their geometry (position, shape and orientation) together with more than one set of material properties have to be specified. The material properties can be assumed as a function of position, i.e., each material point can have unique properties, or the situation may be simplified with the assumption that the properties of a material point depend only on the constituent and do not vary within the constituent.

In science and engineering, concrete is described on different scales, depending on the purpose. In practical civil engineering, concrete is usually described as a homogeneous isotropic material. However, for some applications, the heterogeneous internal structure of concrete plays a crucial role.

Investigated on mesoscale, concrete may be considered as a composition of continuous binder (usually hardened cement paste) matrix with inserted aggregates (such as crushed rocks, gravel or sand) and air voids (pores).

For modeling purposes, the interface transition zone (ITZ) between aggregates and matrix plays a special role.

This chapter describes the development of a discrete mesoscale model for concrete.

7 State of the art

Various approaches of mesoscale concrete modeling have been published. All of them consider concrete as a matrix-based composite with aggregates as inclusions, possibly also with pores. The approaches may be classified from several points of view.

The first significant difference is whether the model is formulated in two dimensions (see, e.g., [6, 44, 104, 55, 56, 61, 72, 75, 84, 103, 108, 111, 112, 78, 43, 40, 41, 113, 36]) or in three dimensions (see, e.g., [19, 55, 55, 86, 97, 106, 49, 15, 109, 62, 22, 23, 25, 24, 50, 27, 26]). Although the 3D models describe the heterogeneous geometry (apart from very special cases) more realistically, some ideas and approaches from 2D models may be useful and applicable also for the 3D case.

According to the numerical method used, the approaches can be divided into continuum and discrete based. Although the main purpose of this work is to develop a discrete mesoscale model, continuum based approaches can be very inspiring, especially in the context of ITZ material models. Most of the continuum based works use FEM as a numerical solution tool [19, 44, 104, 55, 56, 71, 75, 84, 86, 108, 111, 112, 87, 15, 113], but also other methods (meshfree methods [36] or SPH method [60] for instance) are used.

The discrete element method can model disintegration of materials and is therefore also very popular in the context of concrete modeling, especially for scenarios like fragmentation, impact or explosion problems etc. How DEM is used for mesoscale concrete modeling, see, e.g., [6, 16, 42, 45, 47, 54, 57, 61, 72, 97, 103, 78, 43, 40, 41, 109, 62, 22, 23, 25, 24, 27, 26].

7.1 Mesoscale geometry

The concrete heterogeneous geometry (i.e. amount, sizes, shapes and orientation of aggregates and pores) plays an important role in the realistic description of concrete mesoscale behavior. The authors use various ways of definition of aggregate geometry, from extremely simplified regular uniformly sized hexagonal particles (see [84] and figure 7.1 top left) through commonly used spherical/circular (see, e.g., [6, 19, 75, 86, 103, 106, 108, 111, 112, 110, 49, 43, 40, 41, 109, 62, 50, 68, 27, 26] and figure 7.1 top middle) or ellipsoidal/elliptical (see, e.g., [42, 44, 55, 56, 87, 49] and figure 7.1 top right) representation to more sophisticated approximation by polygons/polyhedrons [53, 72, 75, 49, 78, 113] and figure 7.1 bottom left, or representation of aggregates by the series of harmonic functions [34, 44, 83] and figure 7.1 bottom right.

For method testing and validation, there also exist experiments with artificially created mesoscale geometries, where large aggregates have predefined size, position and orientation, see [98, 14] and figure 7.2.

The aggregates are modeled as one rigid particle [43, 103, 109, 27, 26] or as a cluster of particles/elements (e.g., spheres in DEM), see figure 7.3 [6, 40, 41, 42, 49, 72, 78]. Such clustered particles may be rigid or deformable.

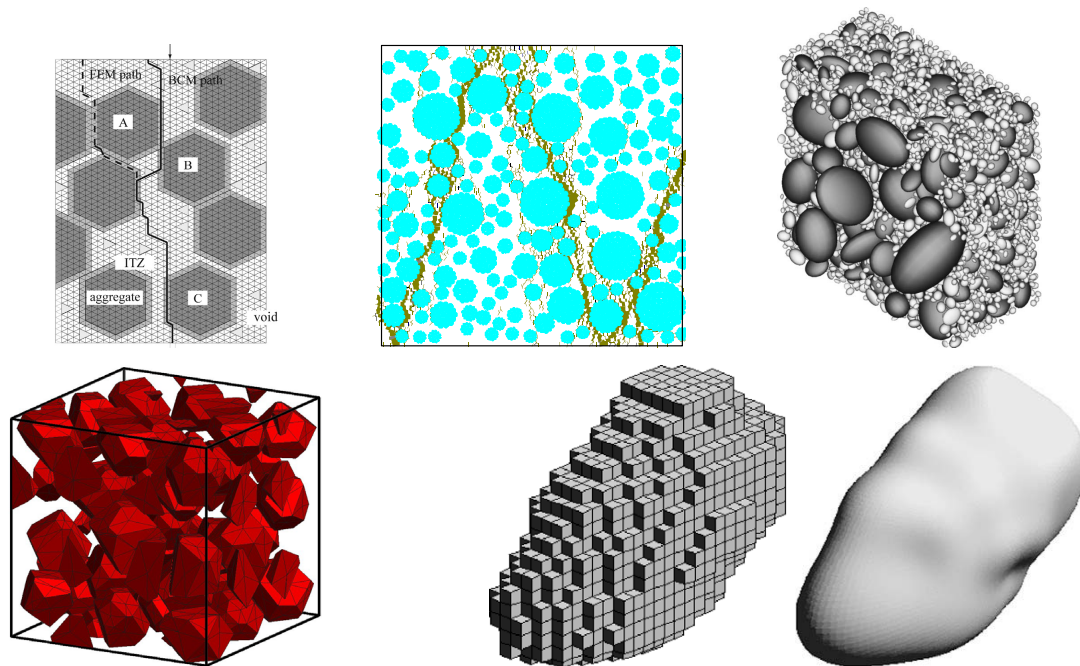


Figure 7.1: Examples of geometrical representation of aggregates: hexagonal [84] (top left), circular [6] (top middle), ellipsoidal [44] (top right), polyhedral [15] (bottom left) and using spherical harmonics [83] (bottom right)

7.2 Material models for mortar and aggregates

For practical and computational reasons, both matrix and individual aggregates are modeled as homogeneous components. Some authors (e.g., [15, 19, 22, 36, 40, 41, 43]) consider aggregates as non damageable, so cracks and damage can only propagate in the matrix. This assumption is reasonable for certain loading scenarios, but is not applicable in a general case, where cracks can propagate also through aggregates (e.g., for light-weight concrete or for dynamic loading).

Although all three phases of concrete composite material may be modeled with different material models [111, 110], many authors use for matrix, aggregates and ITZ the same material model [6, 42, 43, 49, 63, 72, 84, 103, 109, 112].

In the case of continuous (FEM) models, the material model for matrix and aggregates is usually based on damage-plasticity models.

The discrete models usually work with a more or less complex contact law and a link failure envelope. See, e.g., [23, 43, 47, 78, 97, 103] or figure 7.5.

Several rock material models (usable for aggregate description) are published in the literature [31, 46, 18, 67, 76, 81, 85, 59, 94, 102]. Some of them (see, e.g., [67, 85, 59] or figure 7.6) are quite similar to the models of concrete or mortar.

7.3 Interface transition zone

Apart from separated matrix and aggregates, the interface between these components needs to be properly specified for realistic modeling of inelastic processes (crack initiation and propagation for instance). The interface is a very special region of concrete, occupying a minimal volume, but having a significant influence on resulting concrete properties.

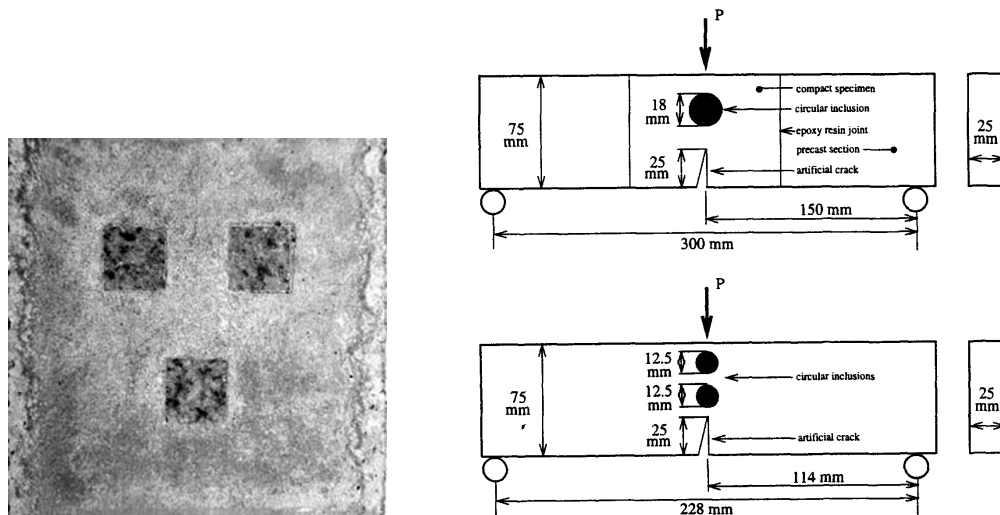


Figure 7.2: Examples of artificial geometry: [98] left and [14] right

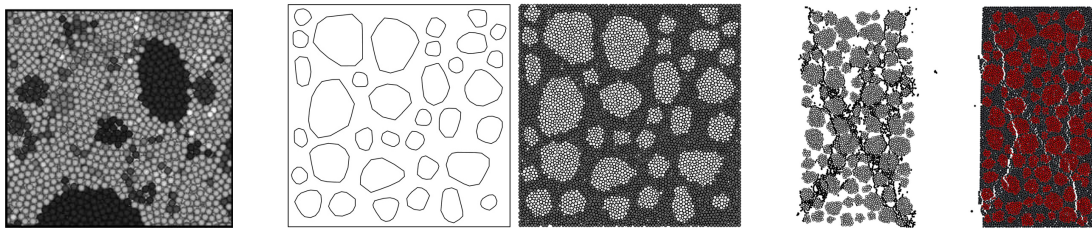


Figure 7.3: Illustration of aggregate representation as a cluster of DEM particles: [42] (left), [78] (middle) and [72] (right)

The special role of ITZ is given by both mechanical and chemical reasons, being investigated mathematically and experimentally [30, 37, 38, 79].

From the simulation point of view, the ITZ is often described by the same type of material model as the other constituents, but is considered as the weakest part of the concrete composite, which is reflected in the material parameters choice; see figure 7.7.

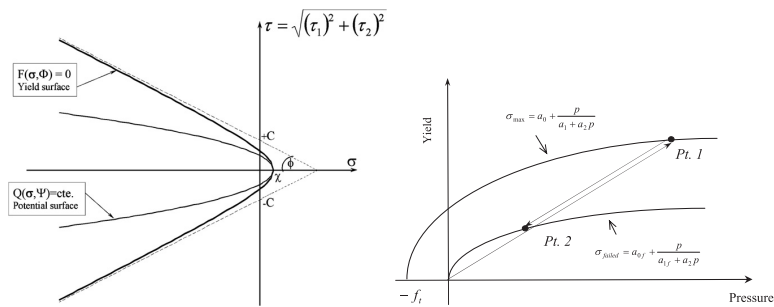


Figure 7.4: Interface model according to [15] (left) and [108] (right)

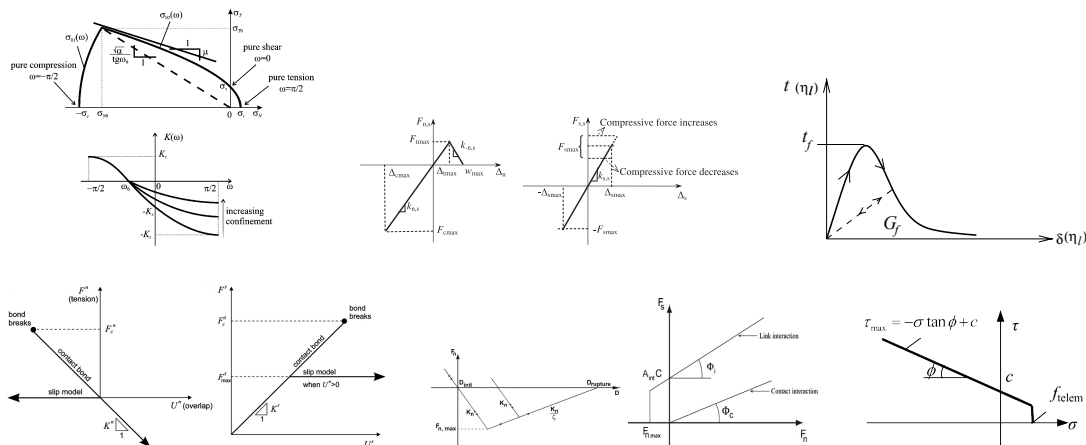


Figure 7.5: Illustration of material models according to [23] (top left), [43] (top middle), [47] (top right), [78] (bottom left), [97] (bottom middle) and [103] (bottom right)

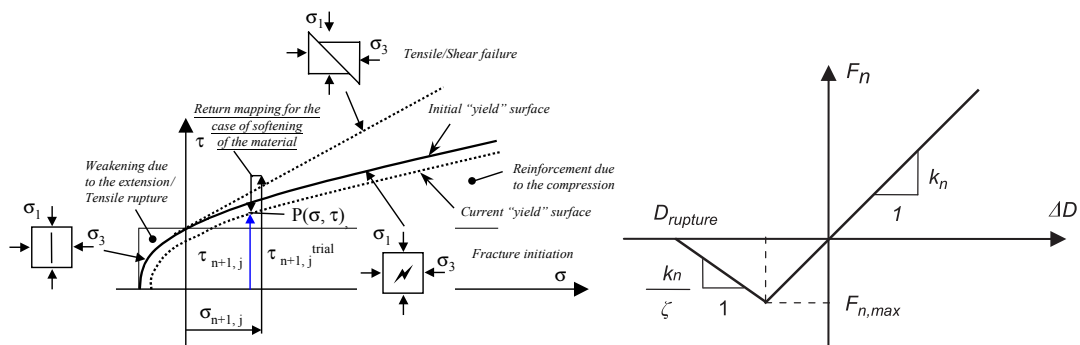


Figure 7.6: Illustration of constitutive law according to [67] (left), and [85] (right)

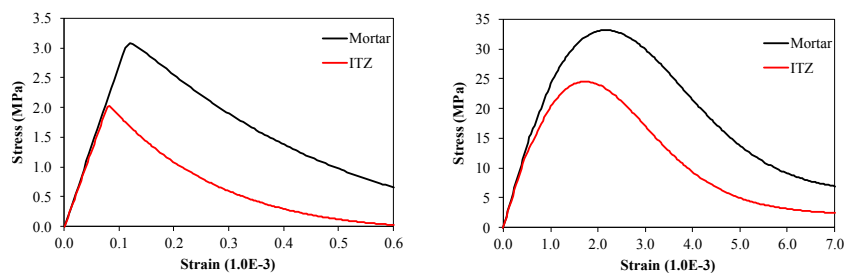


Figure 7.7: ITZ modeled by the same material model, only with different parameters [49]

8 New mesoscale discrete element model for concrete

According to the best knowledge of the author, no three-dimensional mesoscale spherical discrete element model for concrete, sufficiently validated against experiments, is published in the literature. Spherical-like Voronoi diagram based lattice models (e.g., [16, 22, 41, 47, 103, 109]) might seem to be a solution, but such models do not consider new contacts, the link representation is different from classical spherical discrete elements, etc. As a consequence, a new model is proposed.

8.1 New model definition

According to the presented literature study, the author's experience and available simulation tools, the new mesoscale concrete particle model (MCPM) development is summarized in this section.

The discrete element method, using open-source software YADE, is used as a numerical simulation tool.

The material model considered is the CPM, summarized in section 2.5. The model considers concrete as a three-phase composite composed of cement paste/mortar matrix, (disordered) aggregates and interfacial transition zone (ITZ) between matrix and aggregates. The same material model (with different parameters) is considered for all the constituents.

The presented approach considers two types of DEM particles - particles belonging to aggregates and particles belonging to cement mortar. As a consequence, 3 types of links are possible: aggregate-aggregate, mortar-mortar and aggregate-mortar. The aggregate-mortar type of links will be called interface links in this thesis. The material of particles is determined according to the center and size of the particle and according to the geometrical representation (size, shape and orientation) of aggregates. Figure 8.1 illustrates the approach.

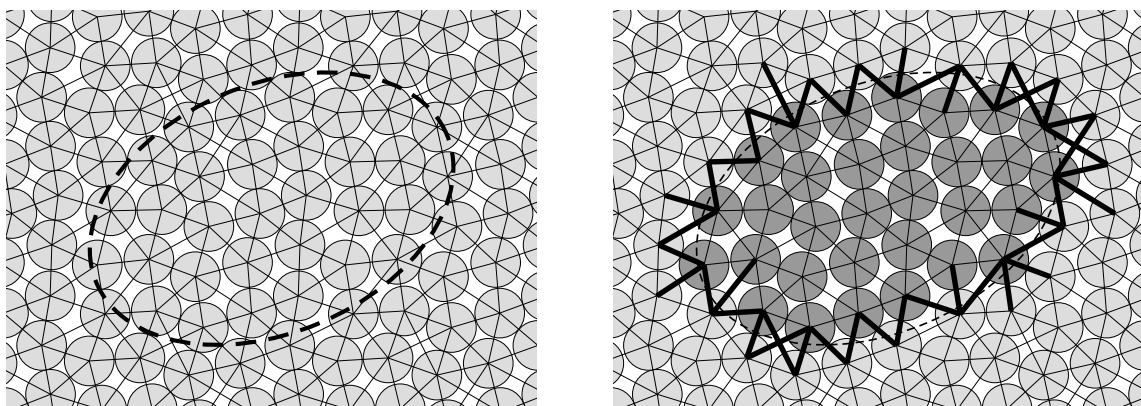


Figure 8.1: Illustration of MCPM geometry definition. Light particles correspond to mortar, dark particles to aggregates and thick links to interface

The material models for all constituents (mortar, aggregates, and ITZ) is modeled by

the Concrete Particle Model [92]. The same model for individual phases is usual among other authors, see section 7.

The material properties are constant within mortar and single aggregates (but different aggregates may have different parameters, e.g., simulating concrete with several different aggregate types). Using this approach, no parts of material are considered as rigid and every part of material may exhibit nonlinear behavior (i.e., aggregates will be deformable and damageable), see figure 8.2 for illustration.

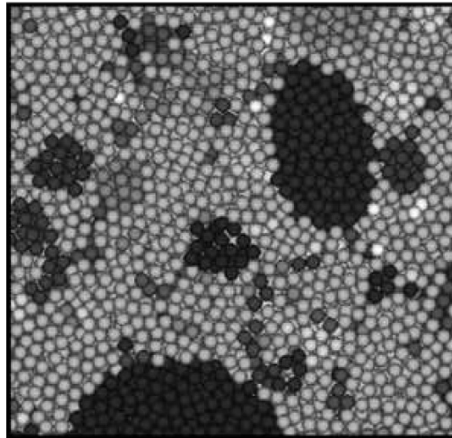


Figure 8.2: Illustration of clustered aggregate according to [42]. Different shades indicates different materials

In YADE default implementation, parameters of links connecting particles with different materials are averaged. The newly implemented algorithm sets parameters of interfacial links based on the matrix material, with further possibility of stiffness, strength and characteristic length modification.

Numerical studies of other authors [6, 49, 50, 53, 41, 43, 40, 77, 78, 87, 95, 98, 109] consider the interface less stiff and weaker than matrix, see figure 8.3. This phenomenon is also supported experimentally [95].

For computational reasons, spherical DEM particles with uniform size are used as discrete elements. The concept of interaction ratio is used in the beginning of the simulation to create cohesive links between mortar-mortar, aggregate-aggregate and mortar-aggregate particles, the latter representing ITZ.

8.2 Model validation

To validate the model for mesoscale concrete, the model should use one set of parameters and should be compared with a set of experiments. The experimental data of mechanical properties dependent on different aggregate grading curves were chosen for this purpose.

In the literature, there are some studies on this topic, but not all of them suit our purpose. Some investigate different grading curves, but the aggregates are artificially made, with lower stiffness and strength than the matrix [29]. Some studies investigate concrete containing a single spherical steel aggregate [3, 2, 1]. Others have incomplete input data (e.g, the experiment was intended for a different purpose than we want) [37, 38].

The papers are useful anyway providing references to other articles and also summarizing literature research. Figure 8.4 shows increasing fracture energy for increasing maximum aggregate size [13]. Figure 8.5 shows influence of maximum aggregate size on

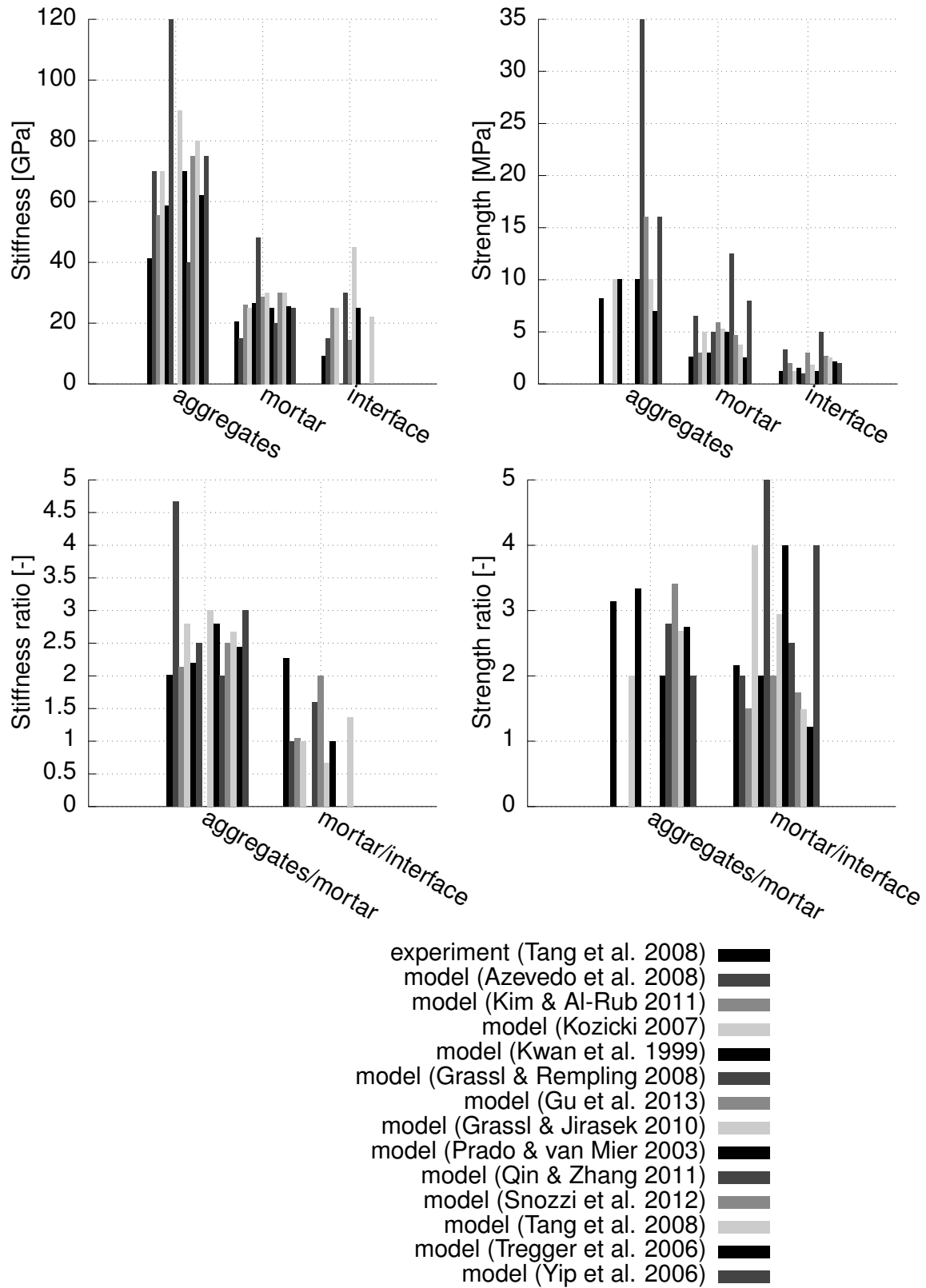


Figure 8.3: ITZ models in literature [6, 49, 50, 53, 41, 43, 40, 77, 78, 87, 95, 98, 109]

various concrete mechanical properties [29]. Black arrows indicate increase, gray dashed arrows decrease and thick gray lines approximately no change. For increasing maximum aggregate size, fracture energy G_f always increased, but for other quantities (f_t and E), the trend is not so indubitable.

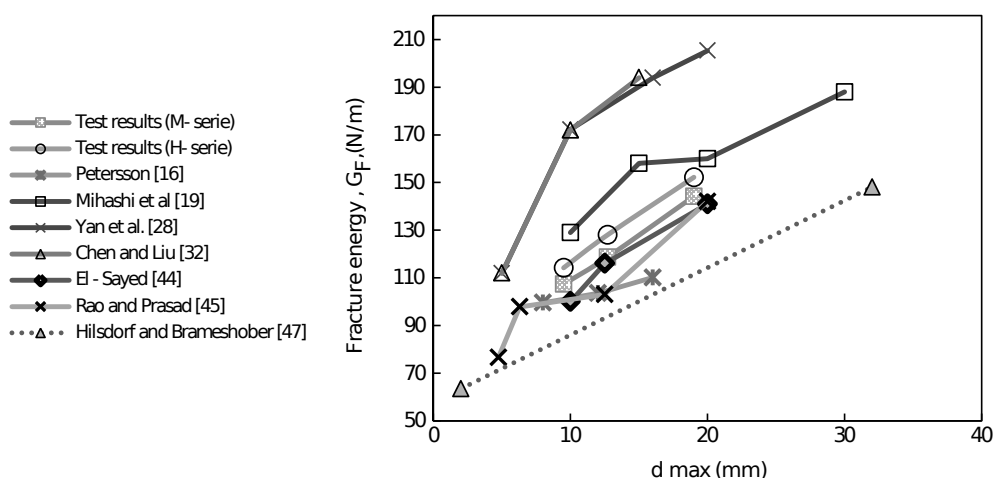


Figure 8.4: Influence of maximum aggregate size on fracture energy [13]

Table 8.1: Cement and water content for concrete compositions [kg/m^3] (top) and grading curves [kg/m^3] (bottom). The first row of the lower table refers to maximum aggregate size

	c	w
low strength	325.8	187.0
high strength	422.4	160.7

	9.5 mm	12.5 mm	19.0 mm
limestone powder	205	205	205
sand	917	917	917
4.75 - 9.5 mm	750	300	300
9.5 - 12.5 mm	-	450	300
12.5 - 19.0 mm	-	-	150

8.2.1 Experiment [12, 13, 69]

From the studied literature, the experiment from [12, 13, 69] was chosen. The experiments investigate the influence of different aggregate sizes (different grading curves) on concrete material properties (f_t , f_c , G_f , E). Two concrete compositions (low strength and high strength) are examined, each with three different aggregate grading curves, see tables 8.1.

Figures 8.6 show the comparison between simulations and experimental data. Since the absolute values of macroscopic quantities can be relatively easily estimated (see section 2.5.3), only values relative to the results for the smallest aggregate size are plotted.

Reference	w/c	%Aggr	Size (mm)	G_F (J/m ²)	E (GPa)	f_t (MPa)
Saouma et al. [6]	0.55	0.44	↓ 19 (max)	↓ 173	↑ 18.0	↑ 2.81
	0.55	0.54	↓ 38 (max)	↓ 223	↑ 16.9	↑ 2.67
	0.55	0.62	↓ 76 (max)	↓ 226	↑ 16.5	↑ 2.41
Li et al. [9]	0.50	0.48	↓ 5-40	↓ 420	↓ 24.6	↑ 1.80
	0.50	0.69	↓ 5-150	↓ 490	↓ 43.1	↑ 1.58
Tasdemir et al. [7]	a	0.36	↓ 5-10	↓ 106	↑ 38	↑ 4.58
	a	0.36	↓ 10-20	↓ 142	↑ 37.2	↑ 3.45
	b	0.36	↓ 5-10	↓ 87	↑ 37.5	↑ 5.42
	b	0.36	↓ 10-20	↓ 87	↑ 37	↑ 4.03
Petersson [2]	0.5	0.5	↓ 8 (max)	↓ 85	↑ 43.2	↑ 4
	0.5	0.5	↓ 12 (max)	↓ 88	↑ 42	↑ 3.8
	0.5	0.5	↓ 16 (max)	↓ 96	↑ 41.9	↑ 3.5
Mihashi et al. [4,5]	-	-	Mortar	105		↑ 3.5
	0.40	0.44	5-10	129		↑ 3.2
	0.40	0.44	10-15	158		↑ 3
	0.40	0.44	15-20	160		↑ 3.4
	0.40	0.44	↓ 20-30	↓ 188		↑ 3.6
Rao and Prasad [8]	a	0.32	↓ 4.75 (max)	↓ 77	↓ 37	↓ 2.39
	a	0.32	↓ 6.3 (max)	↓ 98	↓ 39	↓ 2.7
	a	0.32	↓ 12.5 (max)	↓ 103	↓ 40	↓ 2.9
	a	0.32	↓ 20.0 (max)	↓ 142	↓ 42	↓ 3.06
	b	0.32	↓ 4.75 (max)	↓ 122	↓ 39	↓ 2.55
	b	0.32	↓ 6.3 (max)	↓ 137	↓ 40	↓ 3.31
	b	0.32	↓ 12.5 (max)	↓ 151	↓ 42	↓ 4.01
	b	0.32	↓ 20.0 (max)	↓ 165	↓ 43	↓ 3.8
Chen and Liu [10]	-	-	Mortar	110		↓ 2.04 ^a
	0.37	0.42	↓ 5-10	↓ 175		↓ 2.61 ^a
	0.37	0.42	↓ 10-16	↓ 195		↓ 2.67 ^a
	0.37	0.42	↓ 16-20	↓ 240		↓ 2.58 ^a
Kleinschrodt and Winkler [3]			↓ 8 (max)	↓ 122.3	↓ 25.3	
			↓ 16 (max)	↓ 152.9	↓ 26.9	
Zhang et al. [11]			↓ 7.5	↓ 153	↑ 30	↑ 4.44
			↓ 13	↓ 202	↑ 30	↑ 3.57
			↓ 18	↓ 202	↑ 30	↑ 2.14
			↓ 22.5	↓ 208	↑ 30	↑ 2.46
			↓ 7.5	↓ 180	↑ 35	↑ 4.95
			↓ 13	↓ 182	↑ 35	↑ 4.74
			↓ 18	↓ 199	↑ 35	↑ 4.73
			↓ 22.5	↓ 227	↑ 35	↑ 3.48

Figure 8.5: Influence of maximum aggregate size on mechanical properties [29]

Each point in the graphs is the averaged simulation result from 3 runs. For each run, the same aggregate sizes were considered (according to the corresponding concrete composition and grading curve) and their positions were chosen randomly. The simulations were performed on 50 mm cubic samples with 2 mm DEM particle size (diameter). If particles should be considered as mortar or aggregate particles (and consequently identifying ITZ links) was determined according to figure 8.1

Several combinations of input parameters were tested. The results are plotted for aggregates 2.5 time stiffer and 5 time stronger than matrix and for ITZ 2 times less stiff and 2 times weaker than mortar links. Results 2 refer to 2 times more brittle ITZ than results 1.

The model results reasonably correspond to the trends observed in the experiments, although the precise values are fitted with a certain discrepancy.

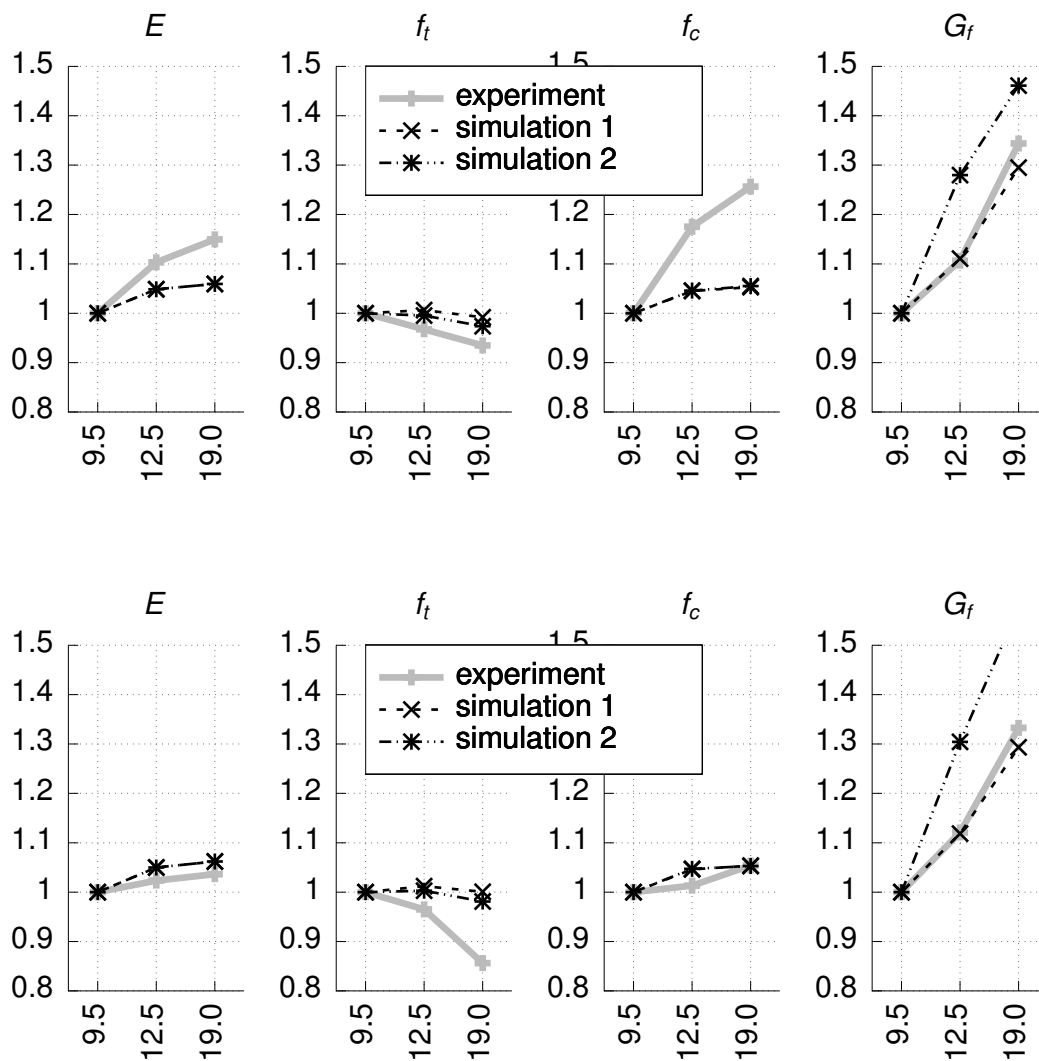


Figure 8.6: Comparison of simulations and experiment [12, 13, 69] for low strength (top) and high strength (bottom) concrete.

Part IV.

Conclusions

9 Conclusions

The following research objectives were accomplished in the present thesis:

- The relation between micro- and macroscopic elastic parameters was investigated both analytically and numerically. The analytical formulas were derived based on the microplane theory. The numerical results were obtained by DEM and FEM simulations. Very good correspondence of the numerical and analytical results is found for packings with interaction ratio greater than 1.25. For lower values of the interaction ratio, the analytical estimation of Young's modulus and Poisson's ratio based on the assumption of uniform distribution of directions of links differs from the numerical results. However, the analytical formula for the full stiffness tensor corresponds to the numerical results very well for all tested values of the interaction ratio.
- The derivation of the stress tensor and couple stress tensor based on the virtual work principle was reviewed and new formulas for the couple stress tensor were proposed and discussed. For the defined volume, the new formulas yield a unique value of the couple stress tensor independent of the choice of the coordinate reference point, which (according to the author's knowledge) has not yet been published in the literature.
- Various classes of FEM–DEM concurrent coupling strategies (namely the surface, direct volume, multiscale and contact coupling) were described. Existing software packages OOFEM and YADE (both providing Python user interface) were chosen for the coupling. Each strategy was illustrated on a simple example. The examples together with the unifying framework form a new open source code project.
- A mapping of the final state of a DEM simulation onto the initial state of the FEM simulation (also referred to as a sequential coupling) was illustrated on uniaxial compression of a concrete material. The method was proven to be able to capture the transition from DEM to FEM relatively well for several different loading scenarios – mapping at different stages (elastic range, peak load, softening regime, with or without unloading etc.). The most divergent results were obtained for the stages of loading where the DEM and FEM material models themselves differed the most.
- A new discrete element model for concrete taking into account the heterogeneous mesoscale structure of concrete (i.e., aggregates and ITZ between aggregates and matrix) was proposed and tested. The validation against experimental data from the literature shows the ability of the model to realistically capture trends of various material properties (elastic modulus, tensile and compressive strength, fracture energy) with respect to the actual mesoscale structure of the material.

References

- [1] T. Akçaoğlu, M. Tokyay, and T. Çelik. Assessing the ITZ microcracking via scanning electron microscope and its effect on the failure behavior of concrete. *Cement and Concrete Research* 35 (2005), pp. 358–363.
- [2] T. Akçaoğlu, M. Tokyay, and T. Çelik. Effect of coarse aggregate size and matrix quality on ITZ and failure behavior of concrete under uniaxial compression. *Cement & Concrete Composites* 26 (2004), pp. 633–638.
- [3] T. Akçaoğlu, M. Tokyay, and T. Çelik. Effect of coarse aggregate size on interfacial cracking under uniaxial compression. *Materials Letters* 57 (2002), pp. 828–833.
- [4] F. Alonso-Marroquin. Static equations of the Cosserat continuum derived from intra-granular stresses. *Granular matter* 13 (2011), pp. 189–196.
- [5] N. M. Azevedo and J. V. Lemos. Hybrid discrete element/finite element method for fracture analysis. *Computer Methods in Applied Mechanics and Engineering* 195 (2006), pp. 4579–4593.
- [6] N. M. Azevedo, J. Lemos, and J. R. de Almeida. Influence of aggregate deformation and contact behaviour on discrete particle modelling of fracture of concrete. *Engineering Fracture Mechanics* 75 (2008), pp. 1569–1586.
- [7] K. Bagi. Discussion on “The asymmetry of stress in granular media”. *International Journal of Solids and Structures* 40 (2003), pp. 1329–1331.
- [8] K. Bagi. Stress and strain in granular assemblies. *Mechanics of Materials* 22 (1996), pp. 165–177.
- [9] J.-P. Bardet and I. Vardoulakis. Reply to discussion by Dr. Katalin Bagi. *International Journal of Solids and Structures* 40 (2003), p. 1035.
- [10] J.-P. Bardet and I. Vardoulakis. Reply to Dr. Kuhn’s discussion. *International Journal of Solids and Structures* 40 (2003), p. 1809.
- [11] J.-P. Bardet and I. Vardoulakis. The asymmetry of stress in granular media. *International Journal of Solids and Structures* 38.2 (2001), pp. 353–367.
- [12] M. H. A. Beygi, M. T. Kazemi, J. V. Amiri, I. M. Nikbin, S. Rabbanifar, and E. Rahmani. Evaluation of the effect of maximum aggregate size on fracture behavior of self compacting concrete. *Construction and Building Materials* 55 (2014), pp. 202–211.
- [13] M. H. A. Beygi, M. T. Kazemi, I. M. Nikbin, J. V. Amiri, S. Rabbanifar, and E. Rahmani. The influence of coarse aggregate size and volume on the fracture behavior and brittleness of self-compacting concrete. *Cement and Concrete Research* 66 (2014), pp. 75–90.
- [14] O. Buyukozturk and B. Hearing. Crack Propagation in Concrete Composites Influenced by Interface Fracture Parameters. *International Journal of Solids and Structures* 35.31–23 (1998), pp. 4055–4066.
- [15] A. Caballero, K. Willam, and I. Carol. Consistent tangent formulation for 3D interface modeling of cracking/fracture in quasi-brittle materials. *Computer Methods in Applied Mechanics and Engineering* 197 (2008), pp. 2804–2822.

- [16] F. Camborde, C. Mariotti, and F. Donzé. Numerical study of rock and concrete behaviour by discrete element modelling. *Computers and Geotechnics* 27 (2000), pp. 225–247.
- [17] C. S. Chang and M. R. Kuhn. On virtual work and stress in granular media. *International Journal of Solids and Structures* 42 (2005), pp. 3773–3793.
- [18] N. Cho, C. Martin, and D. Segol. A clumped particle model for rock. *International Journal of Rock Mechanics & Mining Sciences* 44 (2007), pp. 997–1010.
- [19] I. Comby-Peyrot, F. Bernard, P.-O. Bouchard, F. Bay, and E. Garcia-Diaz. Development and validation of a 3D computational tool to describe concrete behaviour at mesoscale. Application to the alkali-silica reaction. *Computational Materials Science* 46 (2009), pp. 1163–1177.
- [20] E. Cosserat and F. Cosserat. Sur la théorie de l'élasticité. Premier mémoire. *Annales de la Faculté des sciences de Toulouse : Mathématiques* 10.3-4 (1896), pp. 11–116.
- [21] P. A. Cundall and O. D. L. Strack. A Discrete Numerical Model for Granular Assemblies. *Géotechnique* 29.1 (1979), pp. 47–65.
- [22] G. Cusatis. "Tridimensional random particle model for concrete". PhD thesis. Polytechnic University of Milan, 2001.
- [23] G. Cusatis, Z. P. Bažant, and L. Cedolin. Confinement-shear lattice CSL model for fracture propagation in concrete. *Computer Methods in Applied Mechanics and Engineering* 195 (2006), pp. 7154–7171.
- [24] G. Cusatis, A. Mencarelli, D. Pelessone, and J. Baylot. Lattice Discrete Particle Model (LDPM) for failure behavior of concrete. II: Calibration and validation. *Cement & Concrete Composites* 33 (2011), pp. 891–905.
- [25] G. Cusatis, D. Pelessone, and A. Mencarelli. Lattice Discrete Particle Model (LDPM) for failure behavior of concrete. I: Theory. *Cement & Concrete Composites* 33 (2011), pp. 881–890.
- [26] J. B. D. Asahina a E.N. Landis b. Modeling of phase interfaces during pre-critical crack growth in concrete. *Cement & Concrete Composites* 33 (2011), pp. 966–977.
- [27] 3. E N Landis¹ and J. E. Bolander. Explicit representation of physical processes in concrete fracture. *Journal of Physics D: Applied Physics* 42.21 (2009).
- [28] W. Ehlers and W. Volk. Localization Phenomena in Liquid-Saturated and Empty Porous Solids. *Transport in Porous Media* 34 (1999), pp. 159–177.
- [29] M. Elices and G. G. Rocco. Effect of aggregate size on the fracture and mechanical properties of a simple concrete. *Engineering Fracture Mechanics* 75 (2008), pp. 3839–3851.
- [30] S. Erdem, A. R. Dawson, and N. H. Thom. Influence of the micro- and nanoscale local mechanical properties of the interfacial transition zone on impact behavior of concrete made with different aggregates. *Cement and Concrete Research* 42 (2012), pp. 447–458.
- [31] C. Ergenzinger, R. Seifried, and P. Eberhard. A discrete element model predicting the strength of ballast stones. *Computers and Structures* 108–109 (2012), pp. 3–13.

-
- [32] A. Fakhimi. A hybrid discrete–finite element model for numerical simulation of geomaterials. *Computers and Geotechnics* 36 (2009), pp. 386–395.
- [33] G. Frenning. An efficient finite/discrete element procedure for simulating compression of 3D particle assemblies. *Computer Methods in Applied Mechanics and Engineering* 197 (2008), pp. 4266–4272.
- [34] E. Garboczi. Three-dimensional mathematical analysis of particle shape using X-ray tomography and spherical harmonics: Application to aggregates used in concrete. *Cement and Concrete Research* 32 (2002), pp. 1621–1638.
- [35] M. G. D. Geers, V. G. Kouznetsova, and W. A. M. Brekelmans. Multi-scale computational homogenization: Trends and challenges. *Journal of Computational and Applied Mathematics* 234 (2010), pp. 2175–2182.
- [36] A. Ghosh and P. Chaudhuri. Computational modeling of fracture in concrete using a meshfree meso-macro-multiscale method. *Computational Materials Science* 69 (2013), pp. 204–215.
- [37] G. Giaccio and R. Zerbino. Failure Mechanism of Concrete. Combined Effects of Coarse Aggregates and Strength Level. *Advanced Cement Based Materials* 7 (1998), pp. 14–48.
- [38] G. Giaccio, R. Zerbino, J. M. Ponce, and O. R. Batic. Mechanical behavior of concretes damaged by alkali-silica reaction. *Cement and Concrete Research* 38 (2008), pp. 993–1004.
- [39] P. Grassl and M. Jirásek. Damage-plastic model for concrete failure. *International Journal of Solids and Structures* 43 (2006), pp. 7166–7196.
- [40] P. Grassl and M. Jirásek. Meso-scale approach to modelling the fracture process zone of concrete subjected to uniaxial tension. *International Journal of Solids and Structures* 47 (2010), pp. 957–968.
- [41] P. Grassl and R. Rempling. A damage-plasticity interface approach to the meso-scale modelling of concrete subjected to cyclic compressive loading. *Engineering Fracture Mechanics* 75 (2008), pp. 4804–4818.
- [42] U. Groh, H. Konietzky, K. Walter, and M. Herbst. Damage simulation of brittle heterogeneous materials at the grain size level. *Theoretical and Applied Fracture Mechanics* 55 (2011), pp. 31–38.
- [43] X. Gu, L. Hong, Z. Wang, and F. Lin. A modified rigid-body-spring concrete model for prediction of initial defects and aggregates distribution effect on behavior of concrete. *Computational Materials Science* 77 (2013), pp. 355–365.
- [44] S. Häfner, S. Eckardt, T. Luther, and C. Könke. Mesoscale modeling of concrete: Geometry and numerics. *Computers and Structures* 84 (2006), pp. 450–461.
- [45] S. Hentz, F. V. Donzé, and L. Daudeville. Discrete element modelling of concrete submitted to dynamic loading at high strain rates. *Computers and Structures* 82 (2004), pp. 2509–2524.
- [46] H. Huang, B. Lecampion, and E. Detournay. Discrete element modeling of tool-rock interaction I: rock cutting. *International Journal for Numerical and Analytical Methods in Geomechanics* 37 (2013), pp. 1913–1929.

-
- [47] A. Ibrahimbegovic and A. Delaplace. Microscale and mesoscale discrete models for dynamic fracture of structures built of brittle material. *Computers and Structures* 81 (2003), pp. 1255–1265.
- [48] J.-F. Jerier, V. Richefeu, D. Imbault, and F.-V. Donzé. Packing spherical discrete elements for large scale simulations. *Computer Methods in Applied Mechanics and Engineering* 199 (2010), pp. 1668–1676.
- [49] S.-M. Kim and R. K. A. Al-Rub. Meso-scale computational modeling of the plastic-damage response of cementitious composites. *Cement and Concrete Research* 41 (2011), pp. 339–358.
- [50] J. Kozicky. “Application of Discrete Models to Describe the Fracture Process in Brittle Materials”. PhD thesis. Gdańsk University of Technology, 2007.
- [51] E. Kuhl, G. A. D’Addetta, M. Leukart, and E. Ramm. “Microplane modelling and particle modelling of cohesive-frictional materials”. In: *Continuous and Discontinuous Modelling of Cohesive-Frictional Materials*. Vol. 568. Lecture Notes in Physics. Springer Berlin / Heidelberg, 2001, pp. 31–46.
- [52] M. R. Kuhn. Discussion on “The asymmetry of stress in granular media”. *International Journal of Solids and Structures* 40 (2003), pp. 1805–1807.
- [53] A. Kwan, Z. Wang, and H. Chan. Mesoscopic study of concrete II: nonlinear Finite element analysis. *Computers and Structures* 70 (1999), pp. 545–556.
- [54] C. Lambert and O. B. and A. Giacomini. Influence of calcium leaching on the mechanical behavior of a rock–mortar interface: A DEM analysis. *Computers and Geotechnics* 37 (2010), pp. 258–266.
- [55] J. Leite, V. Slowik, and J. Apel. Computational model of mesoscopic structure of concrete for simulation of fracture processes. *Computers and Structures* 85 (2007), pp. 1239–1303.
- [56] J. Leite, V. Slowik, and H. Mihashi. Computer simulation of fracture processes of concrete using mesolevel models of lattice structures. *Cement and Concrete Research* 34 (2004), pp. 1025–1033.
- [57] J. Liu, C. Zhao, and B. Yun. Numerical study on explosion-induced fractures of reinforced concrete structure by beam-particle model. *Science China Technological Sciences* 54 (2011), pp. 412–419.
- [58] A. E. H. Love. *A Treatise on the Mathematical Theory of Elasticity (4th ed.)* Cambridge, University press, 1927.
- [59] F.-V. D. Luc Scholtées a. Modelling progressive failure in fractured rock masses using a 3D discrete element method. *International Journal of Rock Mechanics & Mining Sciences* 52 (2012), pp. 18–30.
- [60] G. Ma, X. Wang, and F. Ren. Numerical simulation of compressive failure of heterogeneous rock-like materials using SPH method. *International Journal of Rock Mechanics & Mining Sciences* 48 (2011), pp. 353–363.
- [61] S. A. Magnier and F. V. Donzé. Numerical simulations of impacts using a discrete element method. *Mechanics of Cohesive-frictional Materials* 3 (1998), pp. 257–276.
- [62] P. Marangi. “Computational modeling of fiber reinforced concrete with application to projectile penetration”. PhD thesis. University of Bologna, 2010.

-
- [63] M. Mungule and B. K. Raghuprasad. Meso-scale studies in fracture of concrete: A numerical simulation. *Computers and Structures* 89 (2011), pp. 912–920.
- [64] A. Munjiza. *The combined finite-discrete element method*. Wiley, Chichester, 2004.
- [65] A. A. Munjiza and K. R. F. Andrews. NBS contact detection algorithm for bodies of similar size. *International Journal for Numerical Methods in Engineering* 43 (1998), pp. 131–149.
- [66] H. Nakashima and A. Oida. Algorithm and implementation of soil–tire contact analysis code based on dynamic FE–DE method. *Journal of Terramechanics* 41 (2004), pp. 127–137.
- [67] A. Nardin and B. A. Schrefler. Numerical simulation of rock behaviour through a discrete model. *International Journal of Solids and Structures* 41 (2004), pp. 5945–5965.
- [68] C. M. Neubauer, H. M. Lennings, and E. J. Garboczi. A Three-Phase Model of the Elastic and Shrinkage Properties of Mortar. *Advanced Cement Based Materials* 4 (1996), pp. 6–20.
- [69] I. M. Nikbin, M. H. A. Beygi, M. T. Kazemi, J. V. Amiri, E. Rahmani, S. Rabbanifar, and M. Eslami. A comprehensive investigation into the effect of aging and coarse aggregate size and volume on mechanical properties of self-compacting concrete. *Materials and Design* 59 (2014), pp. 199–210.
- [70] E. Onate and J. Rojek. Combination of discrete element and finite element methods for dynamic analysis of geomechanics problems. *Computer Methods in Applied Mechanics and Engineering* 139 (2004), pp. 3087–3128.
- [71] J. Ožbolt and A. Sharma. Numerical simulation of dynamic fracture of concrete through uniaxial tension and L-specimen. *Engineering Fracture Mechanics* 85 (2012), pp. 88–102.
- [72] J. Pan, Y. T. Feng, F. Jin, Y. Xu, Q. Sun, C. Zhang, and D. R. J. Owen. Meso-scale particle modeling of concrete deterioration caused by alkali-aggregate reaction. *International Journal for Numerical and Analytical Methods in Geomechanics* 37 (2013), pp. 2690–2705.
- [73] B. Patzák. *OOFEM project home page*. 2018. URL: <http://www.oofem.org>.
- [74] B. Patzák and Z. Bittnar. Design of object oriented finite element code. *Advances in Engineering Software* 32.10–11 (2001), pp. 759–767.
- [75] R. Pedersen, A. Simone, and L. Sluys. Mesoscopic modeling and simulation of the dynamic tensile behavior of concrete. *Cement and Concrete Research* 50 (2013), pp. 74–87.
- [76] D. Potyondya and P. Cundall. A bonded-particle model for rock. *International Journal of Rock Mechanics & Mining Sciences* 41 (2004), pp. 1329–1364.
- [77] E. Prado and J. van Mier. Effect of particle structure on mode I fracture process in concrete. *Engineering Fracture Mechanics* 70 (2003), pp. 1793–1807.
- [78] C. Qin and C. Zhang. Numerical study of dynamic behavior of concrete by meso-scale particle element modeling. *International Journal of Impact Engineering* 38 (2011), pp. 1011–1021.

- [79] G. A. Rao and B. R. Prasad. Influence of the roughness of aggregate surface on the interface bond strength. *Cement and Concrete Research* 32 (2002), pp. 253–257.
- [80] J. Rojek and E. Onate. Multiscale analysis using a coupled discrete/finite element model. *Interaction and Multiscale Mechanics* 1 (2007), pp. 1–31.
- [81] J. Rojek, E. Onñate, C. Labra, and H. Kargl. Discrete element simulation of rock cutting. *International Journal of Rock Mechanics & Mining Sciences* 48 (2011), pp. 996–1010.
- [82] J. Rousseau, E. Frangin, P. Marin, and L. Daudville. Multidomain finite and discrete elements method for impact analysis of a concrete structure. *Engineering Structures* 31 (2009), pp. 2735–2743.
- [83] D. Rypl. Using the spherical harmonic analysis and the advancing front technique for the discretization of 3D aggregate particles. *Advances in Engineering Software* 41 (2010), pp. 38–45.
- [84] A. Satoh, K. Yamada, and S. Ishiyama. Simplified two-dimensional mesoscopic model for evaluating mechanical properties and crack paths near interfaces in concrete. *Engineering Fracture Mechanics* 4 (2013), pp. 6–20.
- [85] L. Scholtés and F.-V. Donzé. A DEM model for soft and hard rocks: Role of grain interlocking on strength. *Journal of the Mechanics and Physics of Solids* 61 (2013), pp. 352–369.
- [86] S. Shahbeyk, M. Hosseini, and M. Yaghoobi. Mesoscale finite element prediction of concrete failure. *Computational Materials Science* 50 (2011), pp. 1973–1990.
- [87] L. Snozzi, F. Gatuingt, and J. F. Molinari. A meso-mechanical model for concrete under dynamic tensile and compressive loading. *International Journal of Fracture* 178 (2012), pp. 179–194.
- [88] J. Stránský and M. Jirásek. “Calibration of Particle Models using Cells with Periodic Boundary Conditions”. In: *Particles 2011*. Barcelona, Spain, 2011.
- [89] J. Stránský and M. Jirásek. “Calibration of particle-based models using cells with periodic boundary conditions”. In: *Particle-based Methods II - Fundamentals and Applications*. Ed. by E. Oñate and D. R. J. Owen. Barcelona, Spain: CIMNE, 2011, pp. 274–285.
- [90] V. Šmilauer, E. Catalano, B. Chareyre, S. Dorofeenko, J. Duriez, A. Gladky, J. Kozicki, C. Modenese, L. Scholtès, L. Sibille, J. Stránský, and K. Thoeni. In: *Yade Documentation 2nd ed.* Ed. by V. Šmilauer. <http://yade-dem.org/doc/>. The Yade Project, 2010.
- [91] V. Šmilauer, E. Catalano, B. Chareyre, S. Dorofeenko, J. Duriez, N. Dyck, J. Eliáš, B. Er, A. Eulitz, A. Gladky, C. Jakob, F. Kneib, J. Kozicki, D. Marzougui, R. Maurin, C. Modenese, L. Scholtès, L. Sibille, J. Stránský, T. Sweijen, K. Thoeni, and C. Yuan. “Reference Manual”. In: *Yade Documentation 2nd ed.* <http://yade-dem.org/doc/>. The Yade Project, 2015. DOI: 10.5281/zenodo.34045.
- [92] V. Šmilauer. “Cohesive particle model using the discrete element method on the Yade platform”. PhD thesis. Czech Technical University in Prague, 2010.
- [93] V. Šmilauer. *YADE project home page*. 2018. URL: <http://www.yade-dem.org>.

-
- [94] C. Tang, X. Xua, S. Kouc, P.-A. Lindqvistc, and H. Liu. Numerical investigation of particle breakage as applied to mechanical crushing—Part I: Single-particle breakage. *International Journal of Rock Mechanics & Mining Sciences* 38 (2001), pp. 1147–1162.
- [95] X. W. Tang, C. H. Zhang, and J. J. Shi. A multiphase mesostructure mechanics approach to the study of the fracture-damage behavior of concrete. *Science in China Series E: Technological Sciences* 51 (2008), pp. 8–24.
- [96] S. Torquato, T. M. Truskett, and P. G. Debenedetti. Is random close packing of spheres well defined? *Physical Review Letters* 84.10 (2000), pp. 2064–2067.
- [97] V. T. Tran, F. V. Donzé, and P. Marin. A discrete element model of concrete under high triaxial loading. *Cement & Concrete Composites* 33 (2011), pp. 936–948.
- [98] N. Tregger, D. Corr, L. Graham-Brady, and S. Shah. Modeling the effect of mesoscale randomness on concrete fracture. *Probabilistic Engineering Mechanics* 21 (2006), pp. 217–225.
- [99] B. Valentini and G. Hofstetter. Review and enhancement of 3D concrete models for large-scale numerical simulations of concrete structures. *International Journal for Numerical and Analytical Methods in Geomechanics* 37.3 (2013), pp. 221–246.
- [100] I. Vardoulakis. *Lecture notes on Cosserat continuum mechanics with application to the mechanics of granular media*. 3rd National Meeting on “Generalized Continuum Theories and Applications” Thessaloniki. Jan. 2009. URL: <http://geolab.mechan.ntua.gr/teaching/lectnotes/CCM2009.pdf>.
- [101] P. Villard, B. Chevalier, B. L. Hello, and G. Combe. Coupling between finite and discrete element methods for the modelling of earth structures reinforced by geosynthetic. *Computers and Geotechnics* 36 (2009), pp. 709–717.
- [102] Y. Wang and F. Tonon. Modeling Lac du Bonnet granite using a discrete element model. *International Journal of Rock Mechanics & Mining Sciences* 46 (2009), pp. 1124–1135.
- [103] Z. Wang, F. Lin, and X. Gu. Numerical Simulation of Failure Process of Concrete Under Compression Based on Mesoscopic Discrete Element Model. *Tsinghua Science And Technology* 13.S1 (2008), pp. 19–25.
- [104] Z. Wang, A. Kwan, and H. Chan. Mesoscopic study of concrete I: generation of random aggregate structure and finite element mesh. *Computers and Structures* 70 (1999), pp. 533–544.
- [105] C. Wellmann and P. Wriggers. A two-scale model of granular materials. *Computer Methods in Applied Mechanics and Engineering* 205–208 (2012), pp. 46–58.
- [106] P. Wriggers and S. Moftah. Mesoscale models for concrete: Homogenisation and damage behaviour. *Finite Elements in Analysis and Design* 42 (2006), pp. 623–636.
- [107] M. Xu, R. Gracie, and T. Belytschko. “Bridging the Scales in Science and Engineering”. In: ed. by J. Fish. Oxford University Press, 2002. Chap. Multiscale modeling with extended bridging domain method.
- [108] Z. Xu, H. Hao, and H. Li. Mesoscale modelling of fibre reinforced concrete material under compressive impact loading. *Construction and Building Materials* 26 (2012), pp. 274–288.

- [109] M. Yip, Z. Li, B.-S. Liao, and J. Bolander. Irregular lattice models of fracture of multiphase particulate materials. *International Journal of Fracture* 140 (2006), pp. 113–124.
- [110] X. Zhou and H. Hao. Mesoscale modelling and analysis of damage and fragmentation of concrete slab under contact detonation. *International Journal of Impact Engineering* 36 (2009), pp. 1315–1326.
- [111] X. Zhou and H. Hao. Mesoscale modelling of concrete tensile failure mechanism at high strain rates. *Computers and Structures* 86 (2008), pp. 2013–2026.
- [112] X. Zhou and H. Hao. Modelling of compressive behaviour of concrete-like materials at high strain rate. *International Journal of Solids and Structures* 45 (2008), pp. 4648–4661.
- [113] W. Zhu and C. Tang. Numerical simulation on shear fracture process of concrete using mesoscopic mechanical model. *Construction and Building Materials* 16 (2002), pp. 453–463.

Part V.

Appendices

A Mathematical and physical concepts and notations

Because the reader may be used to a different notation or terminology, “generally known” mathematical and physical theory is summarized in this chapter.

Some identities and equations of this chapter are referenced multiple times from the core part of the thesis, which was another motivation to create this appendix.

This chapter also contains some “generally known” derivations or derivations which themselves are not so important for the results provided by this thesis, but which are, according to the author’s opinion, worth to be mentioned.

A.1 Tensors

Both index notation

$$a, a_i, A_{ij}, A_{ijk}, A_{ijkl} \quad (\text{A.1})$$

and symbolic notation

$$a, \mathbf{a}, \mathbf{A}, \mathcal{A}, \mathbb{A} \quad (\text{A.2})$$

are used in this thesis. The two lines of symbols above show notation for a zero (scalar), first (vector), second, third and fourth order tensor, respectively. The notations are interchangeable, but there are situations, where one is preferable to the other.

The so called Einstein summation rule is used for index notation, for instance

$$A_{il} = A_{ij} C_{jk} D_{mmkl} \equiv \sum_j \sum_k \sum_m A_{ij} C_{jk} D_{mmkl}. \quad (\text{A.3})$$

This thesis works with Cartesian coordinate system, so there is no need to distinguish between covariant, contravariant or mixed tensors.

A.1.1 Algebraic operations and properties

The following algebraic operations, written usually in both index and symbolic notation, are used throughout the thesis. Some symbols (e.g., \mathcal{E} , $\mathbf{1}$ or \mathbb{I}) are defined in the next section A.1.2.

A.1.1.1 Contraction

$$a = \mathbf{b} \cdot \mathbf{c}, \quad a = b_i c_i \quad (\text{A.4})$$

$$\mathbf{a} = \mathbf{B} \cdot \mathbf{c}, \quad a_i = B_{ij} c_j \quad (\text{A.5})$$

$$\mathbf{a} = \mathbf{b} \cdot \mathbf{C}, \quad a_i = b_j C_{ji} \quad (\text{A.6})$$

$$\mathbf{A} = \mathbf{B} \cdot \mathbf{C}, \quad A_{ij} = B_{ik} C_{kj} \quad (\text{A.7})$$

$$\mathbf{A} = \mathbf{b} \overset{m}{\cdot} \mathbf{C} \quad A_{ij} = b_k C_{ikj} \quad (\text{A.8})$$

$$\mathbf{A} = \mathcal{B} \cdot \mathbf{c} \quad A_{ij} = B_{ijk} c_k \quad (\text{A.9})$$

$$\mathbb{A} = \mathcal{B} \cdot \mathcal{C} \quad A_{ijkl} = B_{ijm} C_{mkl} \quad (\text{A.10})$$

The operator $\overset{m}{\cdot}$ denotes contraction with respect to the middle index.

A.1.1.2 Double contraction

$$\mathbf{a} = \mathbf{A} : \mathbf{B}, \quad \mathbf{a} = A_{ij} B_{ij} \quad (\text{A.11})$$

$$\mathbf{A} = \mathbb{B} : \mathbf{C}, \quad A_{ij} = B_{ijkl} C_{kl} \quad (\text{A.12})$$

$$\mathbf{A} = \mathbf{B} : \mathbf{C}, \quad A_{ij} = B_{kl} C_{klj} \quad (\text{A.13})$$

$$\mathbf{a} = \mathcal{B} : \mathbf{C}, \quad A_i = B_{ijk} C_{jk} \quad (\text{A.14})$$

$$\mathbf{A} = \mathcal{B} : \mathbf{C}, \quad A_{ij} = B_{ikl} C_{klj} \quad (\text{A.15})$$

$$\mathbf{A} = \mathbb{B} : \mathbf{C}, \quad A_{ijkl} = B_{ijmn} C_{mnkl} \quad (\text{A.16})$$

A.1.1.3 Dyadic (outer, tensor, direct) product

$$\mathbf{A} = \mathbf{a} \otimes \mathbf{b}, \quad A_{ij} = a_i b_j \quad (\text{A.17})$$

$$\mathbf{A} = \mathbf{B} \otimes \mathbf{C} \quad A_{ijkl} = B_{ij} C_{kl} \quad (\text{A.18})$$

A.1.1.4 Cross product

$$\mathbf{c} = \mathbf{a} \times \mathbf{b} = \mathbf{b} \cdot \mathcal{E} \cdot \mathbf{a} = -\mathbf{b} \times \mathbf{a} \quad c_i = \varepsilon_{ijk} a_j b_k = b_k \varepsilon_{kij} a_j = -\varepsilon_{ijk} a_k b_j \quad (\text{A.19})$$

$$\mathbf{C} = \mathbf{1} \times \mathbf{b} = \mathcal{E} \cdot \mathbf{b} \quad C_{ij} = \varepsilon_{ijk} b_k \quad (\text{A.20})$$

$$\mathbf{c} = \mathbf{1} \times \mathbf{B} = \mathcal{E} : \mathbf{B}, \quad c_i = \varepsilon_{ijk} B_{jk} \quad (\text{A.21})$$

$\mathcal{E}, \varepsilon_{ijk}$ is the Levi-Civita permutation symbol (A.39).

A.1.1.5 Transposition of a second order tensor

$$\mathbf{A}^T \quad A_{ij}^T = A_{ji} \quad (\text{A.22})$$

A.1.1.6 Symmetric and antisymmetric second order tensor, axial vector, decomposition

Any symmetric second order tensor \mathbf{S} equals its transposition:

$$\mathbf{S} = \mathbf{S}^T \quad S_{ij} = S_{ji} \quad (\text{A.23})$$

Any antisymmetric second order tensor \mathbf{W} equals minus its transposition:

$$\mathbf{W} = -\mathbf{W}^T \quad W_{ij} = -W_{ji} \quad (\text{A.24})$$

Any antisymmetric second order tensor \mathbf{W} can be expressed in terms of its dual (axial) vector \mathbf{w} such that for any \mathbf{b}

$$\forall \mathbf{b}; \quad \mathbf{b} \cdot \mathbf{W} = \mathbf{w} \times \mathbf{b}, \quad \forall b_i; \quad b_i W_{ij} = \varepsilon_{jki} w_k b_i, \quad (\text{A.25})$$

therefore

$$\mathbf{W} = \mathcal{E} \cdot \mathbf{w} = \mathbf{1} \times \mathbf{w} \quad W_{ij} = \varepsilon_{jki} w_k = \varepsilon_{ijk} w_k \quad \mathbf{W} = \begin{bmatrix} 0 & w_3 & -w_2 \\ -w_3 & 0 & w_1 \\ w_2 & -w_1 & 0 \end{bmatrix} \quad (\text{A.26})$$

$$\mathbf{w} = \frac{1}{2} \mathcal{E} : \mathbf{W} = \frac{1}{2} \mathbf{1} \times \mathbf{W} \quad w_k = \frac{1}{2} \varepsilon_{kij} W_{ij} \quad \mathbf{w} = \{W_{23}, W_{31}, W_{12}\}^T. \quad (\text{A.27})$$

The duality of the last equations can be easily shown using properties of \mathcal{E} and substituting (A.27) into (A.26) or vice versa:

$$\begin{aligned}\mathbf{w} &= \frac{1}{2}\mathcal{E} : \mathbf{W} = \frac{1}{2}\mathcal{E} : \mathcal{E} \cdot \mathbf{w} = \frac{1}{2}2\mathbf{1} \cdot \mathbf{w} = \mathbf{w} \\ w_k &= \frac{1}{2}\varepsilon_{kij}W_{ij} = \frac{1}{2}\varepsilon_{kij}\varepsilon_{ijl}w_l = \frac{1}{2}2\delta_{kl}w_l = w_k\end{aligned}\quad (\text{A.28})$$

$$\begin{aligned}\mathbf{W} &= \mathcal{E} \cdot \mathbf{w} = \frac{1}{2}\mathcal{E} \cdot \mathcal{E} : \mathbf{W} = \frac{1}{2}2\mathbb{I}^A : \mathbf{W} = \mathbf{W} \\ W_{ij} &= \varepsilon_{ijk}w_k = \varepsilon_{ijk}\frac{1}{2}\varepsilon_{klm}W_{lm} = \frac{1}{2}(\delta_{il}\delta_{jm} - \delta_{im}\delta_{jl})W_{lm} = \frac{1}{2}(W_{ij} - W_{ji}) = W_{ij}\end{aligned}\quad (\text{A.29})$$

Any second order tensor can be decomposed into the symmetric and the antisymmetric part.

$$\mathbf{A} = \mathbf{A}^S + \mathbf{A}^A \quad A_{ij} = A_{ij}^S + A_{ij}^A \quad (\text{A.30})$$

$$\mathbf{A}^S = \frac{1}{2}(\mathbf{A} + \mathbf{A}^T) = \mathbb{I}^S : \mathbf{A} \quad A_{ij}^S = \frac{1}{2}(A_{ij} + A_{ji}) = \frac{1}{2}(\delta_{ik}\delta_{jl} + \delta_{il}\delta_{jk})A_{kl} \quad (\text{A.31})$$

$$\mathbf{A}^A = \frac{1}{2}(\mathbf{A} - \mathbf{A}^T) = \mathbb{I}^A : \mathbf{A} \quad A_{ij}^A = \frac{1}{2}(A_{ij} - A_{ji}) = \frac{1}{2}(\delta_{ik}\delta_{jl} - \delta_{il}\delta_{jk})A_{kl} \quad (\text{A.32})$$

A.1.1.7 Trace of a second order tensor

A trace of a second order tensor is the sum of its diagonal elements. The trace is the first invariant of a second order tensor.

$$\text{tr}(\mathbf{A}) = A_{11} + A_{22} + A_{33} \quad (\text{A.33})$$

It can be computed as a double contraction with the second order identity tensor.

$$\text{tr}(\mathbf{A}) = \mathbf{A} : \mathbf{1} = \mathbf{1} : \mathbf{A} \quad \text{tr}(A_{ij}) = A_{ij}\delta_{ij} = \delta_{ij}A_{ij} = A_{ii} = A_{11} + A_{22} + A_{33} \quad (\text{A.34})$$

A.1.1.8 Volumetric part of a second order tensor

A volumetric (hydrostatic, spherical, isotropic) part of a second order tensor is a product of its mean value (one third of its trace) and the second order identity tensor

$$\mathbf{A}^V = \frac{\text{tr}(\mathbf{A})}{3}\mathbf{1} = \frac{1}{3}(\mathbf{A} : \mathbf{1})\mathbf{1} = \frac{1}{3}\mathbf{1} \otimes \mathbf{1} : \mathbf{A} \quad A_{ij}^V = \frac{A_{kk}}{3}\delta_{ij} = \frac{1}{3}\delta_{ij}\delta_{kl}A_{kl} \quad (\text{A.35})$$

Trace of the volumetric part equals trace of the original tensor

$$\text{tr}(\mathbf{A}^V) = \text{tr}\left(\frac{\text{tr}(\mathbf{A})}{3}\mathbf{1}\right) = \frac{\text{tr}(\mathbf{A})}{3}\text{tr}(\mathbf{1}) = \frac{\text{tr}(\mathbf{A})}{3}3 = \text{tr}(\mathbf{A}) \quad (\text{A.36})$$

A.1.2 Special tensor instances and identities

A.1.2.1 Second order identity tensor

A matrix representation of the second order identity tensor is the identity matrix. For the index notation, Kronecker delta is used.

$$\mathbf{1} = \begin{bmatrix} 1 & 0 & 0 \\ 0 & 1 & 0 \\ 0 & 0 & 1 \end{bmatrix} \quad \delta_{ij} = \begin{cases} 1 & \text{if } i = j \\ 0 & \text{if } i \neq j \end{cases} \quad (\text{A.37})$$

$$\forall \mathbf{A}; \quad \mathbf{1} \cdot \mathbf{A} = \mathbf{A} \cdot \mathbf{1} = \mathbf{A} \quad \forall A_{mn}; \quad \delta_{ik} A_{kj} = A_{ik} \delta_{kj} = A_{ij}. \quad (\text{A.38})$$

A.1.2.2 Levi-Civita permutation symbol

$$\mathcal{E} \quad \varepsilon_{ijk} = \begin{cases} +1 & \text{if } (i, j, k) \in \{(1, 2, 3), (2, 3, 1), (3, 1, 2)\} \\ -1 & \text{if } (i, j, k) \in \{(3, 2, 1), (1, 3, 2), (2, 1, 3)\} \\ 0 & \text{if } i = j \text{ or } j = k \text{ or } k = i \end{cases} \quad (\text{A.39})$$

therefore

$$\varepsilon_{ijk} = \varepsilon_{jki} = \varepsilon_{kij} = -\varepsilon_{kji} = -\varepsilon_{ikj} = -\varepsilon_{jik} \quad (\text{A.40})$$

and

$$\mathcal{E} : \mathcal{E} = 2 \mathbf{1} \quad \varepsilon_{ikl} \varepsilon_{klj} = 2 \delta_{ij} \quad (\text{A.41})$$

$$\mathcal{E} \cdot \mathcal{E} = 2 \mathbb{I}^A \quad \varepsilon_{ijm} \varepsilon_{mkl} = \delta_{ik} \delta_{jl} - \delta_{il} \delta_{jk}. \quad (\text{A.42})$$

A.1.2.3 Fourth order identity tensors

$$\mathbb{I} \quad I_{ijkl} = \delta_{ik} \delta_{jl} \quad (\text{A.43})$$

$${}^T \mathbb{I} \quad {}^T I_{ijkl} = \delta_{il} \delta_{jk} \quad (\text{A.44})$$

$$\mathbb{I}^S = \frac{1}{2} (\mathbb{I} + {}^T \mathbb{I}) \quad I_{ijkl}^S = \frac{1}{2} (\delta_{ik} \delta_{jl} + \delta_{il} \delta_{jk}) \quad (\text{A.45})$$

$$\mathbb{I}^A = \frac{1}{2} (\mathbb{I} - {}^T \mathbb{I}) = \frac{1}{2} \mathcal{E} \cdot \mathcal{E} \quad I_{ijkl}^A = \frac{1}{2} (\delta_{ik} \delta_{jl} - \delta_{il} \delta_{jk}) \quad (\text{A.46})$$

with following properties

$$\forall \mathbf{A}; \quad \mathbb{I} : \mathbf{A} = \mathbf{A} : \mathbb{I} = \mathbf{A} \quad \forall A_{mn}; \quad \delta_{ik} \delta_{jl} A_{kl} = A_{ij}, \quad A_{ij} \delta_{ik} \delta_{jl} = A_{kl} \quad (\text{A.47})$$

$$\forall \mathbf{A}; \quad {}^T \mathbb{I} : \mathbf{A} = \mathbf{A} : {}^T \mathbb{I} = \mathbf{A}^T \quad \forall A_{mn}; \quad \delta_{il} \delta_{jk} A_{kl} = A_{ji}, \quad A_{ij} \delta_{il} \delta_{jk} = A_{lk} \quad (\text{A.48})$$

$$\forall \mathbf{A}; \quad \mathbb{I}^S : \mathbf{A} = \frac{1}{2} (\mathbb{I} + {}^T \mathbb{I}) : \mathbf{A} = \frac{1}{2} (\mathbf{A} + \mathbf{A}^T) = \mathbf{A}^S \quad (\text{A.49})$$

$$\forall \mathbf{A}; \quad \mathbf{A} : \mathbb{I}^S = \mathbf{A} : \frac{1}{2} (\mathbb{I} + {}^T \mathbb{I}) = \frac{1}{2} (\mathbf{A} + \mathbf{A}^T) = \mathbf{A}^S$$

$$\forall \mathbf{A}; \quad \mathbb{I}^A : \mathbf{A} = \frac{1}{2} (\mathbb{I} - {}^T \mathbb{I}) : \mathbf{A} = \frac{1}{2} (\mathbf{A} - \mathbf{A}^T) = \mathbf{A}^A \quad (\text{A.50})$$

$$\forall \mathbf{A}; \quad \mathbf{A} : \mathbb{I}^A = \mathbf{A} : \frac{1}{2} (\mathbb{I} - {}^T \mathbb{I}) = \frac{1}{2} (\mathbf{A} - \mathbf{A}^T) = \mathbf{A}^A$$

A.1.2.4 Fourth order volumetric projection tensor

The volumetric part of a second order tensor (A.35) can be rewritten to the form

$$\mathbf{A}^V = \frac{1}{3} \mathbf{1} \otimes \mathbf{1} : \mathbf{A} = \mathbb{I}^V : \mathbf{A} \quad A_{ij}^V = \frac{1}{3} \delta_{ij} \delta_{kl} A_{kl} = I_{ijkl}^V A_{kl}, \quad (\text{A.51})$$

where

$$\mathbb{I}^V = \frac{1}{3} \mathbf{1} \otimes \mathbf{1} \quad I_{ijkl}^V = \frac{1}{3} \delta_{ij} \delta_{kl} \quad (\text{A.52})$$

is the fourth order volumetric projection tensor.

A.1.2.5 Special identities

$$\mathbf{a} \cdot \mathbf{B} \cdot \mathbf{c} = \mathbf{B} : (\mathbf{a} \otimes \mathbf{c}) = (\mathbf{a} \otimes \mathbf{c}) : \mathbf{B} \quad a_i B_{ij} c_j = B_{ij} a_i c_j = a_i c_j B_{ij} \quad (\text{A.53})$$

$$\mathbf{a} \cdot \mathbf{B} \cdot \mathbf{a} = \mathbf{B} : (\mathbf{a} \otimes \mathbf{a}) = (\mathbf{a} \otimes \mathbf{a}) : \mathbf{B} \quad a_i B_{ij} a_j = B_{ij} a_i a_j = a_i a_j B_{ij} \quad (\text{A.54})$$

$$\mathbf{A} : (\mathbf{1} \times \mathbf{b}) = (\mathbf{1} \times \mathbf{A}) \cdot \mathbf{b} \quad A_{ij} (\varepsilon_{ijk} b_k) = (\varepsilon_{kij} A_{ij}) b_k \quad (\text{A.55})$$

$$\mathbf{1} \times (\mathbf{b} \otimes \mathbf{c}) = \mathbf{b} \times \mathbf{c} \quad \varepsilon_{ijk} b_j c_k \quad (\text{A.56})$$

A.1.2.6 Unit vectors

A unit vector \mathbf{n} is a vector with its norm equal to 1

$$\|\mathbf{n}\| = \sqrt{\mathbf{n} \cdot \mathbf{n}} = 1 \quad \|\mathbf{n}\| = \sqrt{n_i n_i} = 1 \quad (\text{A.57})$$

$$\mathbf{n} \cdot \mathbf{n} = 1 \quad n_i n_i = 1 \quad (\text{A.58})$$

resulting into useful identities

$$(\mathbf{I}^S \cdot \mathbf{n}) \cdot (\mathbf{n} \otimes \mathbf{n} \otimes \mathbf{n}) = I_{ijab}^S n_b n_a n_k n_l = n_i n_j n_k n_l = \mathbf{n} \otimes \mathbf{n} \otimes \mathbf{n} \otimes \mathbf{n}, \quad (\text{A.59})$$

$$(\mathbf{n} \otimes \mathbf{n} \otimes \mathbf{n}) \cdot (\mathbf{n} \cdot \mathbf{I}^S) = n_i n_j n_a n_b I_{baki}^S = n_i n_j n_k n_l = \mathbf{n} \otimes \mathbf{n} \otimes \mathbf{n} \otimes \mathbf{n}, \quad (\text{A.60})$$

$$(\mathbf{n} \otimes \mathbf{n} \otimes \mathbf{n}) \cdot (\mathbf{n} \otimes \mathbf{n} \otimes \mathbf{n}) = n_i n_j n_a n_a n_k n_l = n_i n_j n_k n_l = \mathbf{n} \otimes \mathbf{n} \otimes \mathbf{n} \otimes \mathbf{n}, \quad (\text{A.61})$$

$$\begin{aligned} (\mathbf{I}^S \cdot \mathbf{n}) \cdot (\mathbf{n} \cdot \mathbf{I}^S) &= I_{ijab}^S n_b n_c I_{caki}^S = \frac{1}{2} (\delta_{ia} \delta_{jb} + \delta_{ib} \delta_{ja}) n_b n_c \frac{1}{2} (\delta_{ck} \delta_{al} + \delta_{cl} \delta_{ak}) = \\ &= \frac{1}{4} (\delta_{ia} \delta_{jb} \delta_{ck} \delta_{al} + \delta_{ia} \delta_{jb} \delta_{cl} \delta_{ak} + \delta_{ib} \delta_{ja} \delta_{ck} \delta_{al} + \delta_{ib} \delta_{ja} \delta_{cl} \delta_{ak}) n_b n_c = \\ &= \frac{1}{4} (n_j n_k \delta_{il} + n_j n_l \delta_{ik} + n_i n_k \delta_{jl} + n_i n_l \delta_{jk}). \end{aligned} \quad (\text{A.62})$$

Trace of a tensor $\mathbf{n} \otimes \mathbf{n}$ equals 1:

$$\text{tr}(\mathbf{n} \otimes \mathbf{n}) = \mathbf{1} : (\mathbf{n} \otimes \mathbf{n}) = \mathbf{n} \cdot \mathbf{1} \cdot \mathbf{n} = \mathbf{n} \cdot \mathbf{n} = 1 \quad \text{tr}(n_i n_j) = \delta_{ij} n_i n_j = n_i n_i = 1 \quad (\text{A.63})$$

A.2 Differential calculus

The notation and terminology for differential calculus used in the thesis is summarized here.

Gradient

$$\mathbf{b} = \nabla a = \frac{\partial a}{\partial \mathbf{x}} \qquad b_i = \nabla_i a = \frac{\partial a}{\partial x_i} \qquad (\text{A.64})$$

$$\mathbf{B} = \nabla \otimes \mathbf{a} \qquad b_{ij} = \nabla_i a_j = \frac{\partial a_j}{\partial x_i} \qquad (\text{A.65})$$

$$\mathbf{B} = \mathbf{a} \otimes \nabla \qquad b_{ij} = a_i \nabla_j = \frac{\partial a_i}{\partial x_j} \qquad (\text{A.66})$$

The symmetric gradient is the symmetric part of the gradient

$$\mathbf{B} = \nabla^S \otimes \mathbf{a} = (\nabla \otimes \mathbf{a})^S = \frac{1}{2} (\nabla \otimes \mathbf{a} + \mathbf{a} \otimes \nabla) \qquad (\text{A.67})$$

$$b_{ij} = \nabla_i^S a_j = (\nabla_i a_j)^S = \frac{1}{2} \left(\frac{\partial a_i}{\partial x_j} + \frac{\partial a_j}{\partial x_i} \right) \qquad (\text{A.68})$$

The antisymmetric gradient is the antisymmetric part of the gradient

$$\mathbf{B} = \nabla^A \otimes \mathbf{a} = (\nabla \otimes \mathbf{a})^A = \frac{1}{2} (\mathbf{a} \otimes \nabla - \nabla \otimes \mathbf{a}) \qquad (\text{A.69})$$

$$b_{ij} = \nabla_i^A a_j = (\nabla_i a_j)^A = \frac{1}{2} \left(\frac{\partial a_i}{\partial x_j} - \frac{\partial a_j}{\partial x_i} \right) \qquad (\text{A.70})$$

Divergence

$$b = \nabla \cdot \mathbf{a} \qquad b = \nabla_i a_i = \frac{\partial a_i}{\partial x_i} \qquad (\text{A.71})$$

$$\mathbf{b} = \nabla \cdot \mathbf{A} \qquad b_j = \nabla_i A_{ij} = \frac{\partial A_{ij}}{\partial x_i} \qquad (\text{A.72})$$

$$\mathbf{B} = \nabla^m \cdot \mathcal{A} \qquad b_{ij} = \nabla_k A_{ikj} = \frac{\partial A_{ikj}}{\partial x_k} \qquad (\text{A.73})$$

∇^m means differentiation with respect to the middle index.

Divergence theorem

Divergence theorem (also known as Gauss's and/or Ostrogradsky's theorem) is "multi-dimensional integration by parts"

$$\int_V \nabla \cdot \mathbf{a} \, dV = \int_S \mathbf{n} \cdot \mathbf{a} \, dS \qquad \int_V \nabla_i a_i \, dV = \int_S n_i a_i \, dS \qquad (\text{A.74})$$

$$\int_V \nabla \cdot \mathbf{A} \, dV = \int_S \mathbf{n} \cdot \mathbf{A} \, dS \qquad \int_V \nabla_i A_{ij} \, dV = \int_S n_i A_{ij} \, dS \qquad (\text{A.75})$$

$$\int_V \nabla^m \cdot \mathcal{A} \, dV = \int_S \mathbf{n}^m \cdot \mathcal{A} \, dS \qquad \int_V \nabla_k A_{ikj} \, dV = \int_S n_k A_{ikj} \, dS \qquad (\text{A.76})$$

V and S denotes volume and surface of the integration domain, respectively.

Derivatives of products

$$\nabla \cdot (\mathbf{A} \cdot \mathbf{b}) = (\nabla \cdot \mathbf{A}) \cdot \mathbf{b} + \mathbf{A} : (\nabla \cdot \mathbf{b}) \quad \nabla_i (A_{ij} b_j) = (\nabla_i A_{ij}) b_j + A_{ij} (\nabla_i b_j) \quad (\text{A.77})$$

$$\nabla \cdot (\mathbf{a} \otimes \mathbf{B}) = (\mathbf{a} \otimes \nabla) \cdot \mathbf{B} + \mathbf{a} \otimes (\nabla \cdot \mathbf{B}) \quad \nabla_j (a_i B_{jk}) = (a_i \nabla_j) B_{jk} + a_i (\nabla_j B_{jk}) \quad (\text{A.78})$$

Gradient of position vector

A derivative of a vector with respect to itself is the second order identity tensor

$$\frac{\partial \mathbf{a}}{\partial \mathbf{a}} = \mathbf{1} \quad \frac{\partial a_i}{\partial a_j} = \delta_{ij}. \quad (\text{A.79})$$

Then it directly follows that the gradient of the position vector is the second order identity tensor

$$\begin{aligned} \nabla \otimes \mathbf{x} &= \mathbf{1} \quad \nabla_i x_j = \frac{\partial x_j}{\partial x_i} = \delta_{ij} \\ \mathbf{x} \otimes \nabla &= \mathbf{1} \quad \nabla_j x_i = \frac{\partial x_i}{\partial x_j} = \delta_{ij}. \end{aligned} \quad (\text{A.80})$$

Expressing a second order tensor using derivatives and position vector

Using equations (A.38) (A.78) and (A.80) yields

$$A_{ij} = \delta_{ik} A_{kj} = (x_i \nabla_k) A_{kj} = \nabla_k (x_i A_{kj}) - x_i (\nabla_k A_{kj}) \quad (\text{A.81})$$

$$\mathbf{A} = \mathbf{1} \cdot \mathbf{A} = (\mathbf{x} \otimes \nabla) \cdot \mathbf{A} = \nabla \cdot (\mathbf{x} \otimes \mathbf{A}) - \mathbf{x} \otimes (\nabla \cdot \mathbf{A}). \quad (\text{A.82})$$

A.3 Cosserat micropolar continuum mechanics

Basic concepts and conventions of Cosserat micropolar continuum are summarized in this section. Equations in this section are derived for the geometrically linear case from engineering point of view extending classical Boltzmann continuum knowledge.

Cosserat continuum (named after Cosserat brothers [20]) considers rotation of material points as an independent variable, therefore it can be used for the description of granular media. The presence of rotational degrees of freedom results in non-symmetric stress and strain tensors.

For more details, see [28, 20, 4, 100].

Consider a material domain with volume V and surface S . Each material point has reference position \mathbf{x} and undergoes displacement \mathbf{u} and *independent* rotation ϕ . Body force \mathbf{f} and body couple \mathbf{c} act at each inner point $\mathbf{x} \in V$ and surface force \mathbf{t} and surface couple \mathbf{m} act at each surface point $\mathbf{x} \in S$. All force and moment quantities may have zero values.

A.3.1 Kinematic equations

The displacement gradient

$$\mathbf{U} = \nabla \otimes \mathbf{u} \quad U_{ij} = \nabla_i u_j \quad (\text{A.83})$$

defines displacement \mathbf{du} of an infinitesimal line segment \mathbf{dx} as

$$\mathbf{du} = \mathbf{dx} \cdot \mathbf{U} \quad (\text{A.84})$$

and can be decomposed into the symmetric and antisymmetric part, representing *macro* strain tensor $\boldsymbol{\varepsilon}_M$ and rotation tensor $\boldsymbol{\Phi}_M$ (or corresponding axial vector $\boldsymbol{\phi}_M$), respectively:

$$\mathbf{U}^S = \boldsymbol{\varepsilon}_M = \nabla^S \otimes \mathbf{u} = \frac{1}{2} (\nabla \otimes \mathbf{u} + \mathbf{u} \otimes \nabla) \quad (\text{A.85})$$

$$\mathbf{U}^A = \boldsymbol{\Phi}_M = \nabla^A \otimes \mathbf{u} = \frac{1}{2} (\nabla \otimes \mathbf{u} - \mathbf{u} \otimes \nabla) = \mathbf{1} \times \boldsymbol{\phi}_M. \quad (\text{A.86})$$

The difference between the independent rotation degree of freedom $\boldsymbol{\phi}$ and the macro rotation $\boldsymbol{\phi}_M$ is additional quantity, the so called *micro* rotation $\boldsymbol{\phi}_m$:

$$\boldsymbol{\phi}_m = \boldsymbol{\phi} - \boldsymbol{\phi}_M. \quad (\text{A.87})$$

$\boldsymbol{\phi}_m$ represents “rotation of material points”, see subsection A.3.1.1. Cosserat strain is then defined as the macrostrain plus the contribution of the microrotation:

$$\boldsymbol{\varepsilon} = \boldsymbol{\varepsilon}_M - \mathbf{1} \times \boldsymbol{\phi}_m, \quad (\text{A.88})$$

which can also be rewritten to the form

$$\boldsymbol{\varepsilon} = \mathbf{U}^S - \mathbf{1} \times (\boldsymbol{\phi} - \boldsymbol{\phi}_M) = \mathbf{U}^S + \mathbf{U}^A - \mathbf{1} \times \boldsymbol{\phi} = \mathbf{U} - \mathbf{1} \times \boldsymbol{\phi} \quad (\text{A.89})$$

A more rigorous derivation is given by, e.g., [100].

Gradient of the rotation vector is the curvature tensor

$$\boldsymbol{\kappa} = \nabla \otimes \boldsymbol{\phi}. \quad (\text{A.90})$$

A.3.1.1 2D example, simple shear

Consider an elementary cube whose points have displacement $\mathbf{u} = \{ky, 0\}^T$ and *total* rotation $\boldsymbol{\phi} = \boldsymbol{\phi}_M + \boldsymbol{\phi}_m$. The displacement gradient is

$$\mathbf{U} = \nabla \otimes \mathbf{u} = \begin{bmatrix} 0 & 0 \\ k & 0 \end{bmatrix}, \quad \mathbf{dx} \cdot \mathbf{U} = \{dx, dy\}^T \cdot \begin{bmatrix} 0 & 0 \\ k & 0 \end{bmatrix} = \{kdy, 0\} = \mathbf{du} \quad (\text{A.91})$$

$$\boldsymbol{\varepsilon}_M = \mathbf{U}^S = \begin{bmatrix} 0 & \frac{1}{2}k \\ \frac{1}{2}k & 0 \end{bmatrix}, \quad \boldsymbol{\Phi}_M = \mathbf{U}^A = \begin{bmatrix} 0 & -\frac{1}{2}k \\ +\frac{1}{2}k & 0 \end{bmatrix}, \quad \boldsymbol{\phi}_M = -\frac{1}{2}k \quad (\text{A.92})$$

Now consider the microstrain with the value

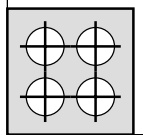
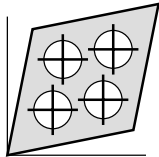
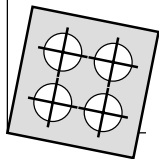
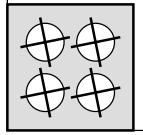
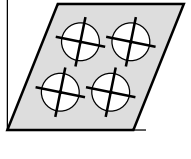
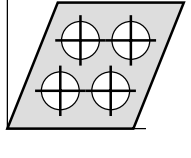
$$\boldsymbol{\phi}_m = +\frac{1}{2}k, \quad \boldsymbol{\Phi}_m = \begin{bmatrix} 0 & +\frac{1}{2}k \\ -\frac{1}{2}k & 0 \end{bmatrix}. \quad (\text{A.93})$$

The resulting Cosserat strain reads

$$\boldsymbol{\varepsilon} = \boldsymbol{\varepsilon}_M - \mathbf{1} \times \boldsymbol{\phi}_m = \boldsymbol{\varepsilon} = \boldsymbol{\varepsilon}_M - \boldsymbol{\Phi}_m = \begin{bmatrix} 0 & \frac{1}{2}k \\ \frac{1}{2}k & 0 \end{bmatrix} - \begin{bmatrix} 0 & +\frac{1}{2}k \\ -\frac{1}{2}k & 0 \end{bmatrix} = \begin{bmatrix} 0 & 0 \\ k & 0 \end{bmatrix} \quad (\text{A.94})$$

Table A.1 illustrates individual components of the displacement gradient and strain tensor, especially the values $\varepsilon_{12} = 0$ (no relative shear deformation between particles) and $\varepsilon_{21} = k$ (existent relative shear deformation between particles).

Table A.1: 2D representation of Cosserat strain

	\mathbf{U}	$\mathbf{U}^S = \boldsymbol{\varepsilon}_M$	$\mathbf{U}^A \equiv \phi_M$	ϕ_m	$\boldsymbol{\varepsilon} = \boldsymbol{\varepsilon}_M - \mathbf{1} \times \phi_m$
	$\begin{bmatrix} 0 & 0 \\ 0 & 0 \end{bmatrix}$	$\begin{bmatrix} 0 & 0 \\ 0 & 0 \end{bmatrix}$	0	0	$\begin{bmatrix} 0 & 0 \\ 0 & 0 \end{bmatrix}$
	$\begin{bmatrix} 0 & v \\ v & 0 \end{bmatrix}$	$\begin{bmatrix} 0 & v \\ v & 0 \end{bmatrix}$	0	0	$\begin{bmatrix} 0 & v \\ v & 0 \end{bmatrix}$
	$\begin{bmatrix} 0 & -v \\ v & 0 \end{bmatrix}$	$\begin{bmatrix} 0 & 0 \\ 0 & 0 \end{bmatrix}$	$-v$	0	$\begin{bmatrix} 0 & 0 \\ 0 & 0 \end{bmatrix}$
	$\begin{bmatrix} 0 & 0 \\ 0 & 0 \end{bmatrix}$	$\begin{bmatrix} 0 & 0 \\ 0 & 0 \end{bmatrix}$	0	v	$\begin{bmatrix} 0 & -v \\ v & 0 \end{bmatrix}$
	$\begin{bmatrix} 0 & 0 \\ 2v & 0 \end{bmatrix}$	$\begin{bmatrix} 0 & v \\ v & 0 \end{bmatrix}$	$-v$	0	$\begin{bmatrix} 0 & v \\ v & 0 \end{bmatrix}$
	$\begin{bmatrix} 0 & 0 \\ 2v & 0 \end{bmatrix}$	$\begin{bmatrix} 0 & v \\ v & 0 \end{bmatrix}$	$-v$	v	$\begin{bmatrix} 0 & 0 \\ 2v & 0 \end{bmatrix}$

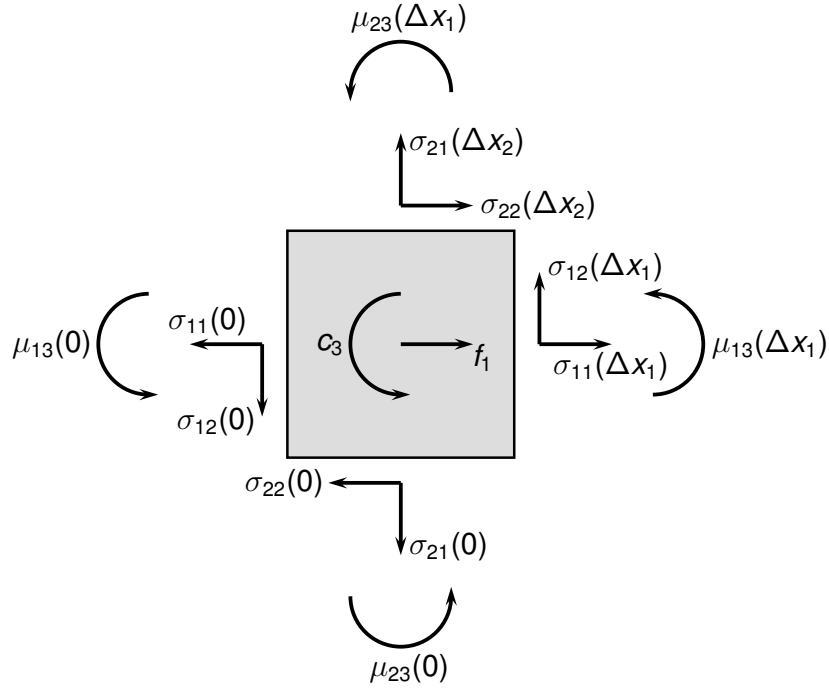


Figure A.1: 2D representation of stresses and couple stresses on elementary cube

A.3.2 Equilibrium equations

The material point can be represented by an infinitesimal cube with dimensions $\Delta \mathbf{x}$.

The stress state of material point is expressed by second order stress tensor σ and second order couple stress tensor μ , see figure A.1 for illustration. For the sake of simplicity, the two opposite corners have coordinates $\mathbf{0}$ and $\Delta \mathbf{x}$, but the same results would hold for corners \mathbf{x} and $\mathbf{x} + \Delta \mathbf{x}$.

The ij component of stress (couple stress) tensor equals surface force (surface couple) acting on the surface with normal \mathbf{e}_i in direction \mathbf{e}_j . Surface force \mathbf{t} and surface couple \mathbf{m} acting on surface with general normal \mathbf{n} can be expressed as the so called Cauchy's stress theorem

$$\mathbf{t} = \mathbf{n} \cdot \boldsymbol{\sigma} \quad \quad \quad t_j = n_i \sigma_{ij} \quad \quad \quad (\text{A.95})$$

$$\mathbf{m} = \mathbf{n} \cdot \boldsymbol{\mu} \quad \quad \quad m_j = n_i \mu_{ij}. \quad \quad \quad (\text{A.96})$$

Equilibrium equations are expressed in terms of body forces \mathbf{f} and body couples \mathbf{c} and can be derived from equilibrium on an infinitesimal cube considering its dimensions as a limit $\|\Delta \mathbf{x}\| \rightarrow 0$. For example, force equilibrium (2D) in direction 1 yields

$$\begin{aligned} -\Delta x_2 \sigma_{11}(0) + \Delta x_2 \sigma_{11}(\Delta x_1) - \Delta x_1 \sigma_{21}(0) + \Delta x_1 \sigma_{21}(\Delta x_2) + f_1 \Delta x_1 \Delta x_2 &= 0 \\ \frac{\Delta x_2 \sigma_{11}(\Delta x_1) - \Delta x_2 \sigma_{11}(0)}{\Delta x_1} + \frac{\Delta x_1 \sigma_{21}(\Delta x_2) - \Delta x_1 \sigma_{21}(0)}{\Delta x_2} + f_1 &= 0 \\ \lim_{\Delta x_i \rightarrow 0} \rightarrow \\ \nabla_1 \sigma_{11} + \nabla_2 \sigma_{21} + f_1 &= 0 \end{aligned} \quad \quad \quad (\text{A.97})$$

and moment equilibrium yields

$$\begin{aligned}
 & -\Delta x_2 \mu_{13}(0) + \Delta x_2 \mu_{13}(\Delta x_1) - \Delta x_1 \mu_{23}(0) + \Delta x_1 \sigma_{23}(\Delta x_2) + \\
 & \quad + \Delta x_2 \sigma_{12} \Delta x_1 - \Delta x_1 \sigma_{21} \Delta x_2 + c_3 \Delta x_1 \Delta x_2 = 0 \\
 & \frac{\Delta x_2 \mu_{13}(\Delta x_1) - \Delta x_2 \mu_{13}(0)}{\Delta x_1} + \frac{\Delta x_1 \mu_{23}(\Delta x_2) - \Delta x_1 \mu_{23}(0)}{\Delta x_2} + \sigma_{12} - \sigma_{21} + c_3 = 0 \quad (\text{A.98})
 \end{aligned}$$

$$\xrightarrow{\lim_{\Delta x_i \rightarrow 0}}$$

$$\nabla_1 \mu_{13} + \nabla_2 \mu_{23} + \sigma_{12} - \sigma_{21} + c_3 = 0.$$

Generalization of (A.97) and (A.98) yields full form of equilibrium equations (which can be derived more rigorously from linear momentum and angular momentum balance or virtual work principle, see section A.3.3):

$$\nabla_i \sigma_{ij} + f_j = 0 \quad \nabla \cdot \boldsymbol{\sigma} + \mathbf{f} = \mathbf{0} \quad (\text{A.99})$$

$$\nabla_i \mu_{ik} + \varepsilon_{kij} \sigma_{ij} + c_k = 0 \quad \nabla \cdot \boldsymbol{\mu} + \mathbf{1} \times \boldsymbol{\sigma} + \mathbf{c} = \mathbf{0}. \quad (\text{A.100})$$

A.3.3 Principle of virtual work

The virtual work principle (specifically the principle of virtual displacement) postulates that the virtual work of internal forces is equal to the virtual work of external forces

$$\int_V \boldsymbol{\sigma} : \delta \boldsymbol{\varepsilon} dV + \int_V \boldsymbol{\mu} : \delta \boldsymbol{\kappa} dV = \int_V \mathbf{f} \cdot \delta \mathbf{u} dV + \int_V \mathbf{c} \cdot \delta \boldsymbol{\phi} dV + \int_S \mathbf{t} \cdot \delta \mathbf{u} dS + \int_S \mathbf{m} \cdot \delta \boldsymbol{\phi} dS \quad (\text{A.101})$$

for any admissible virtual displacement $\delta \mathbf{u}$ and virtual rotation $\delta \boldsymbol{\phi}$. Applying kinematic constraints (A.88) and (A.90) on the virtual fields

$$\delta \boldsymbol{\varepsilon} = \delta \mathbf{U} - \mathbf{1} \times \delta \boldsymbol{\phi} = \nabla \otimes \delta \mathbf{u} - \mathbf{1} \times \delta \boldsymbol{\phi} \quad (\text{A.102})$$

$$\delta \boldsymbol{\kappa} = \nabla \otimes \delta \boldsymbol{\phi} \quad (\text{A.103})$$

yields two independent equations

$$\int_V \boldsymbol{\sigma} : (\nabla \otimes \delta \mathbf{u}) dV = \int_V \mathbf{f} \cdot \delta \mathbf{u} dV + \int_S \mathbf{t} \cdot \delta \mathbf{u} dS \quad (\text{A.104})$$

$$\int_V \boldsymbol{\mu} : (\nabla \otimes \delta \boldsymbol{\phi}) dV - \int_V \boldsymbol{\sigma} : (\mathbf{1} \times \delta \boldsymbol{\phi}) dV = \int_V \mathbf{c} \cdot \delta \boldsymbol{\phi} dV + \int_S \mathbf{m} \cdot \delta \boldsymbol{\phi} dS. \quad (\text{A.105})$$

Using (A.77) and (A.75), equation (A.104) can be rewritten to the form

$$\begin{aligned}
 \int_V \boldsymbol{\sigma} : (\nabla \otimes \delta \mathbf{u}) dV &= \int_V \nabla \cdot (\boldsymbol{\sigma} \cdot \delta \mathbf{u}) dV - \int_V (\nabla \cdot \boldsymbol{\sigma}) \cdot \delta \mathbf{u} dV = \\
 &= \int_S \mathbf{n} \cdot \boldsymbol{\sigma} \cdot \delta \mathbf{u} dS - \int_V (\nabla \cdot \boldsymbol{\sigma}) \cdot \delta \mathbf{u} dV = \int_V \mathbf{f} \cdot \delta \mathbf{u} dV + \int_S \mathbf{t} \cdot \delta \mathbf{u} dS
 \end{aligned} \quad (\text{A.106})$$

$$\xrightarrow{\forall \delta \mathbf{u}}$$

$$\nabla \cdot \boldsymbol{\sigma} + \mathbf{f} = \mathbf{0} \quad (\text{A.107})$$

$$\mathbf{t} = \mathbf{n} \cdot \boldsymbol{\sigma} \quad (\text{A.108})$$

yielding equilibrium equations (A.99) and (A.95).

Using (A.77) and (A.55), the first term of equation (A.105) can be rewritten to the form

$$\begin{aligned} \int_V \boldsymbol{\mu} : (\nabla \otimes \delta \boldsymbol{\phi}) dV &= \int_V \nabla \cdot (\boldsymbol{\mu} \cdot \delta \boldsymbol{\phi}) dV - \int_V (\nabla \cdot \boldsymbol{\mu}) \cdot \delta \boldsymbol{\phi} dV = \\ &= \int_S \mathbf{n} \cdot \boldsymbol{\mu} \cdot \delta \boldsymbol{\phi} dS - \int_V (\nabla \cdot \boldsymbol{\mu}) \cdot \delta \boldsymbol{\phi} dV \end{aligned} \quad (\text{A.109})$$

and the whole equation (A.105) can be rewritten to the form

$$\begin{aligned} \int_V \boldsymbol{\mu} : (\nabla \otimes \delta \boldsymbol{\phi}) dV - \int_V \boldsymbol{\sigma} : (\mathbf{1} \times \delta \boldsymbol{\phi}) dV &= \\ = \int_S \mathbf{n} \cdot \boldsymbol{\mu} \cdot \delta \boldsymbol{\phi} dS - \int_V (\nabla \cdot \boldsymbol{\mu}) \cdot \delta \boldsymbol{\phi} dV - \int_V (\mathbf{1} \times \boldsymbol{\sigma}) \cdot \delta \boldsymbol{\phi} dV &= \int_V \mathbf{c} \cdot \delta \boldsymbol{\phi} dV + \int_S \mathbf{m} \cdot \delta \boldsymbol{\phi} dS \end{aligned} \quad (\text{A.110})$$

$$\nabla \cdot \boldsymbol{\mu} + \mathbf{1} \times \boldsymbol{\sigma} + \mathbf{c} = \mathbf{0} \quad (\text{A.111})$$

$$\mathbf{m} = \mathbf{n} \cdot \boldsymbol{\mu} \quad (\text{A.112})$$

yielding equilibrium equations (A.100) and (A.96).

Or the other way around, contracting local equilibrium equations (A.107), (A.108), (A.111) and (A.112) with virtual displacement and virtual rotation and applying inverse modifications yields the equivalence of internal and external virtual work (A.101).

A.3.4 Classical Boltzmann continuum

Classical Boltzmann continuum is a special case of Cosserat continuum, specifically the case when the microstrain, couples and couple stress tensor are zero:

$$\boldsymbol{\phi}_m = \mathbf{0} \quad \mathbf{c} = \mathbf{0} \quad \mathbf{m} = \mathbf{0} \quad \boldsymbol{\mu} = \mathbf{0} \quad (\text{A.113})$$

Then rotation is defined by the antisymmetric part of the displacement gradient

$$\boldsymbol{\phi} = \boldsymbol{\phi}_M \quad \mathbf{1} \times \boldsymbol{\phi} = \mathbf{1} \times \boldsymbol{\phi}_M = \mathbf{U}^A, \quad (\text{A.114})$$

strain tensor (A.88) is the symmetric part of the displacement gradient

$$\boldsymbol{\varepsilon} = \boldsymbol{\varepsilon}_M = \mathbf{U}^S = \nabla^S \otimes \mathbf{u}, \quad (\text{A.115})$$

and stress tensor (A.100) is symmetric

$$\mathbf{1} \times \boldsymbol{\sigma} = \mathbf{0}. \quad (\text{A.116})$$

The virtual work principle (A.101) simplifies to (replacing the symmetric part of gradient with the gradient because of symmetry of the stress tensor)

$$\int_V \boldsymbol{\sigma} : \delta \boldsymbol{\varepsilon} dV = \int_V \boldsymbol{\sigma} : (\nabla^S \otimes \delta \mathbf{u}) dV = \int_V \boldsymbol{\sigma} : (\nabla \otimes \delta \mathbf{u}) dV = \int_V \mathbf{f} \cdot \delta \mathbf{u} dV + \int_S \mathbf{t} \cdot \delta \mathbf{u} dS \quad (\text{A.117})$$

yielding (unchanged) local equilibrium conditions (A.107) and (A.108):

$$\nabla \cdot \boldsymbol{\sigma} + \mathbf{f} = \mathbf{0} \quad \mathbf{n} \cdot \boldsymbol{\sigma} = \mathbf{t} \quad (\text{A.118})$$

A.3.4.1 Linear elasticity

The linear constitutive law

$$\boldsymbol{\sigma} = \mathbf{D}_e : \boldsymbol{\varepsilon} \quad (\text{A.119})$$

for linear isotropic material can be written in terms of Lamé coefficients λ and μ

$$\boldsymbol{\sigma} = 2\mu\boldsymbol{\varepsilon} + \lambda\mathbf{1}\text{tr}(\boldsymbol{\varepsilon}) = 2\mu\mathbf{I}^S : \boldsymbol{\varepsilon} + 3\lambda\mathbf{I}^V : \boldsymbol{\varepsilon} = (2\mu\mathbf{I}^S + 3\lambda\mathbf{I}^V) : \boldsymbol{\varepsilon} \quad (\text{A.120})$$

with elastic stiffness tensor

$$\mathbf{D}_e = 2\mu\mathbf{I}^S + 3\lambda\mathbf{I}^V. \quad (\text{A.121})$$

Lamé coefficients can be expressed in terms of Young's modulus E and Poisson's ratio ν and vice versa:

$$\begin{aligned} \lambda &= \frac{E\nu}{(1+\nu)(1-2\nu)} & \mu &= G = \frac{E}{2(1+\nu)} \\ \nu &= \mu \frac{3\lambda + 2\mu}{\lambda + \mu} & \nu &= \frac{\lambda}{2(\lambda + \mu)}. \end{aligned} \quad (\text{A.122})$$

The elastic stiffness tensor can then be expressed as

$$\mathbf{D}_e = \frac{E}{1+\nu}\mathbf{I}^S + \frac{3E\nu}{(1+\nu)(1-2\nu)}\mathbf{I}^V. \quad (\text{A.123})$$

A.4 Surface integrals over unit sphere

Values of surface and volume integrals over the unit sphere (over the solid angle Ω) of special tensorial functions

$$\int_{\Omega} d\Omega = 4\pi \quad (\text{A.124})$$

$$\int_{\Omega} n_i n_j d\Omega = \frac{4\pi}{3} \delta_{ij} \quad \int_{\Omega} \mathbf{n} \otimes \mathbf{n} d\Omega = \frac{4\pi}{3} \mathbf{1} \quad (\text{A.125})$$

$$\int_{\Omega} n_i n_j n_k n_l d\Omega = \frac{4\pi}{15} (\delta_{ij}\delta_{kl} + \delta_{ik}\delta_{jl} + \delta_{il}\delta_{jk}) = \frac{4\pi}{15} (3I_{ijkl}^V + 2I_{ijkl}^S) \quad (\text{A.126})$$

$$\int_{\Omega} \mathbf{n} \otimes \mathbf{n} \otimes \mathbf{n} \otimes \mathbf{n} d\Omega = \frac{4\pi}{15} (3\mathbf{I}^V + 2\mathbf{I}^S) \quad (\text{A.127})$$

$$\int_{\Omega} (\mathbf{I}^S \cdot \mathbf{n}) \cdot (\mathbf{n} \cdot \mathbf{I}^S) d\Omega = \frac{4\pi}{3} \mathbf{I}^S \quad \int_{\Omega} I_{ijab}^S n_b n_c I_{caki}^S d\Omega = \frac{4\pi}{3} I_{ijkl}^S \quad (\text{A.128})$$

are derived in this section. The simple surface integral (A.124) is mentioned here for the sake of completeness.

The validity of the formulas can be shown by mere component by component analytical integration using spherical coordinate system, or can be derived in more general way using special identities and rules mentioned earlier in this chapter.

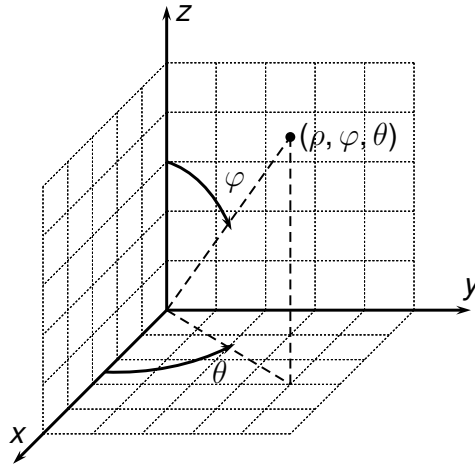


Figure A.2: Spherical coordinate system

A.4.1 Spherical coordinate system

Spherical coordinate system specifies a point by three coordinates:

- azimuth angle θ ($0 \leq \theta < 2\pi$),
- zenith angle φ ($0 \leq \varphi < \pi$),
- radial distance ρ .

The xyz components of position \mathbf{x} expressed by spherical coordinates are

$$\mathbf{x} = \begin{cases} \rho \sin \varphi \cos \theta \\ \rho \sin \varphi \sin \theta \\ \rho \cos \varphi \end{cases}. \quad (\text{A.129})$$

Integration of a function f over the surface or volume of the unit sphere requires the expression for surface and volume element $d\Omega$ and dV in spherical coordinates as follows:

$$\begin{aligned} \int_{\Omega} f d\Omega & \qquad \int_V f dV \\ d\Omega = \sin \varphi d\varphi d\theta & \qquad dV = \rho^2 \sin \varphi d\rho d\varphi d\theta. \end{aligned} \quad (\text{A.130})$$

Integral $\int_{\Omega} d\Omega$ is simply the surface area of the unit sphere

$$\int_{\Omega} d\Omega = \int_0^{2\pi} \int_0^{\pi} \sin \varphi d\varphi d\theta = 4\pi. \quad (\text{A.131})$$

Similarly, $\int_V dV$ is simply the volume of the unit sphere

$$\int_V dV = \int_0^{2\pi} \int_0^{\pi} \int_0^1 \rho^2 \sin \varphi d\rho d\varphi d\theta = \frac{4\pi}{3}. \quad (\text{A.132})$$

A special value of the volume integral of the squared distance from the unit sphere's center (used in the following section)

$$\mathbf{x} \cdot \mathbf{x} = x_i x_i = x^2 + y^2 + z^2 = \rho^2, \quad (\text{A.133})$$

equals

$$\int_V \mathbf{x} \cdot \mathbf{x} dV = \int_V x_i x_i dV = \int_0^{2\pi} \int_0^\pi \int_0^1 \rho^4 \sin \varphi d\rho d\varphi d\theta = 4\pi \int_0^1 \rho^4 d\rho = \frac{4\pi}{5}. \quad (\text{A.134})$$

Assuming $\mathbf{n} = \mathbf{x}$

$$\mathbf{n} = \begin{pmatrix} \sin \varphi \cos \theta \\ \sin \varphi \sin \theta \\ \cos \varphi \end{pmatrix} \quad (\text{A.135})$$

and $\rho = 1$ for the points *on* the surface of unit sphere, the validity of the following expressions can easily be shown by component-by-component analytical integration (A.130).

$$\int_\Omega n_i n_j d\Omega = \frac{4\pi}{3} \delta_{ij} \quad \int_\Omega \mathbf{n} \otimes \mathbf{n} d\Omega = \frac{4\pi}{3} \mathbf{1} \quad (\text{A.136})$$

$$\int_\Omega n_i n_j n_k n_l d\Omega = \frac{4\pi}{15} (\delta_{ij} \delta_{kl} + \delta_{ik} \delta_{jl} + \delta_{il} \delta_{jk}) = 4\pi \left(\frac{3}{15} I_{ijkl}^V + \frac{2}{15} I_{ijkl}^S \right) \quad (\text{A.137})$$

$$\int_\Omega \mathbf{n} \otimes \mathbf{n} \otimes \mathbf{n} \otimes \mathbf{n} d\Omega = 4\pi \left(\frac{3}{15} \mathbf{I}^V + \frac{2}{15} \mathbf{I}^S \right)$$

$$\int_\Omega (\mathbf{I}^S \cdot \mathbf{n}) \cdot (\mathbf{n} \cdot \mathbf{I}^S) d\Omega = \frac{4\pi}{3} \mathbf{I}^S \quad \int_\Omega I_{ijab}^S n_b n_c I_{caki}^S d\Omega = \frac{4\pi}{3} I_{ijkl}^S \quad (\text{A.138})$$

The validity of the analytical integration is shown in the script

codes/scripts/tests/intsolidangle.py.

A.4.2 A more general derivation

A more general approach is presented below. The method is based on divergence theorem (A.75), identity (A.80) and the fact that $\mathbf{n} = \mathbf{x}$ *on* unit sphere surface.

A.4.2.1 Identity (A.125)

$$\begin{aligned} \int_\Omega n_i n_j d\Omega &= \int_\Omega n_i x_j d\Omega = \int_V \nabla_i x_j dV = \int_V \delta_{ij} dV = \frac{4\pi}{3} \delta_{ij} \\ \int_\Omega \mathbf{n} \otimes \mathbf{n} d\Omega &= \int_\Omega \mathbf{n} \otimes \mathbf{x} d\Omega = \int_V \nabla \otimes \mathbf{x} dV = \int_V \mathbf{1} dV = \frac{4\pi}{3} \mathbf{1} \end{aligned} \quad (\text{A.139})$$

A.4.2.2 Identity (A.127)

First we investigate the relation between expressions $\int_\Omega \mathbf{n} \cdot \mathbf{n} d\Omega$ and $\int_V \mathbf{x} \cdot \mathbf{x} dV$ (because of the need to evaluate the derivative of a product, we begin with index notation). Using aforementioned tricks and identity (A.134):

$$\begin{aligned} \int_\Omega n_i n_j d\Omega &= \int_\Omega n_i n_j n_k n_k d\Omega = \int_\Omega n_i x_j x_k x_k d\Omega = \int_V \nabla_i (x_j x_k x_k) dV = \\ &= \int_V (\nabla_i x_j) x_k x_k + x_j (\nabla_i x_k) x_k + x_j x_k (\nabla_i x_k) dV = \\ &= \int_V \delta_{ij} x_k x_k + x_j \delta_{ik} x_k + x_j x_k \delta_{ik} dV = \int_V \delta_{ij} x_k x_k + x_i x_j + x_i x_j dV = \\ &= 2 \int_V x_i x_j dV + \delta_{ij} \frac{4\pi}{5} = 2 \int_V x_i x_j dV + \frac{3}{5} \int_\Omega n_i n_j d\Omega \end{aligned} \quad (\text{A.140})$$

Comparing the leftmost and the rightmost part of equation (A.140) and using (A.139)

$$\begin{aligned}\int_V x_i x_j dV &= \frac{1}{5} \int_{\Omega} n_i n_j d\Omega = \frac{4\pi}{15} \delta_{ij} \\ \int_V \mathbf{x} \cdot \mathbf{x} dV &= \frac{1}{5} \int_{\Omega} \mathbf{n} \cdot \mathbf{n} d\Omega = \frac{4\pi}{15} \mathbf{1},\end{aligned}\quad (\text{A.141})$$

$\int_{\Omega} n_i n_j n_k n_l d\Omega$ can be rewritten to the form

$$\int_{\Omega} n_i n_j n_k n_l d\Omega = \int_{\Omega} n_i x_j x_k x_l d\Omega = \int_V \nabla_i (x_j x_k x_l) dV = \quad (\text{A.142})$$

$$= \int_V (\nabla_i x_j) x_k x_l + (\nabla_i x_k) x_j x_l + (\nabla_i x_l) x_j x_k dV = \quad (\text{A.143})$$

$$= \int_V \delta_{ij} x_k x_l + \delta_{ik} x_j x_l + \delta_{il} x_j x_k dV. \quad (\text{A.144})$$

Recalling identity (A.141):

$$\int_{\Omega} n_i n_j n_k n_l d\Omega = \int_V \delta_{ij} x_k x_l + \delta_{ik} x_j x_l + \delta_{il} x_j x_k dV = \frac{4\pi}{15} (\delta_{ij} \delta_{kl} + \delta_{ik} \delta_{jl} + \delta_{il} \delta_{jk}) \quad (\text{A.145})$$

and definitions (A.52) and (A.45):

$$\begin{aligned}\int_{\Omega} n_i n_j n_k n_l d\Omega &= \frac{4\pi}{15} (\delta_{ij} \delta_{kl} + \delta_{ik} \delta_{jl} + \delta_{il} \delta_{jk}) = \frac{4\pi}{15} (3I_{ijkl}^V + 2I_{ijkl}^S) \\ \int_{\Omega} \mathbf{n} \otimes \mathbf{n} \otimes \mathbf{n} \otimes \mathbf{n} d\Omega &= \frac{4\pi}{15} (3\mathbb{I}^V + 2\mathbb{I}^S)\end{aligned}\quad (\text{A.146})$$

A.4.2.3 Identity (A.128)

With the help of (A.62), (A.139) and (A.146):

$$\begin{aligned}\int_{\Omega} I_{ijab}^S n_b n_c I_{caki}^S d\Omega &= \int_{\Omega} \frac{1}{4} (n_j n_k \delta_{il} + n_j n_l \delta_{ik} + n_i n_k \delta_{jl} + n_i n_l \delta_{jk}) d\Omega = \\ &= \frac{1}{4} \left(\int_{\Omega} n_j n_k \delta_{il} d\Omega + \int_{\Omega} n_j n_l \delta_{ik} d\Omega + \int_{\Omega} n_i n_k \delta_{jl} d\Omega + \int_{\Omega} n_i n_l \delta_{jk} d\Omega \right) = \\ &= \frac{1}{4} \left(\delta_{il} \int_{\Omega} n_j n_k d\Omega + \delta_{ik} \int_{\Omega} n_j n_l d\Omega + \delta_{jl} \int_{\Omega} n_i n_k d\Omega + \delta_{jk} \int_{\Omega} n_i n_l d\Omega \right) = \\ &= \frac{1}{4} \left(\delta_{il} \frac{4\pi}{3} \delta_{jk} + \delta_{ik} \frac{4\pi}{3} \delta_{jl} + \delta_{jl} \frac{4\pi}{3} \delta_{ik} + \delta_{jk} \frac{4\pi}{3} \delta_{il} \right) = \\ &= \frac{4\pi}{3} \frac{1}{4} (\delta_{il} \delta_{jk} + \delta_{ik} \delta_{jl} + \delta_{jl} \delta_{ik} + \delta_{jk} \delta_{il}) = \frac{4\pi}{3} \frac{1}{4} (2\delta_{ik} \delta_{jl} + 2\delta_{il} \delta_{jk}) = \frac{4\pi}{3} \frac{1}{2} (\delta_{ik} \delta_{jl} + \delta_{il} \delta_{jk})\end{aligned}\quad (\text{A.147})$$

$$\int_{\Omega} (\mathbb{I}^S \cdot \mathbf{n}) \cdot (\mathbf{n} \cdot \mathbb{I}^S) d\Omega = \frac{4\pi}{3} \mathbb{I}^S \quad \int_{\Omega} I_{ijab}^S n_b n_c I_{caki}^S d\Omega = \frac{4\pi}{3} I_{ijkl}^S \quad (\text{A.148})$$

A.5 Miscellaneous

Geometric center

The geometric center or centroid \mathbf{x}^0 of a region V is a point defined as

$$\mathbf{x}^0 = \frac{\int_V \mathbf{x} dV}{V}, \quad V\mathbf{x}^0 = \int_V \mathbf{x} dV. \quad (\text{A.149})$$

$\int_V \mathbf{x} dV$ is the first moment of volume with respect to the origin $\{0, 0, 0\}^T$. $\int_V \mathbf{x} - \mathbf{x}^a dV$ is the first moment of volume with respect to the point \mathbf{x}^a . Using the definition (A.149), it can be easily shown that the first moment of volume with respect to the centroid is zero:

$$\int_V \mathbf{x} - \mathbf{x}^0 dV = \int_V \mathbf{x} dV - \int_V \mathbf{x}^0 dV = \int_V \mathbf{x} dV - V\mathbf{x}^0 = \mathbf{0}. \quad (\text{A.150})$$

B Publications of the author

Journal papers

- [1] J. Stránský, J. Vorel, J. Zeman, and M. Šejnoha. Mori-Tanaka Based Estimates of Effective Thermal Conductivity of Various Engineering Materials. *Micromachines* 2 (2011), pp. 129–149.
- [2] W. Song, B. Huang, X. Shu, J. Stránský, and H. Wu. Interaction between railroad ballast and sleeper: a DEM-FEM approach. *International Journal of Geomechanics* (submitted).

Conference papers

- [1] J. Stránský, M. Jirásek, and V. Šmilauer. “Macroscopic Elastic Properties of Particle Models”. In: *Modelling and Simulation 2010*. Prague, Czech Republic, 2010.
- [2] J. Stránský, M. Jirásek, and V. Šmilauer. “Macroscopic Properties of Particle Models: Uniaxial Tension”. In: *Nano and Macro Mechanics 2010*. Prague, Czech Republic, 2010.
- [3] J. Stránský and M. Jirásek. “Calibration of Particle Models using Cells with Periodic Boundary Conditions”. In: *Particles 2011*. Barcelona, Spain, 2011.
- [4] J. Stránský and M. Jirásek. “Inelastic Calibration of Particle Models using Cells with Periodic Boundary Conditions”. In: *Nano and Macro Mechanics 2011*. Prague, Czech Republic, 2011.
- [5] J. Stránský and M. Jirásek. “Modeling of dynamic fragmentation: one-dimensional case”. In: *Engineering Mechanics 2011*. Svatka, Czech Republic, 2011.
- [6] J. Stránský. “JSMech - JavaScriptová knihovna pro snadné modelování, výpočet a zobrazování úloh stavební mechaniky”. In: *Juniorstav 2012*. Brno, Czech Republic, 2012.
- [7] J. Stránský and M. Jirásek. “Open Source FEM-DEM Coupling”. In: *Engineering Mechanics 2012*. Svatka, Czech Republic, 2012.
- [8] J. Stránský and M. Jirásek. “Review on evaluation of equivalent stress tensor in the discrete element method”. In: *Nano and Macro Mechanics 2012*. Prague, Czech Republic, 2012.
- [9] J. Stránský. “FEM - DEM Coupling and MuPIF Framework”. In: *Engineering Mechanics 2013*. Svatka, Czech Republic, 2013.
- [10] J. Stránský. “Open Source DEM-FEM Coupling”. In: *Particles 2013*. Stuttgart, Germany, 2013.
- [11] J. Stránský and M. Jirásek. “Localization Analysis of a Discrete Element Periodic Cell”. In: *Nano and Macro Mechanics 2013*. Prague, Czech Republic, 2013.
- [12] J. Stránský. “Combination of FEM and DEM with Application to Railway Ballast-Sleeper Interaction”. In: *Engineering Mechanics 2014*. Svatka, Czech Republic, 2014.

- [13] J. Stránský. “Kombinace MDP a MKP pro modelování interakce mezi železničním pražcem a podložím”. In: *Juniorstav 2014*. Brno, Czech Republic, 2014.
- [14] J. Stránský. “Stochastic Wang tiles generation using DEM and YADE software”. In: *Nano and Macro Mechanics 2014*. Prague, Czech Republic, 2014.
- [15] J. Stránský and M. Doškář. “Comparison of DEM-based Wang tilings and PUC”. In: *Nano and Macro Mechanics 2015*. Prague, Czech Republic, 2015.
- [16] J. Stránský and M. Doškář. “Stochastic Wang tiles generation using the discrete element method”. In: *Engineering Mechanics 2015*. Svatka, Czech Republic, 2015.

Other

- [1] B. Patzák, V. Šmilauer, and J. Stránský. *Program EduBeam, Uživatelský manuál*. Mar. 2015. URL: <http://mech.fsv.cvut.cz/svn/EduBeam/trunk/userGuide/EduBeam-userGuide.pdf>.
- [2] V. Šmilauer, E. Catalano, B. Chareyre, S. Dorofeenko, J. Duriez, A. Gladky, J. Kozicki, C. Modenese, L. Scholtès, L. Sibille, J. Stránský, and K. Thoeni. In: *Yade Documentation 2nd ed.* Ed. by V. Šmilauer. <http://yade-dem.org/doc/>. The Yade Project, 2010.
- [3] V. Šmilauer, E. Catalano, B. Chareyre, S. Dorofeenko, J. Duriez, N. Dyck, J. Eliáš, B. Er, A. Eulitz, A. Gladky, C. Jakob, F. Kneib, J. Kozicki, D. Marzougui, R. Maurin, C. Modenese, L. Scholtès, L. Sibille, J. Stránský, T. Sweijen, K. Thoeni, and C. Yuan. “Reference Manual”. In: *Yade Documentation 2nd ed.* <http://yade-dem.org/doc/>. The Yade Project, 2015. DOI: 10.5281/zenodo.34045.